N° d'ordre NNT : 021LYSEE005

THESE de DOCTORAT DE L'UNIVERSITE DE LYON
opérée au sein de l'Ecole centrale de Lyon

En cotutelle internationale avec China Scholarship Council

Ecole Doctorale N° 488
SCIENCES, INGÉNIERIE, SANTÉ

Spécialité de doctorat : Mécanique et Ingénierie

Soutenue publiquement le 21/09/201, par :
Jian CAO

Towards a new methodology to identify friction models under severe contact conditions

Devant le jury composé de :

ARRAZOLA ARRIOLA, Pedro José	Professeur	Univ. Mondragon Espagne	Président
GERMAIN, Guénaël	Professeur des Universités	Arts et Métiers	Rapporteur
DESPLANQUES, Yannick	Professeur des Universités	Centrale Lille	Rapporteur
RECH, Joël	Professeur des Universités	EC Lyon-ENISE	Directeur de thèse
COURBON, Cédric	Maître de Conférences	EC Lyon-ENISE	co-encadrant

Abstract

Keywords: finite element method, severe contact, contact temperature, thermal contact resistance, friction coefficient

In many industrial sectors, the ever increasing demands in terms of performance have led to a significant increase of the energy densities to be transmitted between two solids in contact. Involved mechanical systems are thus submitted to draconian working conditions, meaning that the interaction of the relatively moving component surfaces under severe contact conditions is clearly inevitable. Operating under "severe contact conditions" therefore commonly means under high contact pressures and/or sliding velocities and/or operating temperatures and/or oxidizing environments.

The specificity of such a contact configuration lies in the strong coupling between mechanical, thermal, metallurgical and chemical aspects. High temperatures will promote the formation of oxide layers whereas high sliding velocities and/or contact pressures will generate considerable energy densities that will be dissipated in a confined region in the near-surface. If experimental approaches are appealing, the key issue they face is not to investigate the tribological behaviour, i.e. to record friction and observe wear mechanisms, but rather to be able to assess and monitor the exact local contact conditions under which it occurs. This can be seen as a fundamental requirement to reach a better understanding of the complex phenomena occurring under such specific conditions but also to identify friction and wear models depending on local tribological parameters and nt system characteristics.

This thesis aims thus at generally improving the numerical simulation of a sliding contact under extreme contact conditions and proposing an innovative methodology to better identify friction models.

Two 3D finite element (FE) models based on commercial code ABAQUS have first been established to simulate local parameters, such as heat flux and temperature. The first numerical model is an explicit scratch model based on the arbitrary Lagrangian-Eulerian (ALE) approach. It is employed to investigate the contact of a spherical pin during the scratching process under severe contact condition and extract local contact pressures and sliding velocities. A second full 3D heat transfer model is then combined to estimate the interface temperature distribution on the pin surface based on the heat flux distribution computed in the explicit one. This multi-scale approach can simulate

the scratching process until the system reaches the thermal balance conditions and a more realistic 3D temperature distribution at the interface of the pin can be estimated. A sensitivity analysis is performed using this methodology and revealed that the pin & pin holder thermal contact resistance (TCR) plays a significant role in the prediction of realistic temperature distribution.

An experimental set-up is then developed in order to assess this TCR and enhance the prediction of temperature fields in a sliding contact. A laser source is used to heat the pin and/or pin-holder system both equipped with thermocouples and record the temperature evolution at different locations. A FE model is employed to simulate the heat transfer on the one hand between the laser and the pin, and on the other hand, between the pin and the pin-holder. An inverse method is finally applied and the TCR value is adjusted based on the best fit between experimental and simulated temperatures.

The last part covers a new methodology to improve the identification of a generic friction model. A parametric adhesive friction equation μ_{adh} is implemented in the 3D FE scratch model and selected in the form of an exponential decay depending on the local sliding velocity. The model is further used to generate a large amount of data by computing the scratching outputs under a large range of equation parameters and sliding velocities. A surrogate modelling methodology is then applied on the numerical apparent friction coefficient $\mu_{app-num}$ with a simple Response-Surface-Method approach (RSM). The latter leads to a reduced equation that can be instantaneously used to identify the best fitting equation parameters compared to the reference experimental data, opening new perspectives in terms of fast and efficient identification method. The identified equation is finally imported as the input data in the FE model to verify the relevance of the methodology over the whole range of sliding velocities by comparing the macroscopic apparent numerical friction coefficient $\mu_{app-num}$ to the experimental one $\mu_{app-exp}$.

Acknowledgements

I should like to acknowledge with deep gratitude the assistance and guidance given to me by my PhD supervisors, Prof. Joel RECH and Dr. Cedric COURBON, for their kindly supporting during the past four years.

Joel is one of the most knowledgeable people I have ever met. He has provided insightful suggestions about the research. I benefited not only from his deep insights and knowledge but also from his patience and encouragement. I am incredibly grateful to Cedric for his careful guide not only in scientific fields but also in daily life. I am also thankful to Prof. Pedro Jose ARRAZOLA ARRIOLA, Prof. Guénaël GERMAIN, and Prof. Yannick DESPLANQUES for serving on my supervisory committee.

I also want to thank all the members of ENISE for contributing to a great and fun research environment and for many interesting discussions. Especially Julien SIJOBERT, Isabelle PLETTO, Florian DUMONT, Carmella TARDY, and Robin MATEJICEK for their kind support.

I would like to thank my dear friends and colleagu es Dr. Rafal KAMINSKI, Dr. Vipul VIJIGIRI, Dr. Synthia DIVIN, Maxime DUMAS, Irati MALKORRA, Gregory METHON, Timothe LEVEILLE, Thomas PERARD, Florent CLAVIER, Oussama CHERGUY and Aleksandr KULISH for their support and friendly environment during my years as a PhD student. I would also like to thank my friend Chen HE and Sixiang XU for staying with me through the boring Covid quarantine.

I especially thank my family, my father, my mother, and my sister. I could never be who I am without their extraordinary support.

Thanks again to everyone I have met along the way.

Contents

List of Figures

List of Tables

List of acronyms

ALE

arbitrary Lagrangian-Eulerian. I

CCD

central composite design. 102

FE

finite element. I

Fpass

passband frequency. 97

FSW

Friction stir welding. 14–18

HFLA

heat flux multiplied by the nodal area. 57, 58, 63

STD

standard deviation. 99

TCC

thermal contact conductance. 9, 85, 87

TCR

thermal contact resistance. 9, 10, 41, 42, 57, 62, 64–66, 68–73, 75–78, 81, 85–89, 104, II

Glossary

C3D8RT

Coupled temperature-displacement elements, 8-node thermally coupled brick, trilinear displacement and temperature, reduced integration. 54

C3D8T

Coupled temperature-displacement elements, 8-node thermally coupled brick, trilinear displacement and temperature. 54

DC3D8

Diffusive heat transfer, 8-node linear brick. 61

Diff

difference between the original and filtered apparent friction coeffcient. 99

Nomenclature

σ

von Mises flow stress [MPa]. 55

A

yield strength [MPa]. 55

a_{pin}

thermal diffusivity of the pin [$m^2 \cdot s^{-1}$]. 41

Ac

equation of the contact area [m^2]. 42

α

heat partition coefficient. 42, 57

B

hardening modulus [MPa]. 55

b

characteristic length of the contact [m]. 41

C

strain rate sensitivity coefficient (viscosity). 55

d_c

decay constant. 92–94, 96–101, XIII

dev

deviation between experimental and numerical data. 85

dev_{μ}

frictional deviation. 93, 101, 102

$\dot{\varepsilon_0}$

reference plastic strain rate. 55

ε_p

equivalent plastic strain. 55

$\dot{\varepsilon}_p$

plastic strain rate [s^{-1}]. 55

e_q

dissipated kinetic energy during test [J]. 37

F_{R1}

reaction force along the x direction [N]. 92

F_n

normal force [N]. 15, 24, 25, 31, 42, 54, 57, 61, 92, 97

F_t

tangential force [N]. 24, 31, 42

k

similitude factor. 37

λ

efficiency ratio of the laser. 76

λ_{pin}

thermal conductivity of the pin [$W \cdot m^{-1} \cdot K^{-1}$]. 41

$\lambda_{workpiece}$

thermal conductivity of the workpiece [$W \cdot m^{-1} \cdot K^{-1}$]. 41

m

thermal softening coefficient. 55

μ_{adh}

adhesive friction coefficient. 43, 56, 91, 92, 94, 103–105, II

$\mu_{app-exp}$

experimental macroscopic friction coefficient. 42, 43, 92, 94, 95, 101–103, 105, II

$\mu_{app-num}$

theoretical macroscopic friction coefficient. 43, 60, 92–95, 97–99, 101–103, 105, II, XIII

$\mu_{app-RSM}$

numerical apparent friction coefficient estimated by RSM. 93, 101–103

μ_{def}

plastic deformation part of the apparent friction coefficient. 43

μ_{app}

apparent friction coefficient. 43

μ_{k}

local kinetic adhesive friction coefficient. 92–94, 96, 97, 99–101

μ_{s}

local static adhesive friction coefficient. 91–94, 96, 97, 99–101

n

hardening coefficient. 55

P

cutting force resulting from localized phenomena close to the cutting edge [N]. 21

p

macroscopic heat partition ratio. 41, 42

$P_{\mathbf{actual}}$

the actual power which penetrate the interface and heat the materials [W]. 76

$P_{\mathbf{laser}}$

the power of the laser [W]. 76

Pe

Peclet number. 41

$\varnothing$

heat flux generated at interface [$W \cdot m^{-2}$]. 41, 42

$\varnothing_{pin}$

heat flux transmitted to the pin [$W \cdot m^{-2}$]. 41, 42

$\varnothing_{workpiece}$

heat flux transmitted to the workpiece [$W \cdot m^{-2}$]. 41, 42

Q

cutting force on the rake face [N]. 21

S_d

disc friction-surface area of disc braking process [m^2]. 37

s_d

disc friction-surface area of test [m^2]. 37

S_p

pad friction-surface area of disc braking process [m^2]. 37

s_p

pad friction-surface area of test [m^2]. 37

T

absolute temperature [K]. 55

T_0

room temperature [K]. 55

T_1

temperature of solid 1 at interacting surface [K]. 41, 42

T_2

temperature of solid 2 at interacting surface [K]. 41, 42

$T_{exp-TC3}$

experimental measured temperature of TC3 at time t [K]. 85

$T_{exp-TC4}$

experimental measured temperature of TC4 at time t [K]. 85

T_M

melting point of the specific alloy [K]. 55

$T_{num-TC3}$

numerically simulated temperature of TC3 at time t [K]. 85

$T_{num-TC4}$

numerically simulated temperature of TC4 at time t [K]. 85

$T_{max-imp}$

max temperature at interface of explicit model [K]. 64

V_{in}

velocity of the workmaterial flow into the Eulerian surface [$m \cdot s^{-1}$]. 54

V_{out}

velocity of the workmaterial flow out of the Eulerian surface [$m \cdot s^{-1}$]. 54

V_{ls}

local sliding velocity [$m \cdot s^{-1}$]. 59, 91, 92, 103

V_{macro}

macroscopic sliding velocity $[m \cdot s^{-1}]$. 41, 43, 44, 56, 57, 59–61, 63, 66, 68, 93, 94, 96–99, 102, 103, 105, XIII

0 Introduction

The term tribology is derived from the Greek "tribos" meaning "to rub". It is defined as the science and technology of interacting surfaces in relative motion and comprises the study of lubrication, friction and wear [1]. The latter has a significant impact on economic losses and is , more and more, related to environmental issues. Despite the development and applications of new tribological solutions, the influence of the wear and friction on energy consumption, economic expenditure, and CO2 emission on a global scale are still indeed considerable [2]. Nowadays, with applications and research ranging from wheel and rail contacts, gears, bearing to biomedical, sports or defense applications etc, tribology has attracted multiple fields of interests.

Tribology under severe contact conditions

In many industrial sectors, the ever increasing demands in terms of performance have led to a significant increase of the energy densities to be transmitted between two solids in contact. Involved mechanical systems are thus submitted to draconian working conditions, meaning that the interaction of the relatively moving component surfaces under severe contact conditions is clearly inevitable. Operating under "severe contact conditions" therefore commonly means under high contact pressures and/or sliding velocities and/or operating temperatures and/or oxidizing environments.

These are commonly encountered in applications such as automotive, aerospace or nuclear industries but also in several metal working processes. The latter are especially concerned as, behind the question of productivity directly related to the tool-workmaterial interaction, friction and wear directly govern the final mechanical and microstructural state of the generated surface. In other words, they directly govern the final in-use properties and lifetime of the manufactured component, key issue for some leading-edge industries.

Motivations

Perfectly controlling the processes in order to improve these properties necessarily requires a deep understanding of the tribological phenomena occurring under such extreme and broad contact conditions. The specificity of such a contact configuration lies in the strong coupling between mechanical, thermal, metallurgical and chemical aspects. High temperatures will promote the formation of oxide layers whereas high sliding velocities and/or contact pressures will generate considerable energy densities that will be dissipated in a confined region in the near-surface.

With the growing emergence of new materials, the development of advanced experimental methods able to simulate these conditions and provide relevant, original and real-time data is of course essential. However, if experimental approaches are appealing, the key issue is not to investigate the tribological behaviour, i.e. to record friction and observe wear mechanisms, but rather to be able to assess and monitor the exact local contact conditions under which it occurs. Moreover, it is known that friction and wear are highly system dependent meaning that the interaction between the materials in contact and any interfacial media that may be in-between, the surface morphology and the surrounding environment define the response of a system. It becomes thus tricky to think that friction values recorded on a specific test bench could be identically provided by a different one, or even worst, be directly extracted from the actual application.

Considering these ever existing challenges in tribology, there is a clear need to propose alternative methodologies to "numerically probe" the contact interface and extract local data which could not be measured experimentally. The driving idea is that a robust simulation is definitely required to reach a better understanding of the complex phenomena occurring under such specific conditions, draw conclusions less dependent on the tribological system and provide more valuable outputs such as generic friction or wear models.

Objectives of the work

This thesis aims thus at generally improving the numerical simulation of a sliding contact under extreme contact conditions and proposing an innovative methodology to better identify friction models. The detailed objectives of the present work can be listed as:

- To develop a modelling strategy to properly predict the thermo-mechanical loadings at the contact interface;
- To identify the impact of various physical or numerical parameters on the predicted outputs by thorough sensitivity analyses;

- Propose an experimental approach to identify the major boundary conditions governing the heat transfer and contact temperature distribution;
- To investigate the local contact conditions at the interface under extreme conditions, such as the local contact temperature distribution, contact pressure distribution, heat flux distribution at the interface and propose a new methodology to identify friction or heat partition models based on these local data.

Outline of the Thesis

The thesis is drafted in 4 chapters, where Chapter 1 covers a detailed literature review on tribology under severe contact conditions with a special focus on manufacturing processes. The basic principle of tribology is presented whereas experimental and numerical approaches to investigate such contacts are discussed.

In Chapter 2, a multi-scale finite element-based approach is developed to 3D model the scratching process and monitor the physical properties versus time between the contacting surfaces. The details of the models are presented in this chapter including the design of the methodology and model, the thermal physical properties, the element type, boundary conditions as well as the data processing. Sensitivity studies of the multi-scale model are carried out. The critical boundary conditions are identified to improve the reliability of the numerical simulation results.

Based on the critical boundary conditions identified in the previous chapter, Chapter 3 proposes an experimental method to calibrate the thermal contact resistance (TCR) in the pin system to precisely monitor the temperature distribution at each contact surface.

In Chapter 4, a variable friction is then implemented in the scratching model and a large scale numerical screening method is proposed to cover a wide range of possible combinations. The large amount of generated numerical data is then used to identify an enhanced friction model based on local conditions such as sliding velocity.

Finally, in the last chapter, a general conclusion is presented summarizing the different contributions and further perspectives.

1 Literature review

Summary

1.1 Basics of tribology under severe contact conditions

Manufacturing is defined as the transformation of materials and information into goods to satisfy human needs [3]. In the background of global competition, companies and corporations are compelled to improve their production efficiency, shorten production time and control the costs. In manufacturing industries, higher production efficiency likely leads to more critical manufacturing parameters.

Manufacturing processes is a broad terminology that takes into account a wide range of technologies as shown in the classification in Fig. 1.1 [4]. The present work will focus on the material removal processes.

On the one hand, deformation processes are based on shaping the work material by the application of forces resulting in stresses that exceed the yield strength of the material. The work material can be heated before being deformed to improve the ductility and avoid fracture, such as in hot forming. Deformation processes are associated most closely with metalworking and include operations such as forging, extrusion or stamping. On the other hand, material removal cut excess material from raw material to generate the final desired and functional geometry.

1.1.1 Machining

Machining is a material removal process based on chip formation using a cutting tool with a defined cutting edge. During the cutting process, the work material is affected by a severe plastic deformation, i.e., shearing and compression, whereas the cutting tool is subjected to high cutting forces and heat generation due to friction. The critical deformation leads to critical high stress, high strain, high strain rate and high temperature in a small area [5]. Complex shapes and a good surface finish could be produced by machining. Among the machining operations, turning, drilling, and milling are the most common operations (Fig. 1.2).

In order to target the contact conditions, a schematic of the cutting zone is shown in Fig. 1.3 to present the fundamentals of a machining process. Three regions are considered in the shear zone model: the primary shear zone, the secondary shear zone, and the rubbing/tertiary shear zone.

The primary shear zone is a narrow region around the shear plane from the cutting edge to the surface of the workpiece. The work material is submitted to an intermediate plastic deformation under critical shear strains and stresses (Fig. 1.3b). The secondary shear zone is the surrounding area along the tool-chip interface and is characterised by severe plastic deformations and friction.

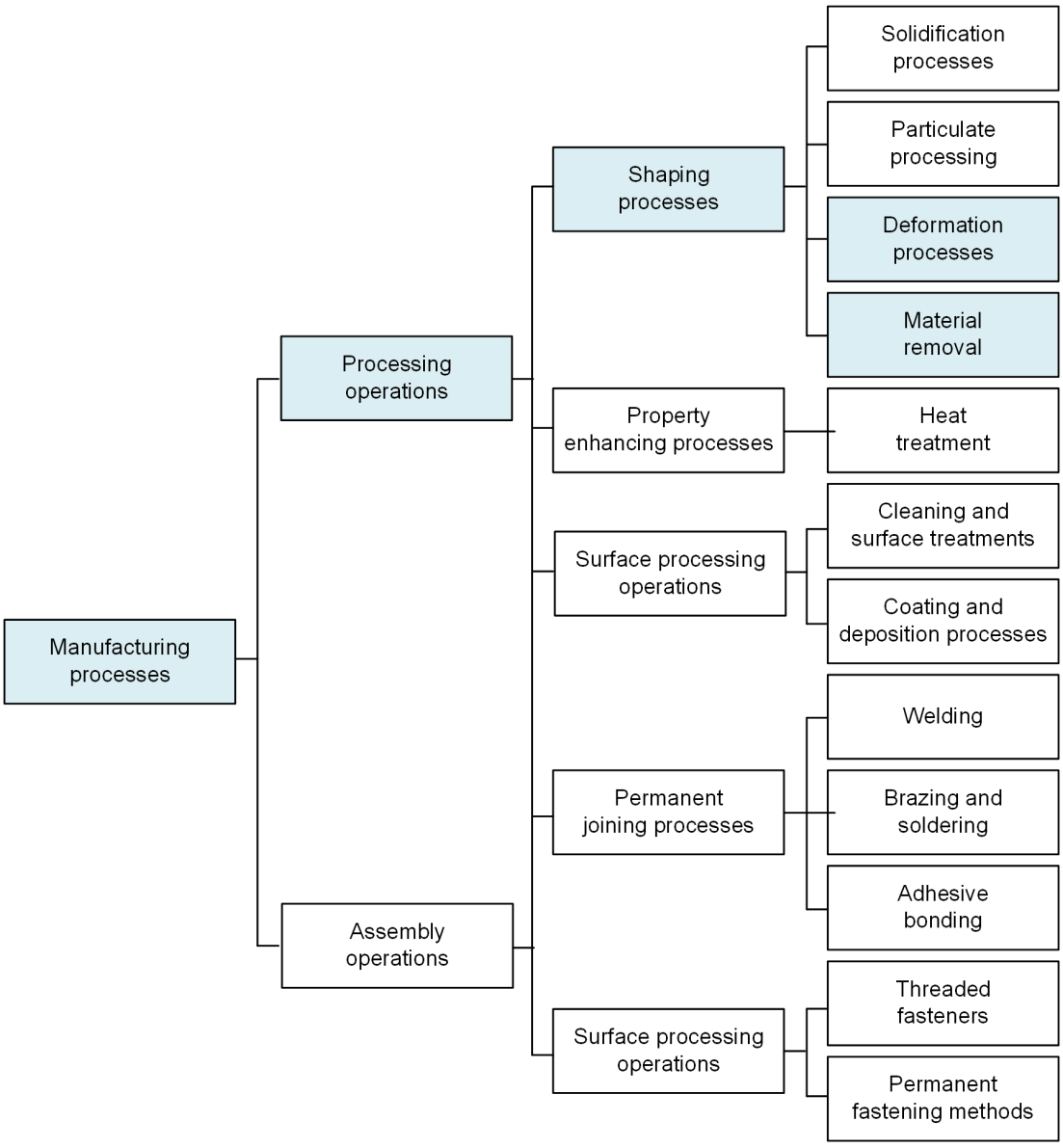

Figure 1.1: Classification of the various manufacturing processes [4].

The early work from Zorev et al. [8], highlighted that the contact conditions in this region are highly complex. For example, they showed that the normal and shear stresses on the rake surface give rise to a region of seizure (or sticking) close to the cutting edge and to a region of sliding in the remaining contact interface [9]. They first introduced the fact that a sliding velocity gradient exists all along the contact zone. This can be now observed by more advanced techniques such as numerical simulation as in Fig. 1.4a & c which shows the evolution of the local sliding velocity along the tool-chip interface at a cutting speed of 2 $\mathrm{m \cdot s^{-1}}$. A friction model depending on local

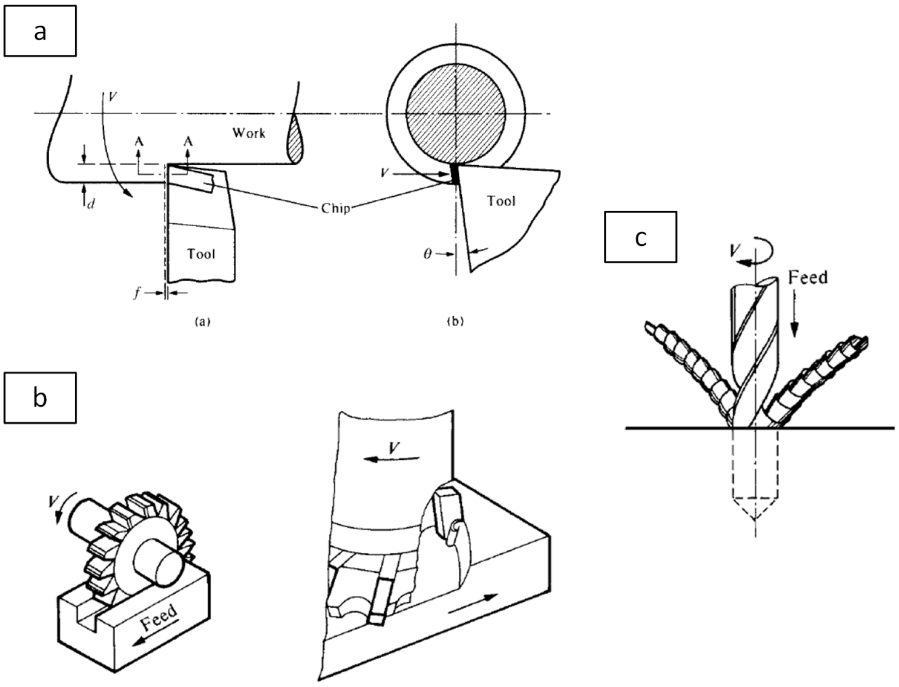

Figure 1.2: Three most widely used cutting process: (a) turning, (b) milling , and (c) drilling [6].

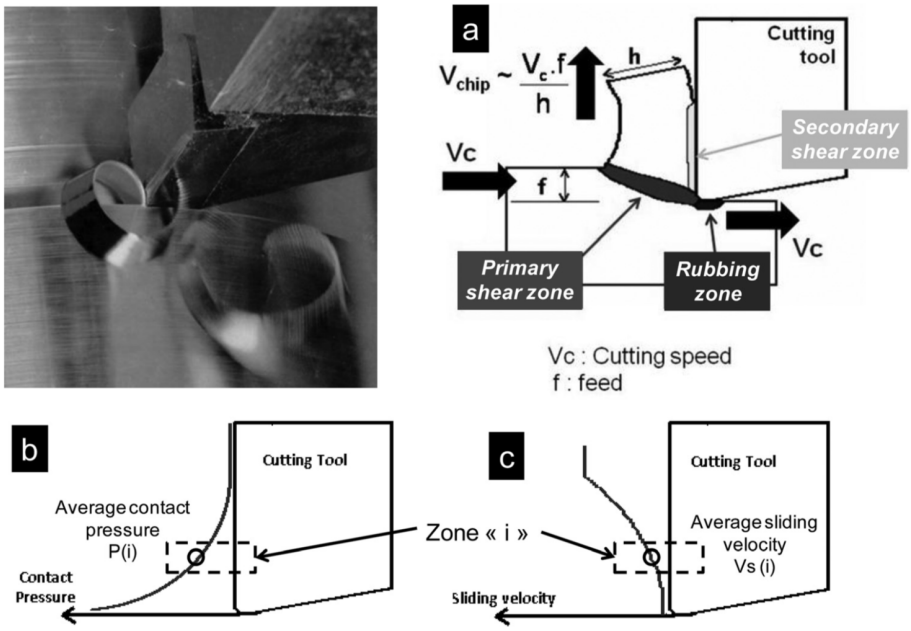

Figure 1.3: (a) Mechanism of chip formation, (b) typical shape of normal stress distribution, and (c) sliding velocity distribution on the tool rake face [7].

sliding velocity is employed in this research. The local sliding velocity on the rake face indeed increases from 0 close to the material separation point to 1.5 $\mathrm{m \cdot s^{-1}}$ at the end of the contact.

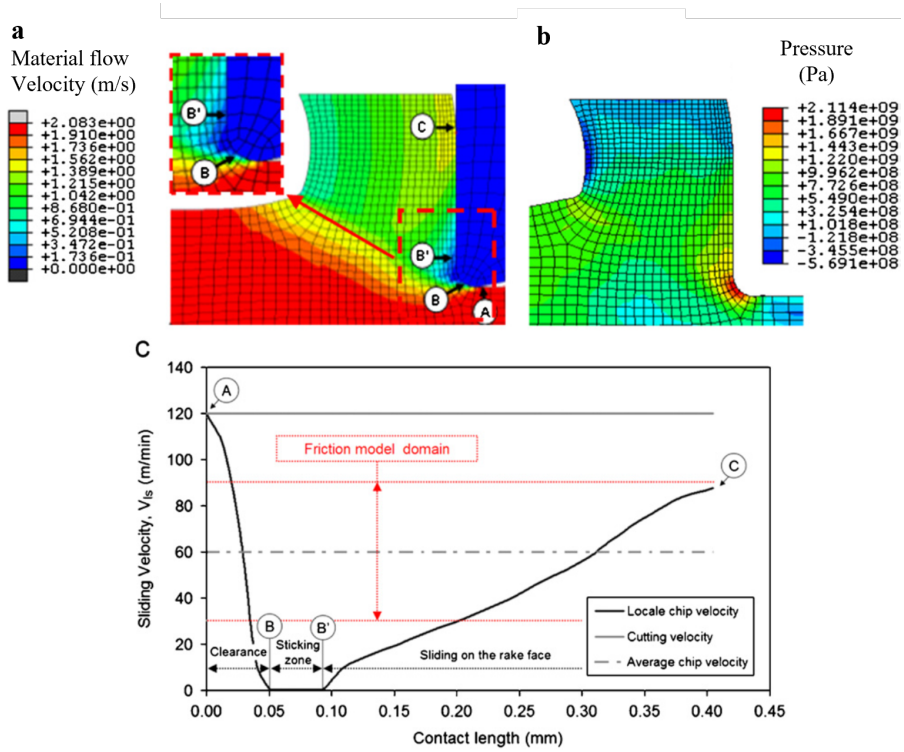

Figure 1.4: Velocity and pressure variation at the tool-chip interface [10].

The Fig. 1.4b also indicates that the maximum contact pressure can exceed 2 GPa. This can be way beyond the material yield stress, leading obviously to a plastic contact. In most of the studies dealing with machining, the tool-chip contact is assumed to occur under perfect plastic conditions [10, 11]. However, When two surfaces are brought into contact, no matter how well polished the surfaces, only a small fraction of the surfaces is actually in contact because of the roughness, non-flatness imperfections of the contacting surfaces [12], as shown in Fig. 1.5 [13].

Even if the macroscopic contact pressure can exceed the yield stress, the real contact area can still be less than 30% of the apparent contact area. [15]. The uniform heat flow is almost exclusively constricted to solid-to-solid contact areas and gives rise to a macroscopically observed temperature jump across the interface. This resistance to heat transfer is called joint resistance or thermal contact resistance TCR, and the inverse value is the so-called thermal contact conductance (TCC)[16], as Equ. 1.1 shows.

$$TCC = \frac{1}{TCR} \tag{1.1}$$

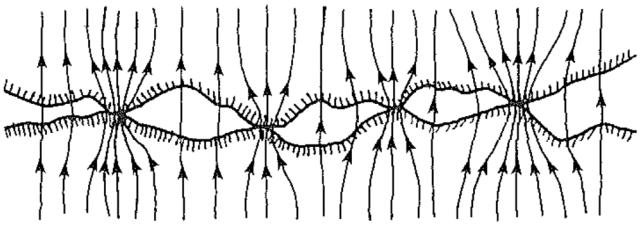

Figure 1.5: Heat flow through a joint [14].

For the manufacturing process, the TCR between assembled parts of the tool plays a significant part in the temperature distribution [17, 18, 19]. In order to avoid cutting tool overheating, some researchers investigated the effect of thermal resistance between the cutting tool and its supports on the temperature by COMSOL Multiphysics software. Different mediums between the assembled parts are considered. It indicated that the use of air showed the highest thermal resistance while using copper and aluminum foils considerably decreased the maximum tool temperature and gave results close to the case of zero thermal resistance. Mondelin et al. [19] proposed an experiment and simulation procedure to calibrate the TCR between insert and tool holder to optimize cutting conditions and improve tool lifetime as well as the quality of the pieces produced.

In numerical simulation, the TCR is generally assumed to be 0 (thermal perfect contact) [20] or a constant value between 1 to 100 $K \cdot mm^{-2} \cdot k^{-1}$ [18, 21, 22, 21, 23]. Courbon et al. [18] studied the TCR at the tool-chip interface in dry cutting of AISI 1045. The results reveal that an imperfect contact exists at the sliding part of the contact leading to a TCR at a higher value of $100\,K \cdot mm^2 \cdot W^{-1}$. Bourouga et al. [23] found that the TCR of sliding contact between AISI 1045 and M2 tool is around $90\,K \cdot mm^2 \cdot W^{-1}$ whereas Kusiak et al. [24] also showed that the tool coating also contributes to the TCR. The large range of TCR at interface could be explained by the theory of nonlinear thermoelastic behaviour of contacting solids by Attia and Kops [25, 26, 27]. The contact pressure distribution at interface has a critical impact on the redistributing the heat flux across the interface.

The severe contact conditions at the interface during the machining process result in disadvantageous effects, such as critical wear [28]. The experimental results indicate that high wear is characterized by high friction [29]. Thus the controlling the heat generation and heat removal would help reduce the drawbacks. Fig. 1.6 presented the topography of the cutting tool wear after tuning of AISI 1045 steel over 8 min at dry cutting and minimum quantity cooling lubrication (MQCL) conditions. It shows that MQCL could decrease the crater depth. Furthermore, the duration length, from several minutes to several hours, also has a significant influence on cutting tool wear.

An important specificity of metal cutting is that new surfaces are formed by plastic

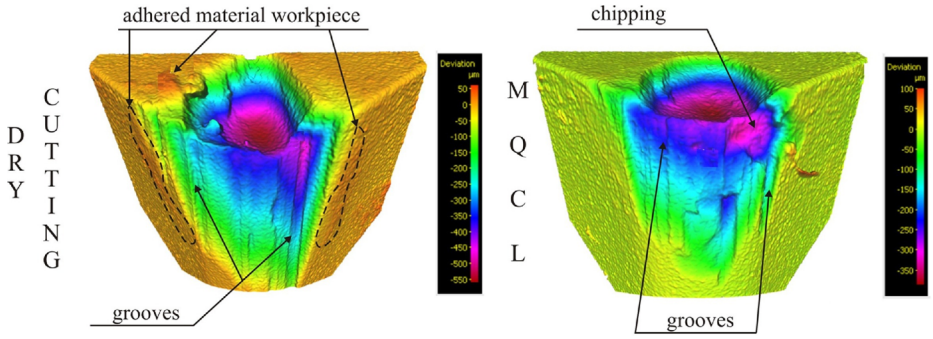

Figure 1.6: Topography of the cutting tool wear of dry cutting and MQCL [29].

flow around the tool edge. Thus the cutting process could be considered as an open system from the tribological point of view. A so-called open tribo-system is characterized by having only one of the interacting surfaces permanently in contact whereas the other one is continuously regenerated. On the contrary, in closed tribo-systems, both of the surfaces are always in contact throughout the duration of the test and are therefore continuously engaged in the tribological process. In this case, repeated work-hardening or even wear particles can be generated in the contact, which will then act as a so-called 'third body', drastically modifying the tribological behavior. For example, the pin-on-disc test is a widely used tribosystem. The comparisons between the open and closed tribosystem will be developed more in detail in section 1.2.

Indeed, at the tool-material contact zone, the sliding velocities could reach 60–600 $m \cdot min^{-1}$, the temperatures are up to 1000 °C, and the contact pressure could be up to 2 GPa, as described by Buryta et al. [30]. Even if this is definitely tool-material dependent, it already clearly defines what can be meant by "severe contact conditions".

Chip formation is a complex process with various physical phenomena. It starts at a microscopic scale with fractures and finally grows at a macroscopic level. Lagrangian formulation with node separation criterion (Fig. 1.7a) [31] or Lagrangian formulation with adaptive mesh and remeshing (Fig. 1.7b) [32] have been successfully employed in some simulations. ALE simulations have also been employed as they provide the possibility to avoid any separation criterion and direct access to the steady state cutting regime.

1.1.2 Metal forming

Metal forming is a metalworking process based on mechanical deformation [33]. The main objective is to produce a part into the final shape with a minimal material removal. As widespread manufacturing methods, many different metal forming operations have been developed [9]. Based on the type of stresses applied to the work material, these

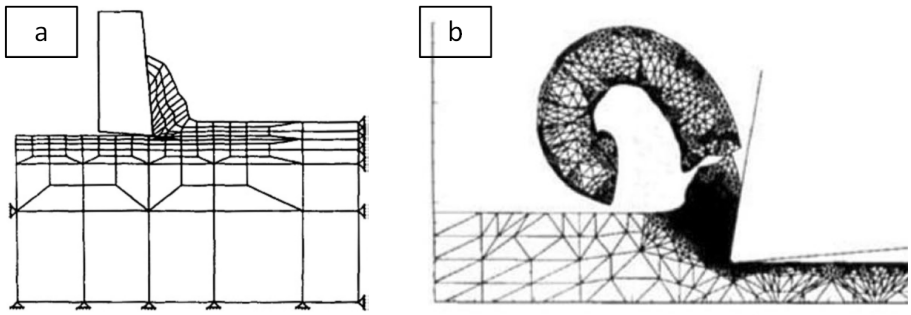

Figure 1.7: Numerical modeling of machining using Lagrangian formulation with (a) node separation criterion [31], and (b) adaptive mesh and remeshing [32].

processes could be divided into several types, as shown in Fig. 1.8 [34].

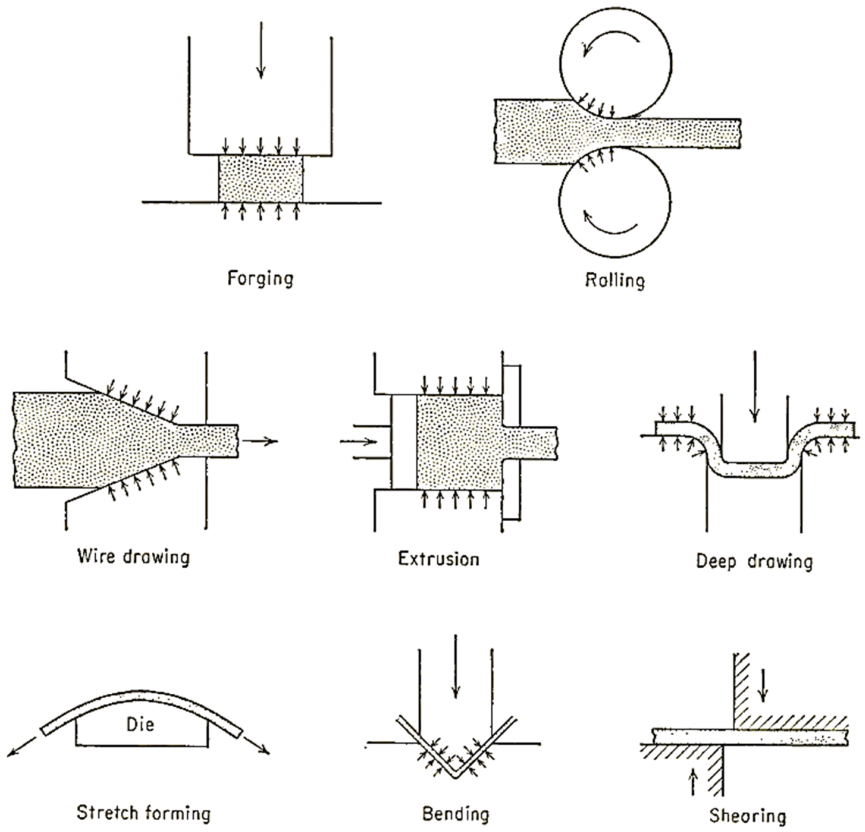

Figure 1.8: Typical forming operations [34].

Metal forming processes could be generally separated into two categories: bulk deformation and sheet metalworking.

- Bulk deformation, such as rolling, forging, extrusion and wire drawing. It is characterized by significant deformations and massive shape changes, but mostly by the surface area-to-volume of the work which is relatively small [4].
- Sheet metalworking, such as deep drawing, bending, shearing. Those operations are performed on metal sheets, strips, and coils. The surface area-to-volume ratio of the raw material is high; thus, this ratio is a useful means to distinguish bulk deformation from sheet metal processes.

During the metal forming process, the severe plastic deformation for the production of metal objects results in critical contact conditions at the tool/work material or die/work material interfaces. For example, during the cold forging process of steels, the contact pressure and temperature at tool/work material interface could be up to 2.5 GPa and over 600 °C [35].

Fig. 1.9 is an example of the contact pressure distribution over the die radius in sheet metal forming process. For reference, each graph's inset shows a three-dimensional representation of the deformed blank at a particular instant during the simulation [36]. It indicates that the contact pressure could reach 1.25 GPa at a particular location on the die radius.

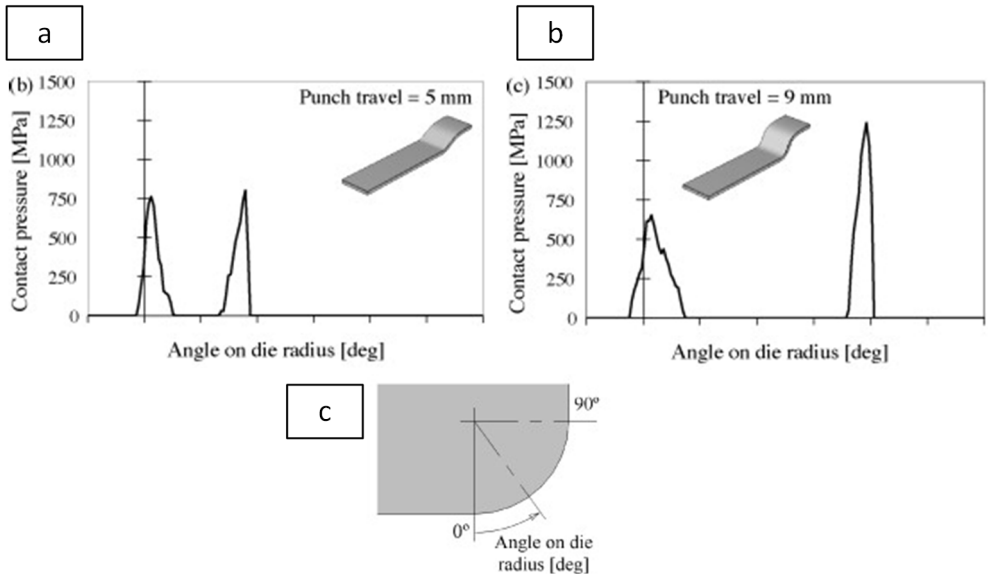

Figure 1.9: Predicted contact pressure distribution over the die radius (a) punch travel=5mm, (b) punch travel=9mm, and (c) corresponding inset [36].

Groche et al. [37] summarized the mechanical conditions in bulk metal forming tribometers. Fig. 1.10 shows the normalized contact normal stress (absolute value divided by the flow stress of 700 MPa) at the billet–die interface at three different strokes of the double cup extrusion test, which was first introduced in [38]. The friction coefficient

was set to 0.03 at all interfaces. The zero value on the y-axis is consistent with the position of the lower punch. It indicates that the appearing contact normal stresses are hardly exceed the material's flow stress.

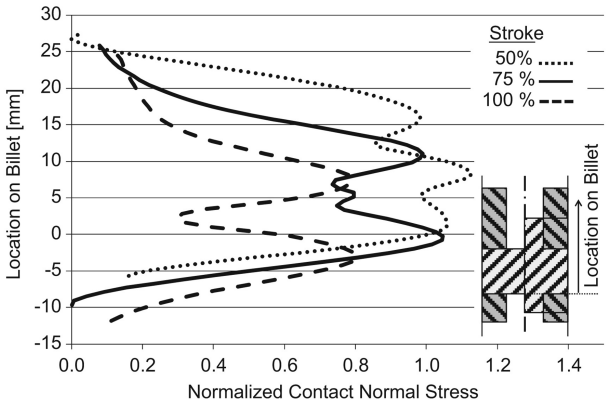

Figure 1.10: Normalized contact normal stress (DCE) [37].

Hot forming is a widely used metal forming process in vehicle industries. Liu et al. [39] investigate the hot forming process of the ultra high strength steel (UHSS) to improve the springback and formability. Fig. 1.11 shows the stages of hot forming. The blank is heated at 950 °C for around 180 s to guarantee homogeneous austenitization. Then the blank is transferred to the die to finish the forming process with critically large deformations. After the quenching process, the austenite transforms into martensite, which results in an increase in strength.

1.1.3 Friction stir welding

Friction stir welding (FSW) is another high speed manufacturing process with high rotating speed. It is a fast and efficient process developed to joint metals without any additional material input, especially for aluminum alloys. Recently some researchers succeeded in jointing dissimilar metals [40] by FSW. The schematic of the friction stir welding set-up is shown in Fig. 1.12. During the welding process, the rotating tool is traversing along the joint line (Fig. 1.12a) with a small tilt angle (Fig. 1.12c). An advancing side and a retreating side are formed (Fig. 1.12b). Heat energy is generated due to the friction between the rotating-traversing tool and work material. Once heated and softened along the joint line, the latter flows to the backside where it then cools down and forms a weld with a high strength [41].

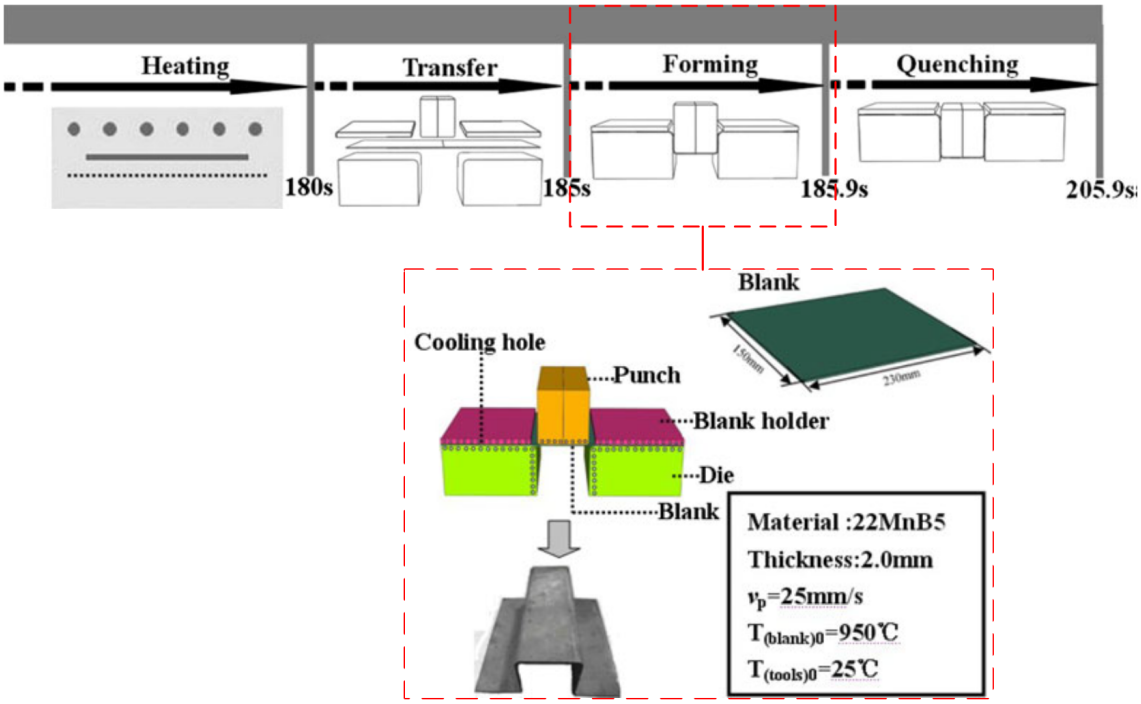

Figure 1.11: Stages of hot forming process [39].

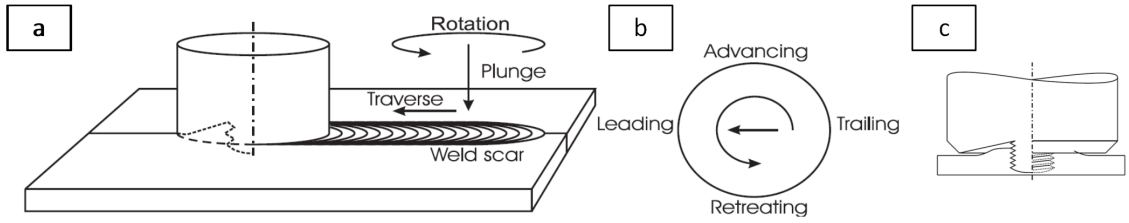

Figure 1.12: (a) Schematic of the weld set-up and definition of orientations, (b) top view, and (c) side view [41].

Three welding parameters control the weld joint's quality in FSW: the tool's rotation speed, welding speed, and welding pressure. The tool's or sometimes called pin's rotation speed and welding speed can be easily controlled, while the welding pressure is a consequence of the processing configuration, i.e. parameters, geometry and work materials. The tool's rotation speed typically ranges from 150 rpm [41] to 16500 rpm when jointing aluminum alloy thin sheets [42]. The welding speed can reach 800 $mm \cdot min^{-1}$ [43] and the welding normal force F_n could range from 1000 to 7000 N [44] when welding aluminum plates.

Fig. 1.13 is a sample of numerical simulation of the FSW process. The schematic of the thermo-mechanical model is shown in Fig. 1.13a whereas Fig. 1.19b shows the

temperature distribution at the top surface for the welding condition of 1500 rpm and 150 mm/min. One can see that the maximum temperature can exceed 550 °C.

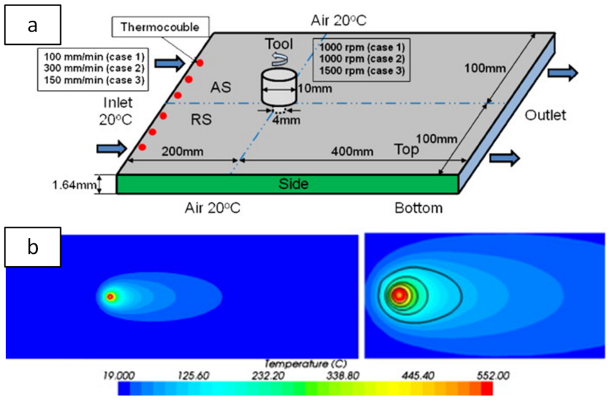

Figure 1.13: Schematic of the thermo-mechanical model (a) and the temperature distribution of 1500 rpm and 150 mm/min (b) (unit °C) [45].

The principle of the process itself makes it highly severe. Joining is achieved by mixing the two targeted materials in a semi-solid state due to the intense thermal energy dissipated by friction. Previous research shows that the maximal equivalent strain varied from 6 [46, 47] to 133 [48] under different welding conditions. Fig. 1.14 is a sample of the simulated equivalent plastic strain field by ABAQUS Explicit in the longitudinal cross section along the joint-line after 10 s with two panels in AA2024-T3. The welding speed is 2 $\mathrm{mm \cdot s^{-1}}$ and the rotating speed is 400 rpm. The maximal equivalent strain is around 133.2.

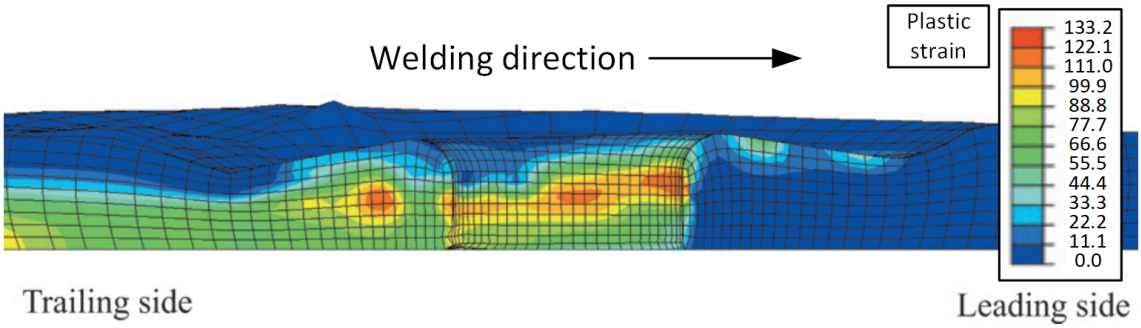

Figure 1.14: Plastic strain field in the longitudinal cross section near the tool/matrix interface 10.0 s [48].

Milagre et al. studied the microstructure characterization of the AA2098-T351 alloy welded by FSW process. Fig. 1.15 presents the relationship between top surface

microhardness and calculated temperatures at different depths from the cross-section. It is clearly that the high temperature at the welding joint leads to the decreasing of microhardness. The microhardness at 16 mm away from the centerline dropped compared with the base metal. This phenomena is also reports by some other researchers [49, 50]. This overaging behavior is due to the coupled effect of temperature and forging-extrusion of the material [50].

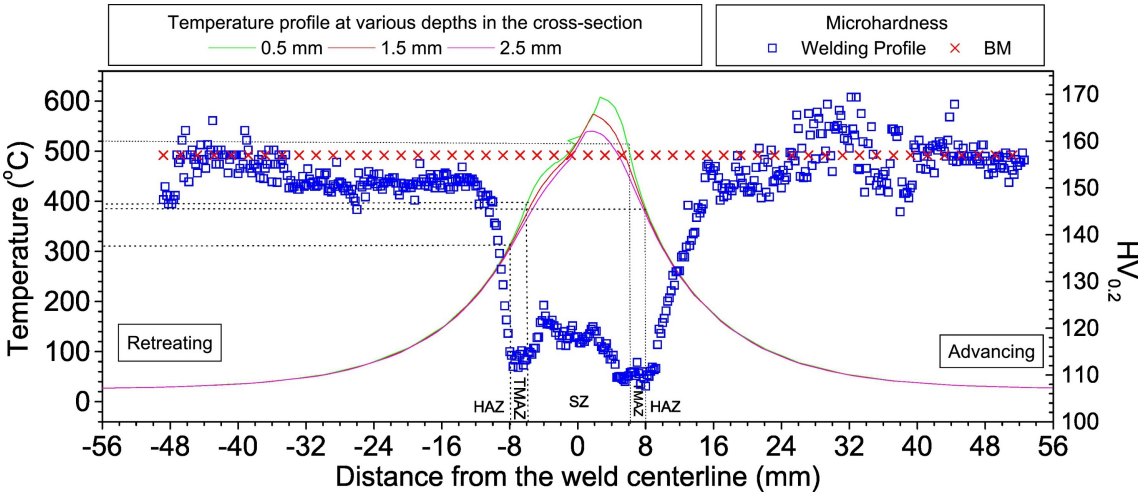

Figure 1.15: Relationship between top surface microhardness profile and temperatures calculated at different depths from the cross-section [51].

Numerical modeling for FSW also have been developed since the 1990s using whether a Lagrangian, Eulerian, ALE or even Coupled Eulerian-Lagrangian (CEL) formulations. The primary objective is to assess the metallurgical state, deformations, residual stresses of the joint materials [52]. In addition, the metallurgical state is one of the key parameters which affect the thermal and mechanical properties of the final joint [53]. However, due to the critical deformation and distortion during the FSW simulation process, the mesh quality decreases, and numerical problems may occur. Therefore adaptive meshing or remeshing techniques have to be applied.

The boundary conditions are difficult to determine, particularly considering the heat flux at tool-wrok materials interface [52].

Assidi et al.[54] investigated the FSW of Al 6061 aluminum plate with an untreated concave tool using ALE formulation implemented in commercial code Forge3 to compute the contact and frictional surface accurately. The workpiece follows the Hansel–Spittel constitutive model. Coulomb friction model and Newton friction model are compared. They conclude that the welding forces and tool temperatures are highly sensitive to small variations of friction. Fig. 1.16 shows the normal stress distributions using either the Eulerian (Fig. 1.16a) or ALE (Fig. 1.16b). It indicates that higher values are obtained in the ALE case, especially at the probe's tip.

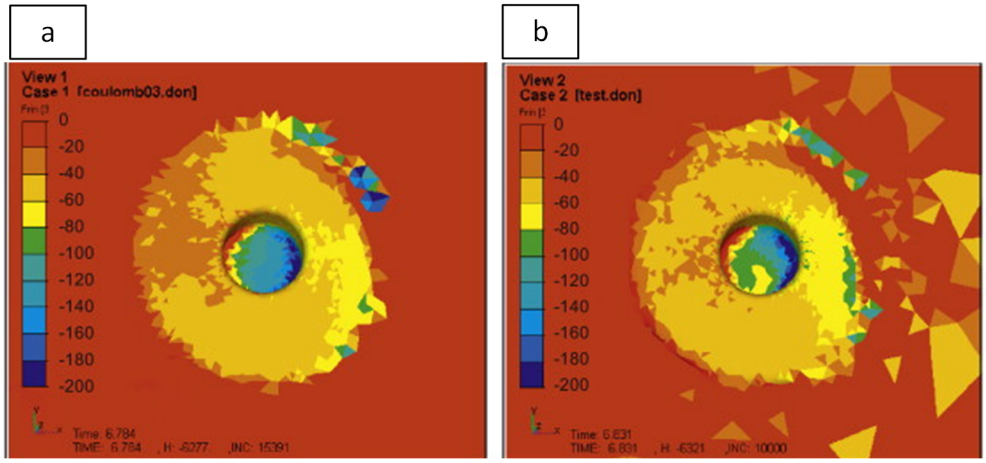

Figure 1.16: Normal stress distributions using either the Eulerian (a) or ALE (b) [54].

Recently, the Coupled Eulerian-Lagrangian (CEL) formulation is another option to analyze the thermo-mechanical behavior in the FSW process. In the CEL formulation, the tool is considered a Lagrangian part, while the workpiece applies the Eulerian approach. The interaction between the tool and the workpiece is implemented based on the immersed boundary method [55]. The mesh for representing the workpiece was stationary, and thus, the material could move freely through the mesh without causing mesh distortion [56]. For example, Tongne et al. made use of the CEL formulation to study the FSW of aluminum alloy with trigonal tools (Fig. 1.17) [57, 58]. The maximal equivalent plastic strain is around 24.57.

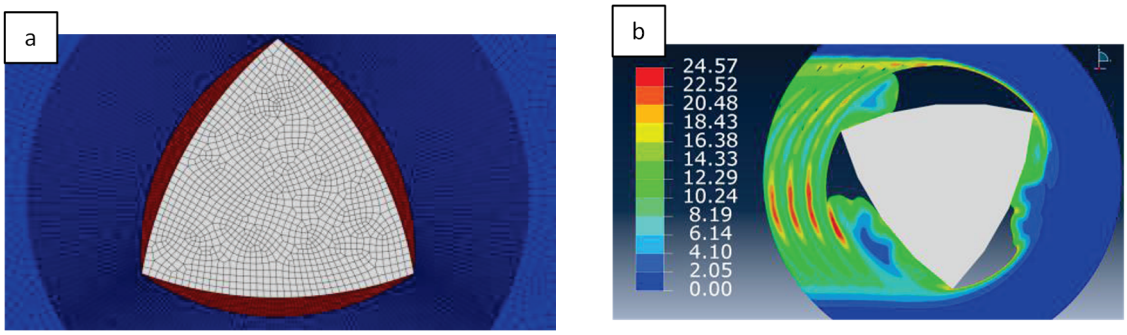

Figure 1.17: (a) Parts configuration at the initial step of the process, and (b) equivalent plastic strain [58].

In the FSW process, welding defects are obviously the negative factors for the welding joint performance. There are several concepts to predict them, such as the free

surface evolution in the model, the analysis of the in-process damage evolution, using the information on the material flow path and the material velocity [56]. In any case, the heat generation and resulting temperature fields are the key outputs in the thermo-mechanical analysis. They directly govern the metallurgical processes that can be activated, such as dynamic recrystallization [59] and solid-state bonding [60]. The heat is mostly generated at the contact interfaces between the welding tool and the work material. Thus, in order to perform a relevant thermo-mechanical analysis, not only material properties and processing parameters have to be properly selected [56], but also the way the contact occurs, i.e. the way friction and heat transfer are modeled.

1.1.4 Braking

Besides the manufacturing process, special configurations with severe contact conditions can be found in the literature. The disc braking process is selected as an example. In general, The disc braking system consists of two-part: the rotating part of a wheel's disc against the fixed brake pads. Fig. 1.18a is the assembly of the vehicle's disk brake system. Fig. 1.18b shows the schematic of this configuration [61]. During the braking process, the friction between the disc and pads causes the system to slow down or stop.

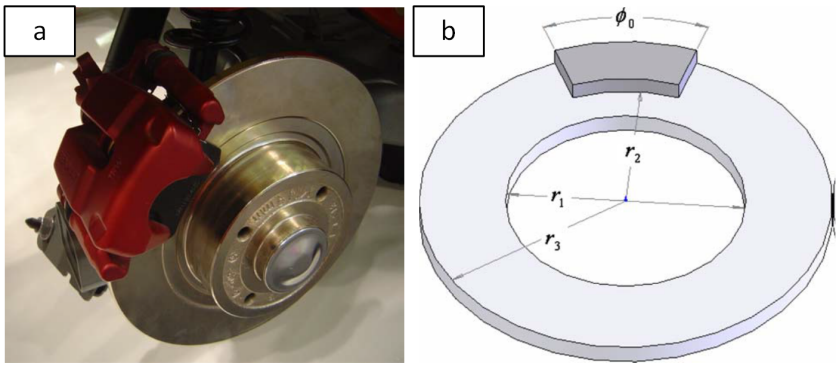

Figure 1.18: (a) Assembly and (b) schematic of the disk brake [61].

In order to improve efficiency, high contact pressure and friction coefficients are aimed between discs and pads to achieve more significant friction force and braking capacity. However, the high sliding velocity leads to critical contact conditions at the interface with exceptionally high contact temperatures. The thermal degradations due to the thermal stress may cause brake fade, premature wear, brake fluid vaporization, bearing failure, etc. [62]. Therefore, researchers carried out various experimental and numerical approaches to investigate the frictional behavior and the thermal performance of the braking system. A brief review of experimental set-ups will be presented in

Section 1.2.3.

Numerical models have been developed to assess the local contact conditions. Fig. 1.19 presents the temperature and Von Mises compression stress distribution of grey iron disk. The evaluation of the vehicle dynamics estimates the heat flux transfer into the pin. The braking speed is 19.4 $m \cdot s^{-1}$, the brake duration is 1 s, the macroscopic pressure exerted during braking actions is 5 MPa. Simulation temperatures up to 450 °C and stresses up to 450 MPa have been reported. Collignon et al. [63] also made use of the heat flux estimated by an experimental approach to predict the temperature distribution by a 3D numerical model. The heat loss due to natural convection and radiation is considered. The maximal temperature is over 750 °C, and the temperature distribution indicates the presence of significant thermal gradients in the disc.

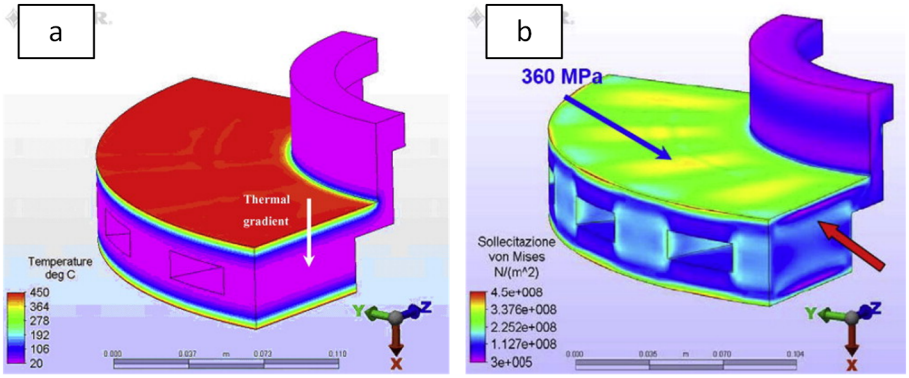

Figure 1.19: Temperature (a) and Von Mises compression stress (b) distribution at the end of braking [64].

In order to simulate those critical contact condition, Kim et al. [65] examined the tribological behavior of NAO type brake linings with a speed of 22.2 $m \cdot s^{-1}$ and pressure of 3 MPa. Cho et al. [66] investigated the frictional characteristics between gray cast iron and automotive brake linings. The contact pressure was only around 0.79 MPa whereas the sliding velocity was set up to 2.6 $m \cdot s^{-1}$, confirming the high speed sliding nature of these configurations.

1.2 Tribological set-ups under severe contact conditions

In each of the previously listed applications, the tribological aspects play a key role and significantly influence efficiency, productivity, tool failure, economic loss, and ecology. It is thus important to have a deep understanding of the response of such complex

tribological systems. The most common approach is to develop a dedicated test bench to perform friction and wear testing.

This section summarizes the experimental methods to investigate a sliding contact under severe contact conditions depending on the targeted application. In any case, intensive plastic deformation of the work material, high contact pressure, critical temperature distribution associated with an intense friction behavior are highly concerned [67].

1.2.1 Developments in machining

1 st type: Metalworking itself

The first type of experimental approach is based on using the metalworking process itself [68, 69, 70, 71]. In general, a simplified configuration is selected to really focus on the fundamental mechanisms. For example, in machining, the experimental set-up is based on two parts: a tube made of the investigated material and a cutting tool made of the relevant substrate and coating [7]. For example, Arrazola et al. [71] performed an orthogonal machining experiment, as Fig. 1.20 shows, plunge turning of thin webs on AISI 4340 steel using an uncoated carbide cutting tool.

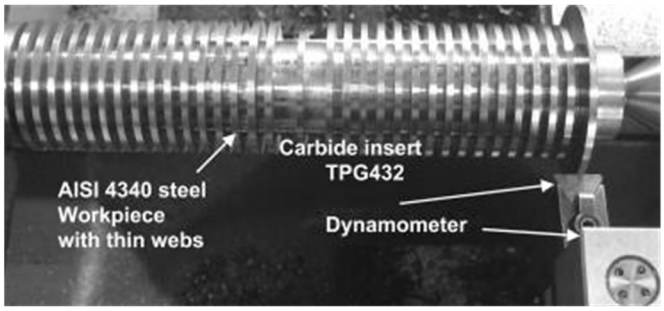

Figure 1.20: Tribological test for orthogonal turning [71].

In order to identify the friction coefficient at the tool-chip interface, as Fig. 1.21 shows, the cutting force and feed force are measured with a dynamometer and DAQ system. Based on the research of Albrecht [72], the resultant of the cutting and feed forces could be considered as the resultant force of P and Q , where P represents the force resulting from localized phenomena close to the cutting edge and Q represent the force on the rake face. The critical feed rate determines the Q and P force. The friction coefficient from Albrecht's theory is only determined by the Q force, and the P force is not considered. The major drawback of this method is that Albrecht assumes that the P force remains constant, and so is the contact pressure with various feed rates. However, the feed rate has effects on the strain, strain rate, and temperature, thus this

assumption can be highly questioned [71].

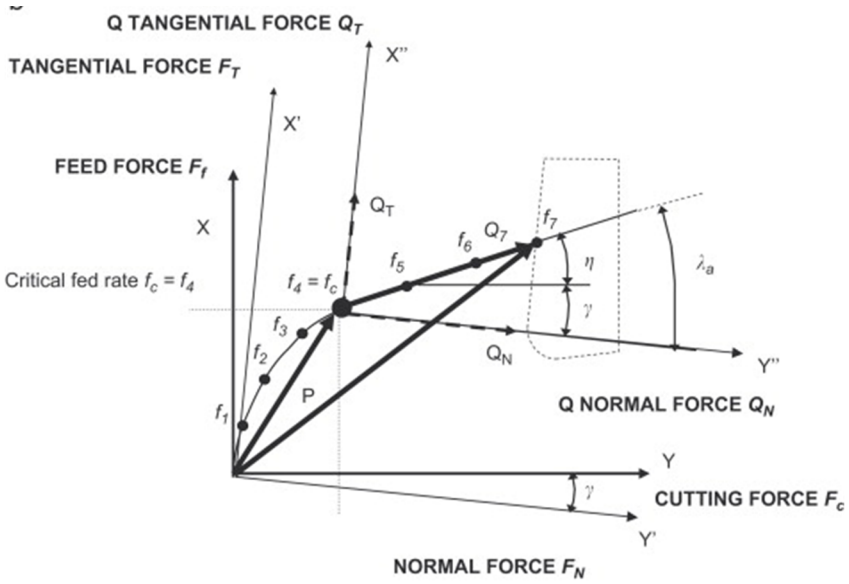

Figure 1.21: Forces decomposition [71].

Thus the split-tool methodology was developed to overcome the drawbacks [73, 74]. As Fig. 1.22 shows, the cutting tool is divided into two separated parts along the rake face by a small gap so that the chip can not flow into it. The contact pressure and shear stress are measured in each section of the tool. Therefore the distribution of friction and normal stress could be presented along the rake face of the cutting tool. However, the manufacturing of the split tool is too complex, and it is not piratical to coated tools [75, 76].

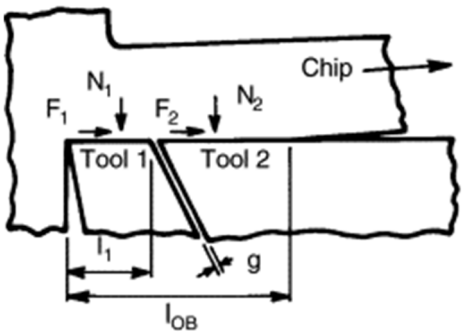

Figure 1.22: Schematic view of the split tool [75].

Recently, Ortiz-de-Zarate et al. [76] employed the Partially Restricted Contact Length Tools (PRCLT) to determine rake face friction and normal contact stress distributions by

orthogonal machining. As Fig. 1.23 shows, the insert has a rectangular groove of depth that stops short of the cutting edge, but extends beyond the contact length between the chip and tool. The work material is AISI 1045 carbon steel with TiN-coated or uncoated cemented carbide tools. The cutting speed is from 50 to 200 $\mathrm{m \cdot min^{-1}}$ and the feeds of 0.2 and 0.3 $\mathrm{mm \cdot rev^{-1}}$.

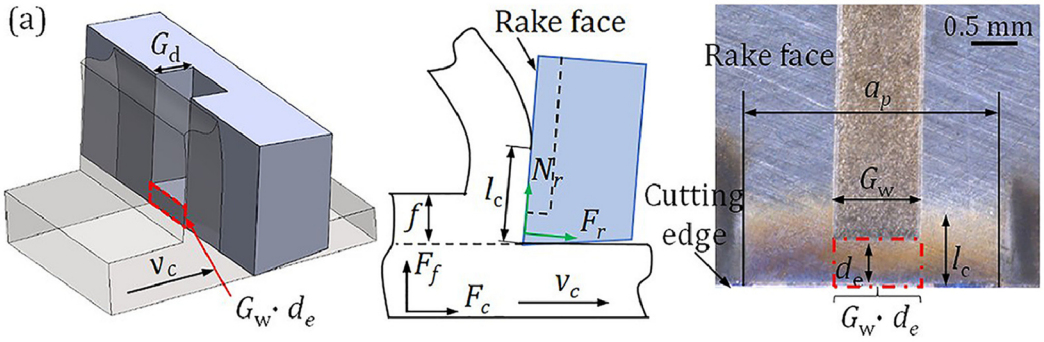

Figure 1.23: Basic description of the PRCLT [76].

In general, this method is an appropriate method to simulate the relevant friction conditions. The advantages are:

- Cutting forces and temperature could be measured during the test.
- The contact zone left by the cutting process at the tool's surface or the workpiece could be analyzed after the test.
- The geometry, microstructure of the chips could be analyzed after the test.

However, this method does not consider the variations of the local contact conditions along the tool-work material interface [77] due to the changes of local sliding velocity, contact pressure, and temperature (Fig. 1.24). Only macroscopic parameters can be measured. As a consequence, there are still some limitations from the tribological point of view.

2 nd type: Conventional tribometers

The second approach is to use a tribometer to dissociate the frictional behaviour from the material removal phenomenon. For the conventional tribometers, various contact conditions could be simulated based on the requirement of the actual metalworking process, such as coated/uncoated, dry/lubrication, room/high temperature, etc.

Most of the conventional tribometers are closed tribosystems. Thus the pin, ball, or block always rubs on the same contact trace. However, when compared to metal cutting, the tools never continuously rub within the same trace against the workpiece,

which corresponds to an open tribosystem. Additionally, conventional tribometers are hardly able to cover the whole range of local contact conditions along the tool-work material interface [77].

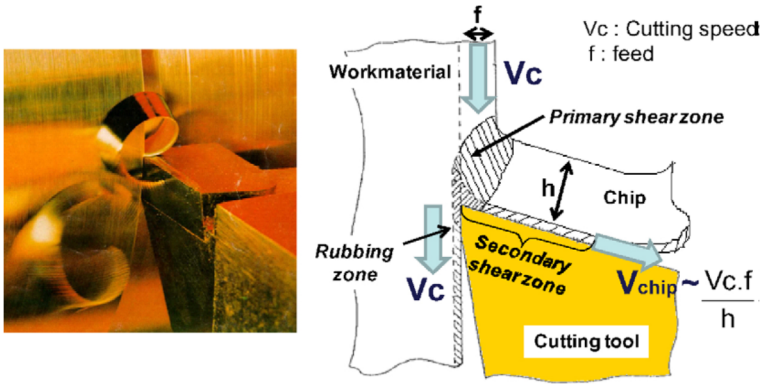

Figure 1.24: Illustration of the various strategic zones [11].

One of the most widely used 'universal' tribosystem to evaluate friction and wear is the pin-on-disc tribometer.

As Fig. 1.25 shows, it consists of two parts, a pin with a particular load in contact with a rotating disc. The friction coefficient could be calculated by the measured normal forces F_n and tangential forces F_t by the force transducer. As a 'universal' tribosystem, the basic pin-on-disc tribometer has been used to perform fundamental studies. It has been modified to simulate the various friction pairs and contact conditions that could be found in metalworking processes, such as cutting, forging, stamping, rolling, with various contact conditions, dry, lubricated, high temperature, etc.

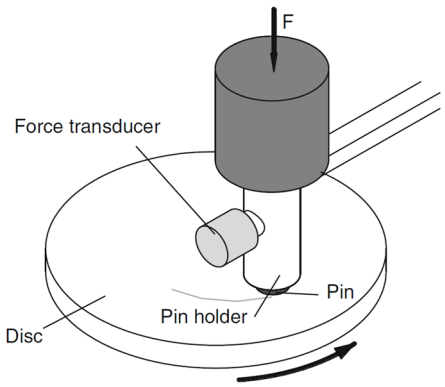

Figure 1.25: Pin-on-disc tribosystem [9].

.

Fig. 1.26a is a high contact pressure pin-on-disc tribometer from Sterle et al. [78]. They increased the structural strength of the pin-on-disc tribometer with WC-Co ball in contact with 42CrMo4 disc (Fig. 1.26a) so as to increase contact pressure up to 1.3 GPa and generate plastic deformation. However, the sliding speed is still limited up to 1 $m \cdot s^{-1}$ and tests are performed at room temperature.

The second modified tribosystem is the high speed pin-on-disc tribometer (Fig. 1.26b) by Kagnaya et al. [79]. It is employed to study the wear mechanisms of a WC–Co cutting tool against AISI 1045 steel. A large sliding speed range from 1 to 10 $m \cdot s^{-1}$ is considered with a contact pressure however lower than 5 MPa.

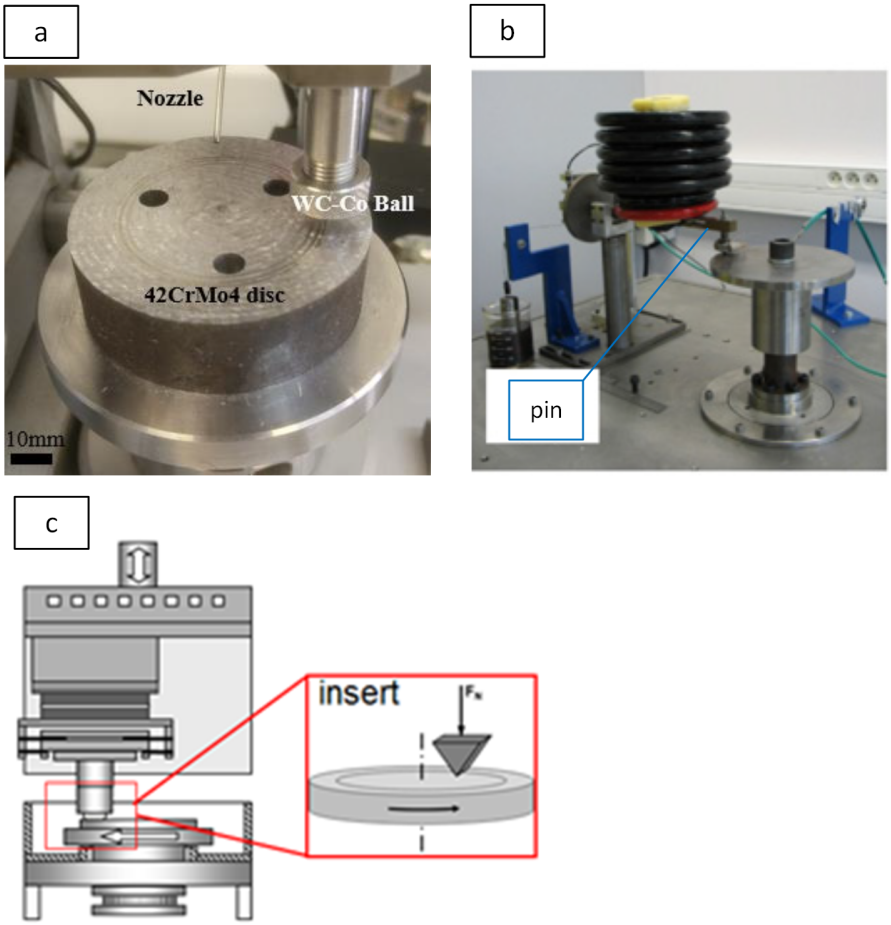

Figure 1.26: Modified pin-on-disc tribosystem: (a) Sterle's tribometer[78], (b) Kagnaya's tribometer [79], and (c) Bollig's tribometer [80].

The third configuration (Fig. 1.26c) is designed by Bollig et al. [80] to simulate the drilling process. The friction coefficients could be calculated from ball-on-disc tests or insert-on-disc tests with a normal force F_n of 20 N or 40 N. The sliding velocity could

reach 10 $m \cdot s^{-1}$ with the carbide insert on the AISI4140 disc.

To sum up, the advantages of the conventional tribometers are as follows:

- They can be seen as fast and easy to run set-ups only requiring the manufacture of samples and/or holders;
- They can be used to perform fundamental studies, sensitivity and qualitative analyses using the actual tool material pairs;
- The macroscopic friction coefficient could be estimated under the given contact configuration and based on some hypotheses.

Nevertheless, they still present some important limitations:

- The contact conditions (temperature and/or contact pressure and/or sliding velocity) are not always consistent with those observed in the real metalworking process;
- As closed tribosystem, the pin, ball, or block rubs continuously on the same contact track. A repeated work hardened layer or the generation of a wear debris bed can influence the tribological response in some way and thus distort the analyses;

3 rd type: Specially-designed tribometers

Due to the previously identified limitations of the conventional tribometers, researchers started to propose an alternative and build specially-designed tribometers. These tribosystems are employed to identify the characteristics of various contact conditions specifically dedicated to the machining process. One important aspect is that they are all based on an open contact configuration which appears to be of primary importance. Several examples are presented below.

In Fig 1.27a, Olsson et al. [81] employed a special equipment layout where a cutting tool is placed in front of the pin rubbing on a tube's flat face. During the friction test, the cutting tool could refresh the surface so as to avoid the pin running on the same track. The sliding velocity is similar to the cutting process, whereas the contact temperature is supposed to be relatively close to the actual one. However, the average contact pressure is only 15 MPa due to a lack of rigidity of the system and a risk of chip formation in front of the pin [82].

Hedenqvist's tribometer [83] is shown in 1.27b. The advantage of this configuration compared to the previous one is the sufficient sliding velocity (up to 3 $m \cdot s^{-1}$) while not using a cutting tool. This makes the system easier to handle and still enables the

continuous introduction of a fresh counter material surface at the interface. However, there are certain drawbacks associated with its use such as the contact pressure still limited (15 MPa) to simulate the contact conditions in the metal cutting process.

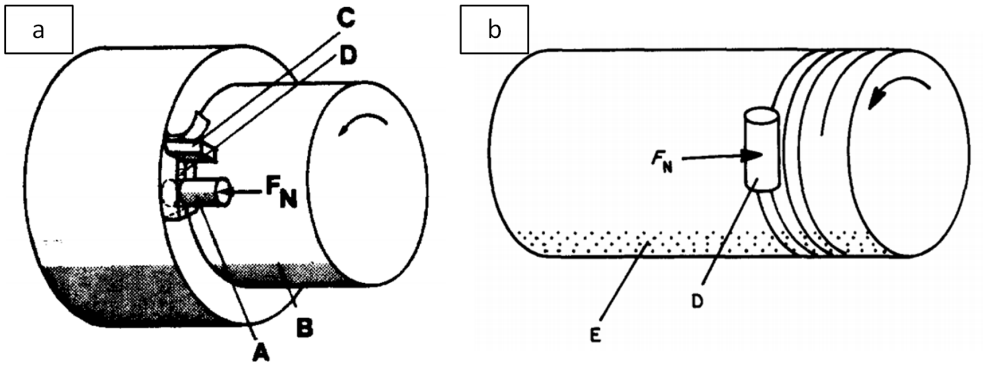

Figure 1.27: Special-designed tribometers:(a) Olsson's tribometer [81], (b) Hedenqvist's tribometer [83].

Fig. 1.28a shows the tribometer designed by Zemzemi et al. [82], based on the principle of Olsson et al. [81] and fitted on a lathe. The plastic affected surface is refreshed by the cutting tool, and the pin is in contact with the refreshed surface. The contact pressure is estimated to 1 to 2 GPa and the sliding velocity can reach 3 $m \cdot s^{-1}$, which was expected to emulate the contact conditions obtained during the cutting process.

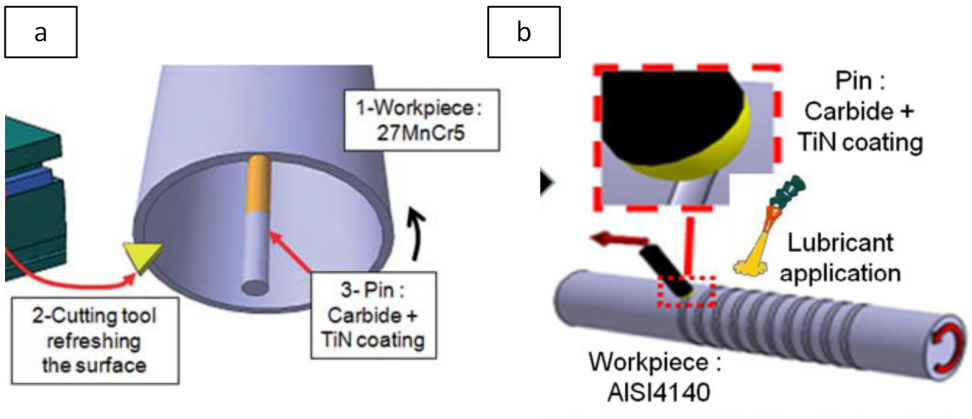

Figure 1.28: Special-designed tribometers: (a) Zemzemi's tribometer [82], (b) Claudin's tribometer [84].

Based on the Zemzemi's development, a new tribometer is designed by Claudin et al. [84] with an extended speed range. The principle of this tribometer is shown in Fig. 1.28b. This device is based on a CNC lathe with a more rigid structure compare to

the Zemzemi's one. The hertzian contact pressure could reach 3.5 GPa for a AISI4142 steel with the sliding velocity over 6 $m \cdot s^{-1}$ [84] in dry or lubricated conditions. Ben Abdelali et al. [7] used this tribometer to study the interface in dry machining of AISI 1045 steel with a TiN coated carbide tool and sliding velocities up to 5 $m \cdot s^{-1}$.

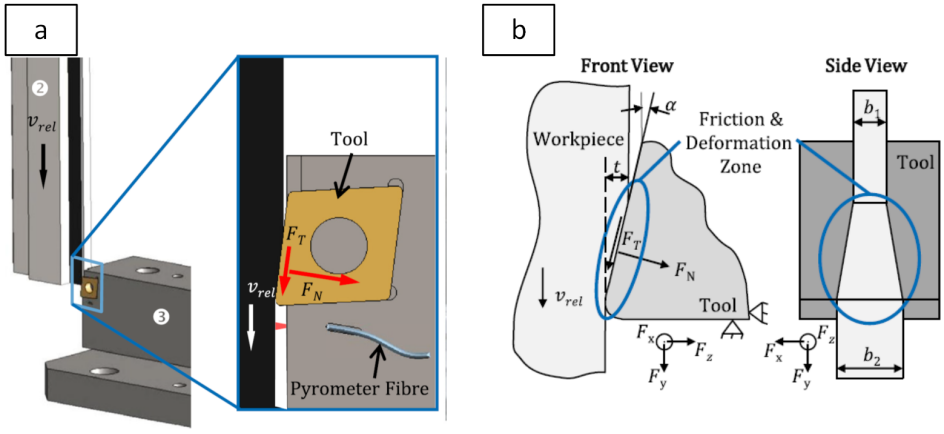

Figure 1.29: Puls' tribometer (a) and kinematic concept (b) [85].

Puls et al. [86, 85] proposed an alternative tribometer in Fig. 1.29 based on a reverse cutting operation. An extremely negative rake angle is used (contact on the flank face) to suppress chip formation, resulting in a simple high speed forming process and plastic metal flow over the tool's inclined plane. The sliding velocity is up to 3.3 $m \cdot s^{-1}$ and contact temperature is estimated to be close to 1000 °C with Carbide WC-6Co tools in contact with AISI1045/Inconel718/AISI4140 workpiece.

To sum up, these specially-designed tribometers for metal cutting could simulate the severe contact in different aspects:

- As open tribosystem, the pin or the cutting tool never rubs on the same trace.
- A wider range of sliding velocities and contact pressures can be covered to emulate the severe contact conditions.

Despite the efforts done, it is still difficult to monitor the changes of local sliding velocity, contact pressure, and temperature (Fig. 1.3) along tool/chip/work material interfaces during the cutting process. As a consequence, there are still some limitations below:

- Only macroscopic parameters such as forces and sometimes a remote temperature, could be measured in-situ;
- Impossible to monitor the local contact pressure or temperature distribution at

the tool-work material interface during the test.

Finally, the Table 1.1 presents a summary of the capabilities including contact type, contact pressure, sliding speed, elastic/plastic contact, open/closed tribosystem, workpiece temperature and test duration time.

Table 1.1: Process characteristics in tribological test of machining.

Author	Contact	Pressure (MPa)	Speed ($m \cdot s^{-1}$)	Elastic/Plastic contact	open/closed tribosystem	Workpiece temperature (°C)	Test duration (s)
Sterle [78]	sphere - flat	900-12500	0.5, 1	plastic	closed	ambient	
Kagnaya [79]	sphere - flat	4.77	0.05-30	plastic	closed	ambient	300-7200
Bollig [80]	sphere - flat		0-10	plactic	closed	ambient	300
Olsson [81]	flat - flat	15	0.83-1.67	elastic	open	ambient	
Hedenqvist [83]	cylinder - cylinder	15	0.42-5	elastic	open	ambient	0.24-36
Zemzemi [82]	sphere - flat	2000	1-3.3	plastic	open	ambient	10
Claudin [84]	sphere - flat	3000	0.16-5	plastic	open	ambient	20
Puls [85]	flat - flat		0.33-3.33	plastic	open	ambient	

1.2.2 Developments in forming

1 st type: Deformation-based tribometer

Tribological set-ups have also been used to reproduce the plastic deformation and frictional behavior in the metal forming process. Deformation kind of tests have been developed in this field such as the ring compression test (RCT) and the double cup extrusion test (DCET) shown in Fig. 1.30 a&b. The RCT was developed by Kunogi [87] in 1954 to qualitatively assess lubrication conditions in metal extrusion. When a plastic ring is compressed between two flat dies, high friction (poor lubrication) leads to an inward flow of the material, while low friction (good lubrication) leads to an outward flow of the material. DCET is commonly used to evaluate the performance of lubricants in cold forging. A cylindrical billet is compressed by a upper punch moving downwards, while the lower punch and the die are fixed [37]. The contact pressure at the billet–container interface could reach 1.2 GPa when forming a AISI 1018 steel [88]. Compared to RCT, DCET could simulate more severe deformation, which is similar to what happens during the cold forging process [88]. In the forming community, both test benches are widely accepted to estimate the friction behavior of the metal-plastic deformation process and evaluate the impact of lubricants.

The Fig. 1.30c describes the Spike forging test, proposed by Lahoti and Altan [89] in 1982 and developed in 1992 by Isogawa and Kimura [90]. The height of the spike extruded into the die cavity is an indicator of the friction conditions and the quality of a lubricating system [91][92]. Despite the fact that the spike height gives information on the overall friction conditions, this test does not allow analyzing friction in detail due to local and time in-homogeneity.

The set-up (Fig. 1.30d) proposed by Wanheim and Bay [93, 94] is one of the deformation-based tribometer developed to investigate friction coefficient of a deformed specimen under extremely high contact pressure and torque. Due to the container, an intense hydrostatic pressure up to 800% of the yield stress could be reached for example on an aluminum specimen [94].

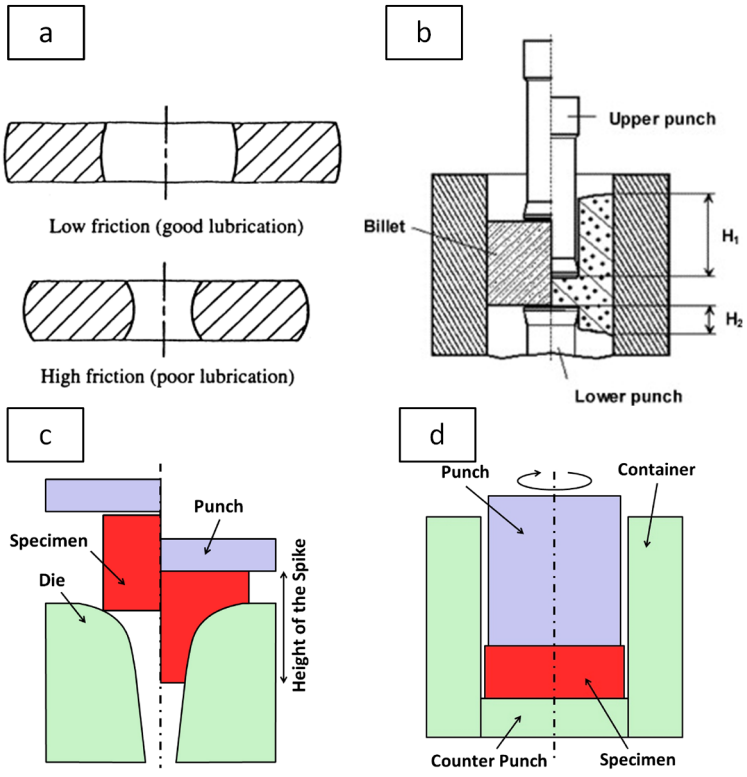

Figure 1.30: Tribometers: (a) ring compression test [95], (b) double cup extrusion test [96], (c) Spike test [37], (d) Wanheim & Bay tribometer [37].

2 nd type: Conventional tribometers

The previous set-ups are characterised by a "forming" type of configuration and especially by a low sliding amplitude or a highly confined tribosystem. They might be difficult to set but most of all, do not provide a direct access to the friction coefficient.

Within a cold forming context, the twin-disc machine [97] in Fig. 1.31a is employed to simulate the rolling process with contact pressure up to 750 MPa and sliding velocity up to 4 $mm \cdot s^{-1}$. Fig 1.31b shows the SRV4 pin-on-disc tribometer [98] which is employed to investigate the surface enlargements and elevated temperatures in cold forging process. The contact temperature is over 400 °C with a normal load of 2000 N.

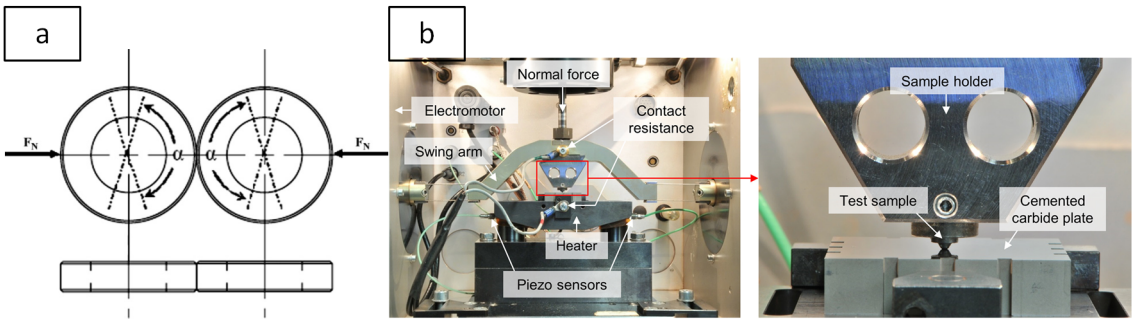

Figure 1.31: (a) Twin-disc machine [97], and (b) SRV4 pin-on-disc tribometer [98].

.

By going through the literature, one can observe that hot forming and especially hot stamping generated a lot of studies as specific phenomena occur at elevated temperature. The high-temperature tribological process is indeed critically complicated (Fig. 1.32a) due to microstructural changes; thermal softening; surface chemical and morphological changes due to oxidation and diffusion; deterioration of the surface and bulk material as a result of adhesive/abrasive wear and thermal fatigue [99]. These changes tend to occur at or close to the interface.

As an example, the most commonly used pin-on-disc tribometer (Fig. 1.25) could be employed to simulate the bulk-forming process as well. For example, Ghiotti et al. [101] used the high-temperature pin-on-disc tribometer (Fig. 1.33) to investigate the characteristics of sheets under hot stamping conditions. Pin is made of the hardened hot working tool steel AISI H11, while the disc is made of the 22MnB5 with Al-Si coating. In order to simulate the industrial hot stamping conditions, the disc is heated up to 900 °C using a specific heating chamber while the pin is kept at room temperature to simulate the dies. Despite a sliding velocity limited to 0.01 $m \cdot s^{-1}$, contact pressures up to 25 MPa could be achieved.

Simple sliding configurations have also been developed as the upsetting-sliding tribometer shown in Fig. 1.34a. The workpiece specimen is first heated up in a furnace and then moved towards as a special tooling to generate the contact via a contactor. As the specimen are relatively simple, the physical and chemical properties of the coating and substrate can be easily respected [37]. The friction coefficient can be calculated with the normal forces F_n and tangential forces F_t measured during the test. This configuration has been employed for example to study the contact between AISI 1045

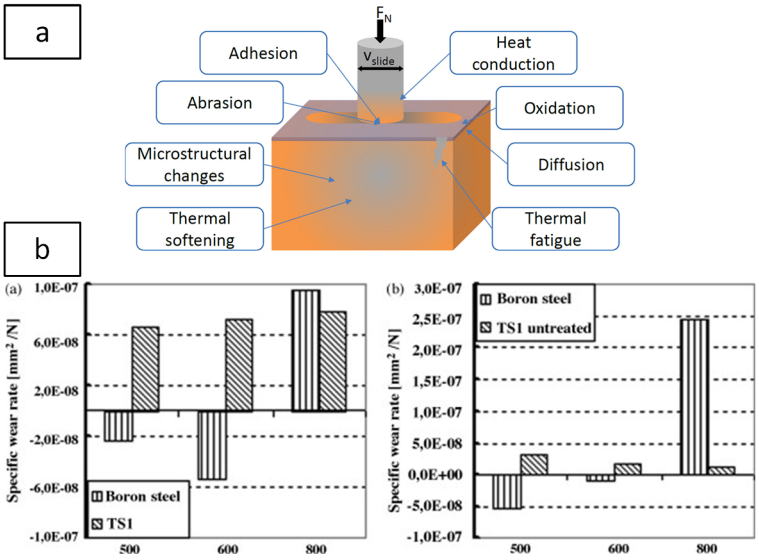

Figure 1.32: (a) Complexity of high temperature tribology by har[99], (b) specific wear rates of treated/untreated tool steel [100].

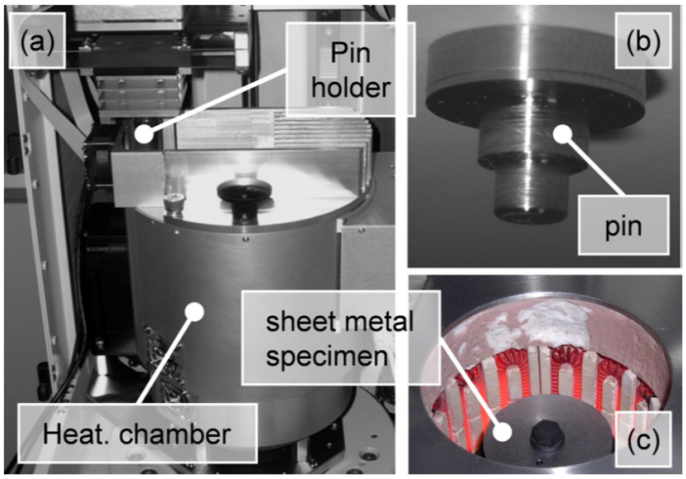

Figure 1.33: Modified pin-on-disc tribosystem for forming: high-temperature tribometer by Ghiotti et al [101].

steel and H13A carbide with 1.25 GPa of contact pressure, a sliding speed up to 0.4 $m \cdot s^{-1}$ and a maximum initial temperature of 1000 K [102].

Hardell et al. [97, 100, 103, 99] and Courbon et al. [104] focused their activity on the tribological performance of different tool materials at elevated temperature. Most of their experiments run on an Optimol SRV reciprocating configuration (Fig. 1.34b), were performed at elevated temperatures (up to 800°C) to study the frictional behavior

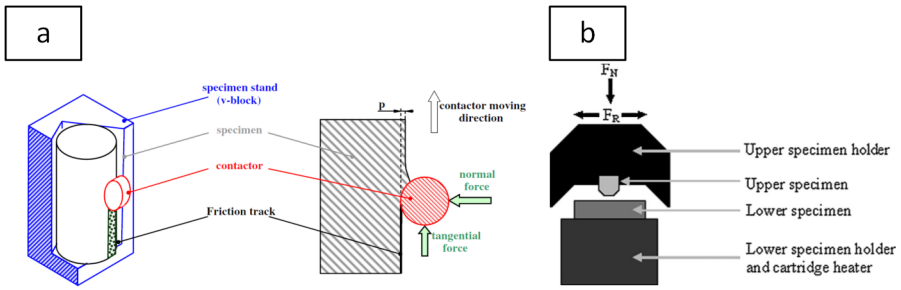

Figure 1.34: (a) Upsetting-sliding tribometer [102], and (b) Optimol SRV reciprocating test [97].

.

and wear mechanism of the hot stamping process or hot rolling process. Consistent coating and surface treatments were considered and the results indicate that frictional behavior and wear mechanism is significantly impacted by the operating temperature (Fig. 1.32b). Critical phenomena such as material transfer and oxidation wear are drastically amplified.

3 rd type: Specially-designed tribometers

In order to alleviate the limitations of conventional tribometers, dedicated set-ups have also been developed in this field. One common characteristic is to generate an open contact configuration compared to the previously identified set-ups.

Specific tribological tests targeting stamping conditions are shown in Fig. 1.35. Cora et al. [105] studied the wear of stamping dies during forming of ultra/advanced high strength steel sheets using an unidirectional sliding configuration. The die wear test system (Fig. 1.35a) is employed to simulate the contact conditions instead of the real stamping process. Samples with different coatings were tested along a accumulated 2 km contact distance with a sliding velocity of 0.33 $m \cdot s^{-1}$ and a normal load of 200N, but at room temperature.

Boher et al. [106] investigated the wear and mechanism of dies in hot stamping of high strength boron steel with the deep-drawing process simulator [106]. The temperature of the strip slides on the tool is around 730 °C and contact pressure reaches 20-30 MPa with a sliding velocity of 0.25 $m \cdot s^{-1}$.

Galling is a severe adhesion phenomenon typically observed when running a contact at elevated temperature. Deng et al.[107] studied galling on stamping tools used in hot forming of Al–Si-coated ultra-high-strength steel. They employed the specifically designed tribometer shown in Fig. 1.36a. The pin is made of hardened tool steel in contact with the boron steel strips. The temperature of the latter is commonly increased

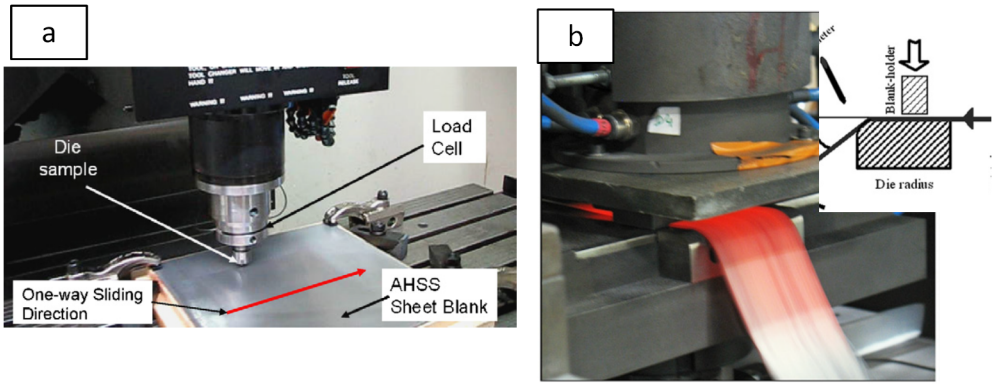

Figure 1.35: Tribometers under stamping conditions: (a) die wear test system by Cora et al [105], (b) deep-drawing process simulator by Boher et al [106].

to 600 to 750 °C with the contact pressure from 5 to 15 MPa. They observed that the test temperature was an important factor in terms of the galling severity in the galling evaluation,

Gaard et al. [108] employed the slider-on-flat surface (SOFS) tribometer 1.36b to investigate the initiation of galling in sheet metal forming. A disc-shaped tool slides against the sheet material with contact pressure around 1 GPa at a velocity of 3.3 $mm \cdot s^{-1}$. Despite the fact that tests were performed at room temperature, they reported the friction coefficient which was relatively steady with the value around 0.2 for different sliding conditions.

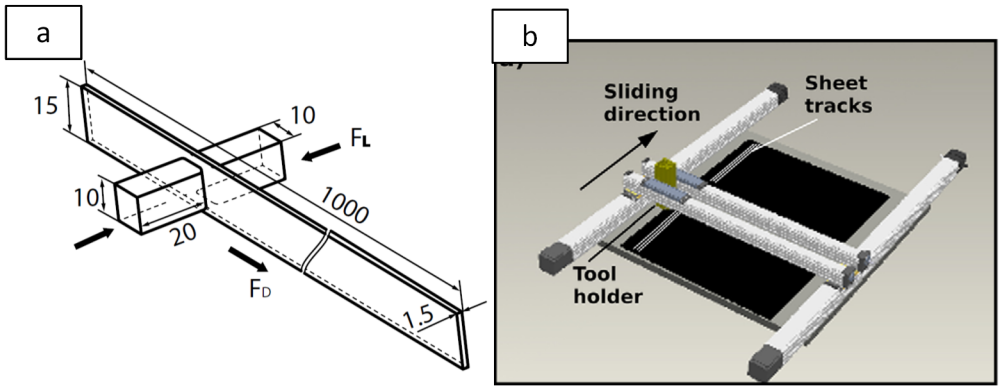

Figure 1.36: Tribometers for galling: (a) Deng's tribometer [107], (b) slider-on-flat surface (SOFS) tribometer [108].

The tribological parameters of several selected tests of metal forming are summarized in Table 1.2, including contact type, contact pressure, sliding speed, elastic/plastic contact, open/closed tribosystem, workpiece temperature and test duration time.

Table 1.2: Achievable contact conditions with the forming oriented tribometers.

Author	Contact	Pressure (MPa)	Speed ($m \cdot s^{-1}$)	Elastic/Plastic contact	open/closed tribosystem	Workpiece temperature (°C)	Test duration (s)
two-disc machine [97]	flat - flat		0.002		closed	500, 600, 800	900
optimol SRV test [97]	flat - flat	110-750	0.033-0.133	plastic	open	ambient	
Ghiotti [101]	flat - flat	5, 25	0.01, 0.1	plastic	closed	500, 800	
Upsetting-sliding [102]	cylinder - cylinder	1500	1.6	plastic	open	ambient	
Cora [105]	sphere - flat		0.33	plastic	open	ambient	
Boher [106]	cylinder -flat	20-30	4.2	plastic	open	875	20
Deng [107]	flat - flat	5,10,15	0.1	plastic	open	ambient	0.5,2,4
SOFS [108]	slider-flat		3.3	plastic	open	ambient	18

1.2.3 Developments in braking

Whereas forming or machining can be defined as processes running at respectively low or intermediate sliding velocities, the braking process appears as a special configuration as extremely high sliding speeds can be reached. As a global tribometer, the pin-on-disc configuration is widely used in reproducing the frictional behavior and thermal performance in braking process. Due to the critical contact conditions, such as high sliding velocity and contact pressure, the structural strength of the pin-on-disc configuration is necessary to be increased.

Osterle et al. [109] made use of the pin-on-disc configuration to investigate the braking of railway disks. As Fig. 1.37 shows, the test was conducted with a constant rotation speed of 900 rpm, which corresponds to a sliding velocity of 10 $m \cdot s^{-1}$, and a normal load of 230 N. The time interval was 225 s. The load is manually applied when the sliding velocity is up to 10 $m \cdot s^{-1}$. The experimental results indicate that the third body at interface plays a significant part in the frictional behavior.

Desplanques et al. [110] designed a pin-on-disc braking tribometer based on the conformity of the type of contact, the composition and microstructure of the materials, the mean contact pressure, and the sliding velocity. Fig. 1.38 shows the schematic drawing of the braking tribometer. The maximal mean contact pressure is up to 10 MPa corresponding to the normal load of 1000 N. The sliding velocity is up to 70 $m \cdot s^{-1}$. Severe high speed stop-braking conditions can be reproduced by this specially designed pin-on-disc braking tribometer [111, 62, 112].

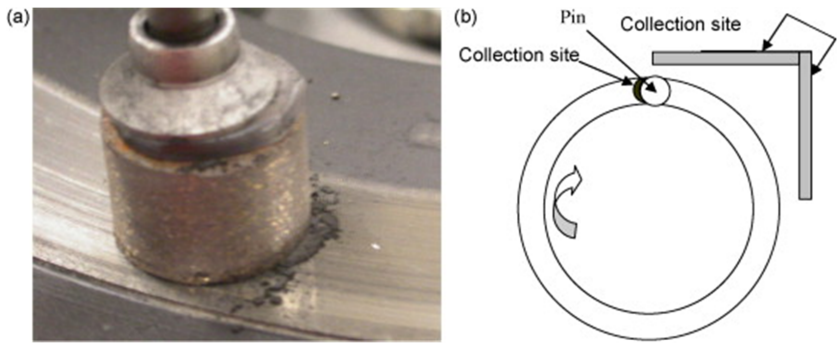

Figure 1.37: Test device: (a) photo of pin actuating against disc and (b) schematic of test [109].

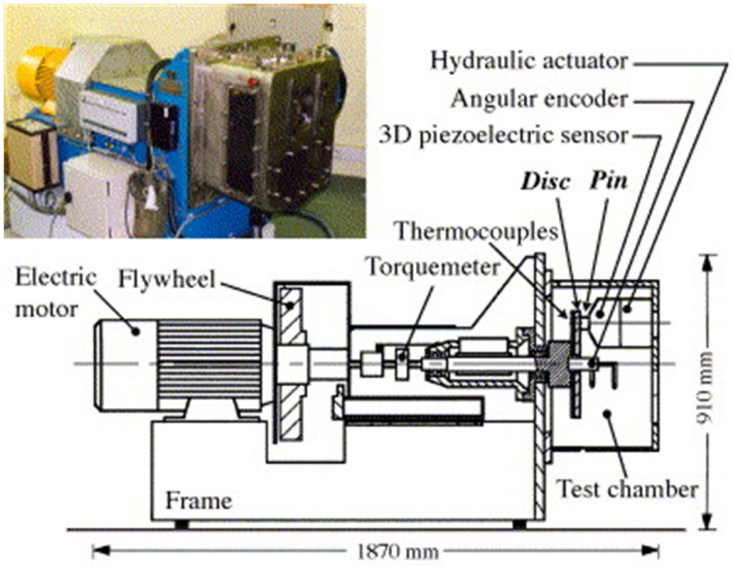

Figure 1.38: Schematic drawing of the braking tribometer by Desplanques et al [110].

Fig. 1.39 is a high speed pin-on-disc tribometer by Meresse et al. [113] specifically developed for this application and able to reach 50 $m \cdot s^{-1}$. The contact pressure is set to 0.35 MPa and 1.2 MPa corresponding to the common and emergency braking pressure. The sliding speed is 3.75, 7.5 and 15 $m \cdot s^{-1}$ corresponding the speed of car. An interesting aspect is that a pyrometer based system has been implemented to assess experimentally the contact temperature which could be over 250 °C at 15$m \cdot s^{-1}$

In short, due to the similar contact condition, the classical and updated pin-on-disc tribometers are widely used to reproduce the in-service braking conditions and thermal phenomena caused by friction in the contact. In order to ensure the accuracy of the

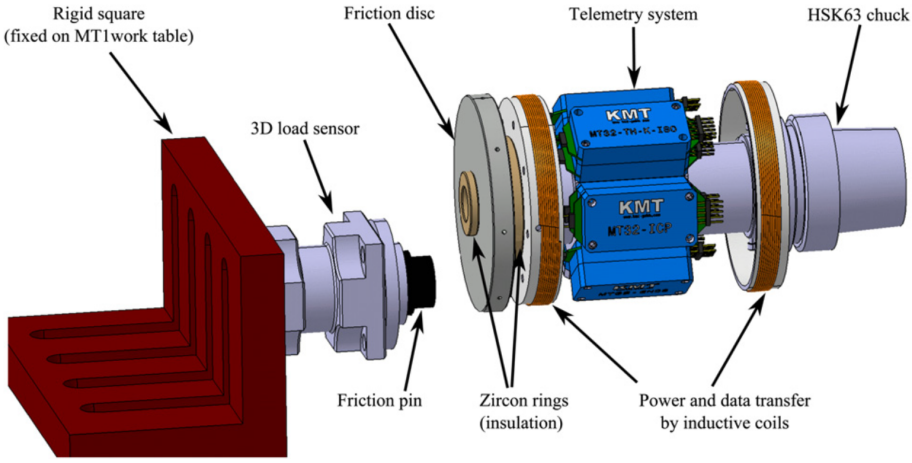

Figure 1.39: High speed braking tribometer[113].

results, the similitude rules are carried out by Desplanques et al. [110]. The dissipated kinetic energy and heat flux through the pad and disc friction areas are considered. Thus the similitude factor k is defined in Equ. 1.2 and reduced-scale experimental conditions can be determined.

$$k = \frac{E_q}{e_q} = \frac{S_\mathrm{p}}{s_\mathrm{p}} = \frac{S_\mathrm{d}}{s_\mathrm{d}} \tag{1.2}$$

Where the e_q is the dissipated kinetic energy during the test, s_d is the areas of disc friction-surface area, and the s_p is the pad friction-surface area. E_q, S_d and S_p refer to the corresponding conditions at full-scale. Fig. 1.40 indicates the difference of classical pin-on-disc contact geometry to a railway disc brake contact.

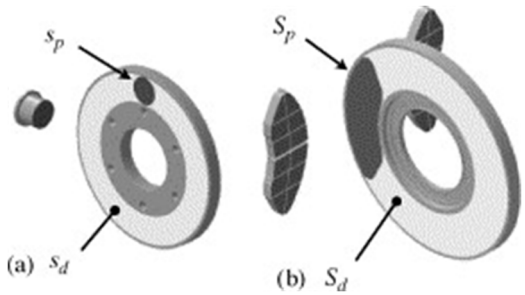

Figure 1.40: Comparison of (a) the classical pin-on-disc contact geometry to (b) a railway disc brake contact [110].

The tribological parameters of several selected tests of braking are summarized in Table 1.3, including contact type, contact pressure, load, sliding speed, elastic/plastic

contact, open/closed tribosystem, workpiece temperature, and test duration time.

Table 1.3: Achievable contact conditions with the braking oriented tribometers.

Author	Contact	Pressure (MPa)	Load (kN)	Speed ($m \cdot s^{-1}$)	Elastic/Plastic contact	open/closed tribosystem	Workpiece temperature K	Test duration (s)
Osterle [109]	pin-disk		0.5	10	plastic	closed	ambient	225
Desplanques [110]	pin-disk	10	1	70	plastic	closed	ambient	
Meresse [113]	pin-disk		10	50	plastic	closed	ambient	1800

1.3 Numerical methods to simulate severe contact conditions

Numerical simulation is becoming one of the most widely used methods to investigate different metalworking processes with various contact conditions. It is a valuable tool that can increase their understanding by providing data that cannot be assessed experimentally, dissociate the leading mechanisms by activating or not specific phenomena or perform sensitivity studies.

1.3.1 Key aspects of a numerical model

Besides some alternatives such as finite-difference method (FDM), smoothed-particle hydrodynamics (SPH), meshless method, the finite element method (FEM) remains the most commonly used and accepted approach to simulate solid mechanics issues and manufacturing processes. The present section does not intend to review the whole background of FEM and the numerous applications but rather to give a brief summary of the key aspects such as the problem formulation, thermo-mechanical coupling, material modeling, time integration, contact algorithm or adaptive remeshing.

Finite element method

The basic concept of the FEM is the discretization in the space dimensions. In order to solve a critical problem, the complicated system is subdivided into a series of simplified finite elements by the construction of meshing. The path to the solution of a finite-element problem consists of five specific steps: (a) the problem, (b) the element, (c) the element equation, (d) the assemblage of element equations, and (e) the numerical solution of the global equations [114].

Problem formulation

In general, there are three formulation methods for FEM, the Lagrangian, the Eulerian and the Arbitrary Lagrangian Eulerian (ALE) formulation. In Lagrangian formulation, the nodes are attached to the discrete particles of material. Thus the particles are represented by the nodes during the examination process. [115], the main drawback being then severe mesh distortion. Large deformations may lead for example to the Jacobian matrix turning negative at some integration points.

The Eulerian formulation differs from the Lagrangian formulation by fixing the nodes in the space and avoid the mesh distortion issues in large deformation. The Eulerian formulation is relevant to simulate efficiently a steady state deformation process [116]. However, a predefined geometry of the problem is necessary while the final configuration is often what is sought after. Eulerian formulations have been extensively used in the modeling of rolling, wire drawing, extrusion, etc. [117]. This formulation is computationally faster, and the velocity and pressure field throughout the region could be analyzed. However, it is not suitable for stresses in elastic zone analysis [118].

The ALE formulation is another method to avoid the disadvantages of Lagrangian and Eulerian formulations. In ALE formulation, the nodes can both follow the material deformations like in a Lagrangian analysis, and being fixed in space and flow through the mesh like in an Eulerian analysis [119]. Since the mesh motions are independent from the motion of the material, the high quality finite element meshes are preserved even during the numerical simulation of large deformation processes process[120]. Compared to the Lagrangian formulation with remeshing, the ALE formulation is computationally inexpensive. However, it is still difficult to define the mesh motions to preserve the mesh's high quality during the simulation, especially in 3D. Fig 1.41 presents an example of 2D simulation of the chip forming process with ALE formulation [121].

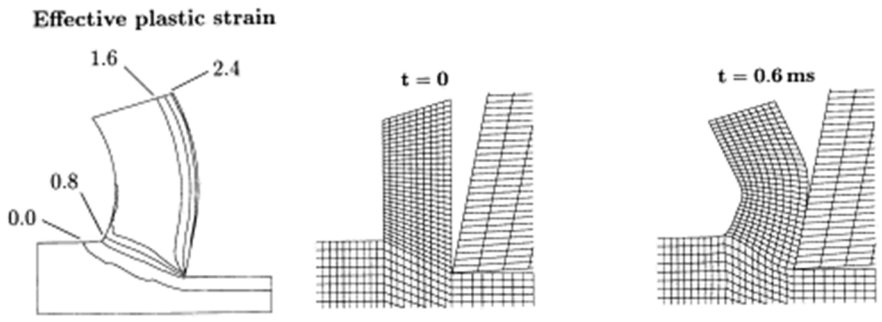

Figure 1.41: Numerical modeling of metal cutting processes using an ALE formulation [121].

In the updated Lagrangian formulation, the domain consists of a series of particles. Moreover, the configuration of the domain is updating each time increment. A linear

incremental procedure coupled with the Newton-Raphson equilibrium iterative procedure is applied for the load increment [31]. An incremental strain tensor is taken as the measure of deformation. Accordingly, the constitutive equation is expressed in terms of incremental stress, and incremental strain tensor [122]. In general, the updated Lagrangian formulation is useful in the simulation of forging process, deep drawing process, and sheet bending process, etc. [117].

Coupling

Depending on the interaction between different physical phenomena, there are two types of coupling problem, sequential coupling for weakly coupled problems, and fully-coupled analysis for strongly coupled problems [123].

As mentioned before, severe contact conditions occurring in the previously identified applications (up to several GPa, 800 °C, and 60 $m \cdot s^{-1}$ [124]) are directly connected to an intense heat generation due to the plastic deformation fricitonal dissipation. Thus taking into account the strong thermo-mechanical coupling and heat transfer between the solid in contact is necessary for an accurate numerical simulation.

Thermo-mechanical coupling method is a kind of fully-coupled analysis for strongly coupled problems, such as thermal stress, friction-driven heat transfer and temperature-displacement simulation. The heat equation considered for nonequilibrium energy is modified due to the thermo-mechanical coupling of temperature and stress. Thus, the heat generated at the interface is partially dissipated by heat transfer and partially used for the thermal expansion of the workmaterials. Therefore, the results of temperature and stress distributions of thermo-mechanical coupling is different from the uncoupled analysis [125].

Contact algorithms

The severe thermo-mechanical contact conditions at the interface have critical impacts on the numerical simulation results. The contact algorithms solve two major problems, (a) the contact detection and (b) the enforcement of the contact constrains. Regarding the contact detection strategy, the node-to-segment approach by Hallquist et al. [126] is the most common choice. Some new algorithms are presented recently, such as segment-to-segment discretization strategies based on Mortar Method [127] and contact domain method [128]. The contact constraints are then commonly applied by the Penalty approach, the Lagrangian multipliers, or the mixed penalty-lagrangian formulation [120].

Unilateral contact condition is always enforced using Signorini's conditions to limit the penetration and the apparition of tensile surface tractions between contact surfaces and the complementarity between normal stresses and the normal gap [129].

Contact properties for metalworking process

In order to estimate the heat partitioning to the two contact parts, a moving heat source theory of two semi-infinite solids in sliding contact was developed by Blok [130], and Jaeger [131]. As shown in Fig. 1.42, the heat is shared into two parts via the macroscopic heat partition ratio p, according to the Equ. 1.3. Where $\varnothing_{pin}$ is the heat flux transmitted to the pin (solid 1), $\varnothing_{workpiece}$ is the heat flux transmitted to the workpiece (solid 2). λ_{pin} and $\lambda_{workpiece}$ are the corresponding thermal conductivity of the pin (solid 1) and workpiece (solid 2), respectively. The Peclet number Pe is dependent on macroscopic sliding velocity V_{macro}, a_{pin} is the thermal diffusivity of the pin (solid 1), and b is a characteristic length of the contact. Equ. 1.3 indicates the heat partition is dependent on the velocity of the moving heat source. It should be noticed that these researches were based on a hypothesis that the interface is in a perfected sliding contact condition with the same temperature of the interacting bodies.

$$p = \frac{\varnothing_{pin}}{\varnothing_{pin} + \varnothing_{workpiece}} = \frac{\lambda_{pin}}{\lambda_{pin} + \lambda_{workpiece} \cdot \sqrt{f\left(\frac{1}{Pe}\right)}} \quad \text{with} \quad Pe = \frac{V_{macro} \cdot b}{a_{pin}} \tag{1.3}$$

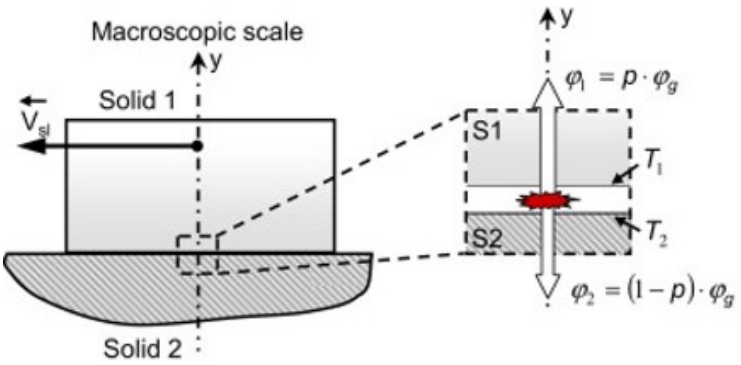

Figure 1.42: Illustration of heat partitioning in a perfect sliding contact [18].

However, at microscopic scales, the actual contact area is limited. Only a small fraction of the surfaces are actually in contact because of the roughness and imperfections of the surface, as Fig. 1.43a shows. The low thermal conductivity of interstitial media leads to the thermal constriction phenomenon [18]. Due to the modification of isotherms and flux lines, a macroscopically observed temperature jump across the interface. This resistance to heat transfer is called thermal contact resistance TCR. In a static contact, the difference of temperature T_1 and T_2 between both interacting surfaces can be expressed as a equation of the contact area Ac, the heat flux crossing the interface $\varnothing$ and the TCR, which is proposed in Equ. 1.4.

$$T_2 - T_1 = \frac{TCR}{Ac} \cdot \varnothing \tag{1.4}$$

Thus many researcher focused on the understanding and modelling of an imperfect sliding contact [132, 133, 134]. Equ. 1.5 was proposed by Bardon [132].

$$\begin{cases} \varnothing_{pin} = \alpha \cdot \varnothing + Ac \cdot \frac{T_2 - T_1}{TCR} \\ \varnothing = \varnothing_{pin} + \varnothing_{workpiece} \end{cases} \tag{1.5}$$

Where α is the heat partition coefficient, the $\varnothing_{pin}$ and $\varnothing_{workpiece}$ are the heat flux transmitted to the pin and workpiece, $\varnothing$ is the heat flux generated at interface. T_1 and T_2 are the temperature of interacting surfaces. Ac is an equation of the contact area and TCR is thermal contact resistance.

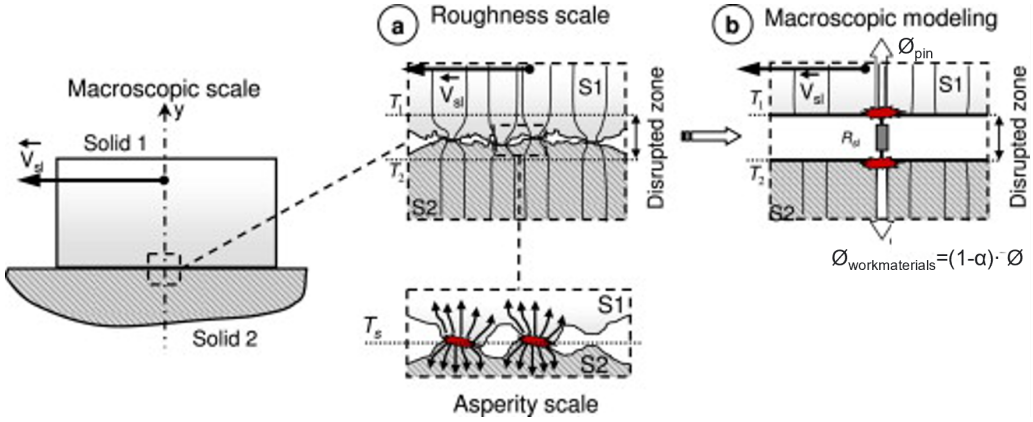

Figure 1.43: Illustration of a) An imperfect sliding contact under different scales and b) associated macroscopic thermal model [18].

It should be noted that the heat partition coefficient α in Equ. 1.5 of the heat generated by friction is essentially different from the macroscopic heat partition ratio p in Equ. 1.3. In the thesis, "heat partition coefficient" will thus refer to α.

In general, the friction coefficient at the contact interface is estimated by an experimental method such as the frictional tests and whereas only macroscopic data could be provided [135]. As Fig. 1.44 shows, the normal force F_n and tangential force F_t could be quantified by the dynamometer. Thus the macroscopic apparent friction coefficient $\mu_{app-exp}$ (experimental value) is calculated by equation 1.6.

$$\mu_{\text{app-exp}} = \frac{F_t}{F_n} \tag{1.6}$$

Bowden and Tabor [136] proposed a model which divided tangential force F_t into two parts, the plastic deformation of the workmaterials under severe contact conditions and adhesive phenomena due to the asperities contact, etc. The illustration of apparent friction coefficient divided by plastic deformation and adhesive phenomena

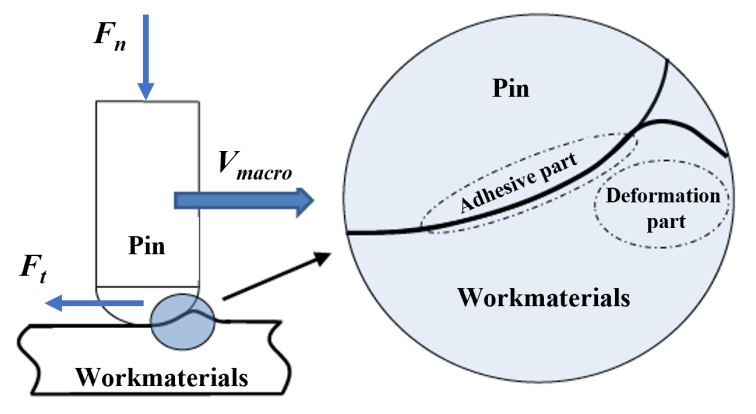

Figure 1.44: Illustration of apparent friction coefficient divided by plastic deformation and adhesive phenomena.

was presented in Fig. 1.44. Thus the apparent friction coefficient μ_{app} is presented as equation 1.7. Where the μ_{adh} is the adhesive friction coefficient, and the μ_{def} is the plastic deformation part of the apparent friction coeffcient.. However, Bowden and Tabor neglected the adhesive for the conical indenter, while the tribometer's critical deformation cannot be neglected during the scratching process.

$$\mu_{app} = \mu_{adh} + \mu_{def} \tag{1.7}$$

In order to identify the adhesive friction coefficient μ_{adh}, researchers proposed a series of mechanical contact models of the scratching process, which is shown in Table 1.4. Zemzemi et al. [137] proposed a friction model depended on contact temperature and pressure, while the contact temperature is hard to estimate unless by numerical modeling. Some researchers identified the mechanical contact models based on average local sliding velocity [11, 138, 139, 7].

For example, Ben Abdelali et al. [7] proposed a friction model by using a numerical model to identify the apparent adhesive friction coefficient μ_{app}. They assumed that the adhesive fricion coefficient μ_{adh} is constant over the surface at a specific macroscopic sliding velocity V_{macro}. The procedure starts by introducing a theoretical adhesive friction coefficient in the model. Then, the model provides the numerical apparent friction coefficient, $\mu_{app-num}$. As Fig. 1.45 shows, the model provided a numerical apparent friction coefficient $\mu_{app-num}$ by introducing a theoretical adhesive friction coefficient μ_{adh}. The adhesive friction coefficient was presented by interpolation when the deviation between theoretical ($\mu_{app-num}$) and experimental ($\mu_{app-exp}$) macroscopic friction coefficient was less than 1%.

Nevertheless, these researchers considered the impact of sliding velocity on the

Table 1.4: Mechanical contact models

Author	Year	Workmaterials & tools	Local sliding velocity V_{ls} ($m \cdot s^{-1}$)	Sliding velocity V_{macro} ($m \cdot s^{-1}$)	Friction model
Zemzemi [137]	2007	AISI4142 TiN coated carbide		0.4-3.3	$\mu_{adh} = 0.16 (T > 746°C)$ $\mu_{adh} = 5.56 \times 10^{7} T^{-3.3008} P^{0.285} - 0.018 (545 < T < 746°C)$ $\mu_{adh} = 0.5 (T < 545°C)$
Zemzemi [11]	2009	AISI4142 TiN coated carbide	0.03-2.83	1-3.33	$\mu_{adh} = -0.07 ln(V_{ls}) + 0.570$
Rech [138]	2009	AISI1045 TiN coated carbide	0.83-1.72	1.25-2.5	$\mu_{adh} = -0.002 V_{ls} + 0.498$
Courbon [139]	2011	AISI1045 TiN coated carbide		1.0-5.0	$\mu_{adh} = 0.162 + 0.368 e^{-0.746 V_{ls}}$
Ben Abdelali [7]	2011	AISI1045 TiN coated carbide		0.083-5.0	$\mu_{adh} = -0.002 (V_{ls})^4 + 0.024 (V_{ls})^3 - 0.042 (V_{ls})^2 - 0.117 (V_{ls}) + 0.484$
Rech [140]	2013	AISI1304L TiN coated carbide		0.4-3.3	$\mu_{adh} = 3.91 (V_{ls})^{-0.559}$

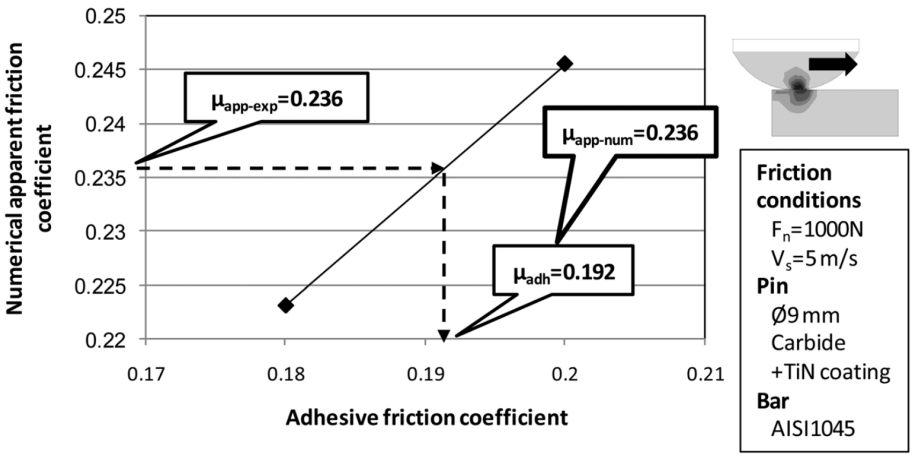

Figure 1.45: Determination of adhesive friction coefficient Ben Abdelali et al [7].

friction coefficient. The introduced theoretical adhesive friction coefficient is still a constant value at a single macroscopic sliding velocity V_{macro}. Moreover, the average local sliding velocity is difficult to be estimated as well.

1.3.2 Examples of applications in metalworking processes

This section focus on the numerical modeling of "pure" sliding contact.

Bonnet et al. [10] presented a is a 3D ALE model of a unidirectional sliding test in Fig 1.46. The objective was to identify the friction properties at the tool/chip/workpiece interface focusing the analysis on the phenomena occurring at the pin/workpiece interface. One can see that contact pressures up to 2.7 GPa and contact temperature around 1460 °C at the tool-workpiece interface could be reached when sliding WC/Co carbide against AISI 316L workmaterial at 2 $m \cdot s^{-1}$. The minimal mesh size of the pin and workpiece is 5 and 10 μm, respectively.

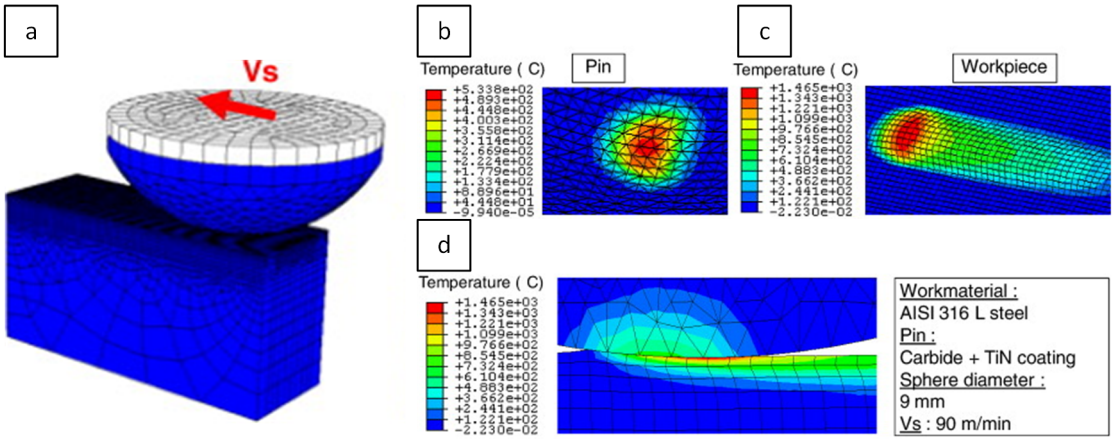

Figure 1.46: (a) 3D scratching model, temperature distribution of (b) pin, (c) workpiece, and (d) assembly [10].

Ben Abdelali et al. [7] used a 3D ALE model (Fig. 1.47) to numerically estimate the local sliding velocity, contact pressure, and temperature at the interface during the dry sliding of AISI1045 steel with TiN coated carbide pin. They also used this model as an inverse methodology to identify a friction model and a heat partition model based on sliding velocity by comparison of the simulated values with the experimental data provided by the Claudin's tribometer [84] in Fig. 1.28. Due to the limitation of ALE formulation, the 3D ALE model only simulated several milliseconds of the actual scratching process. It is too hard for the model to reach the thermal equilibrium conditions. Thus the 3D temperature distribution of the 3D ALE model should be questioned.

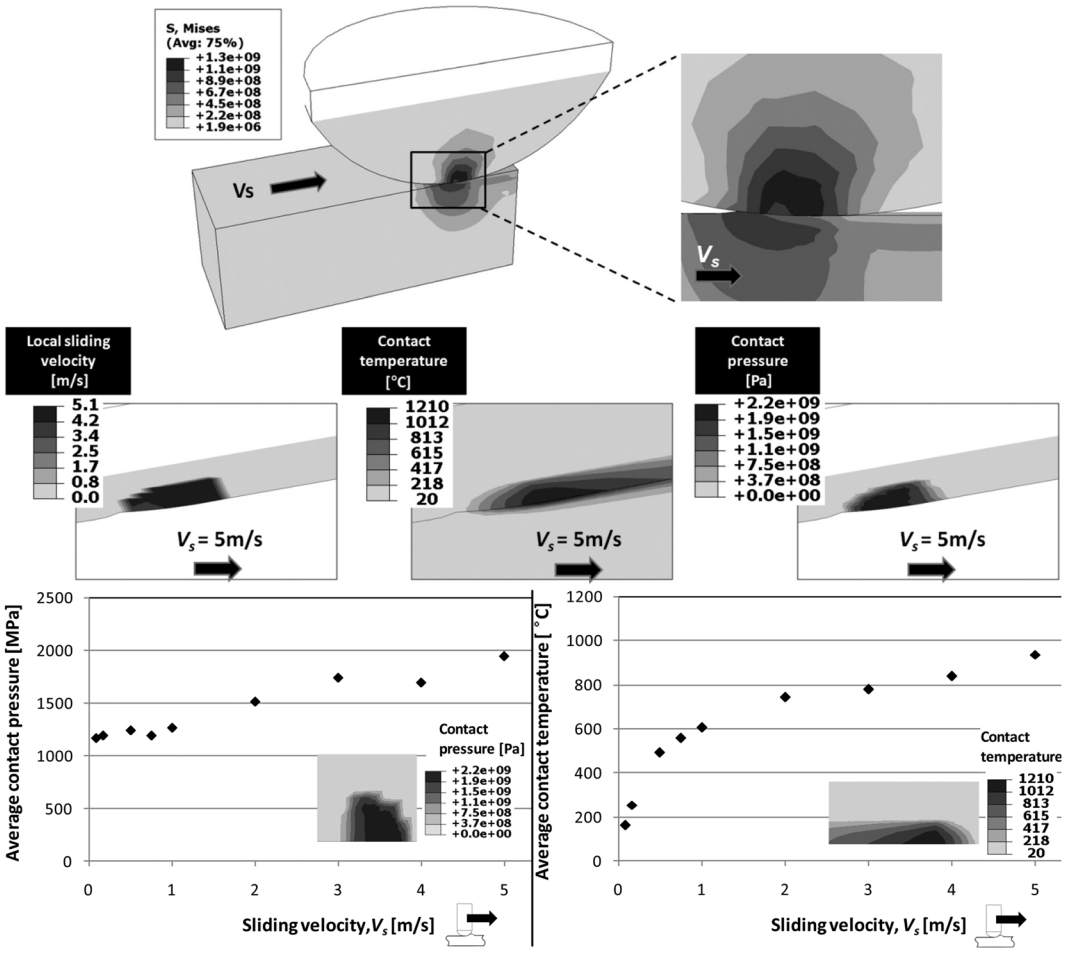

Figure 1.47: 3D scratching model by Ben Abdelali [7].

Brocial et al. [102] employed a numerical model of the upsetting-sliding test to extract the contact conditions such as the contact pressure, the interfacial temperature, the sliding velocity for the dry machining of AISI 1045 steels. As Fig. 1.48 shows, the maximum contact pressure located in front of the contact is around 1.5 GPa. The maximum temperature is 1185 K. The average of temperatures in the contact zone reaches 925 K for the specimen.

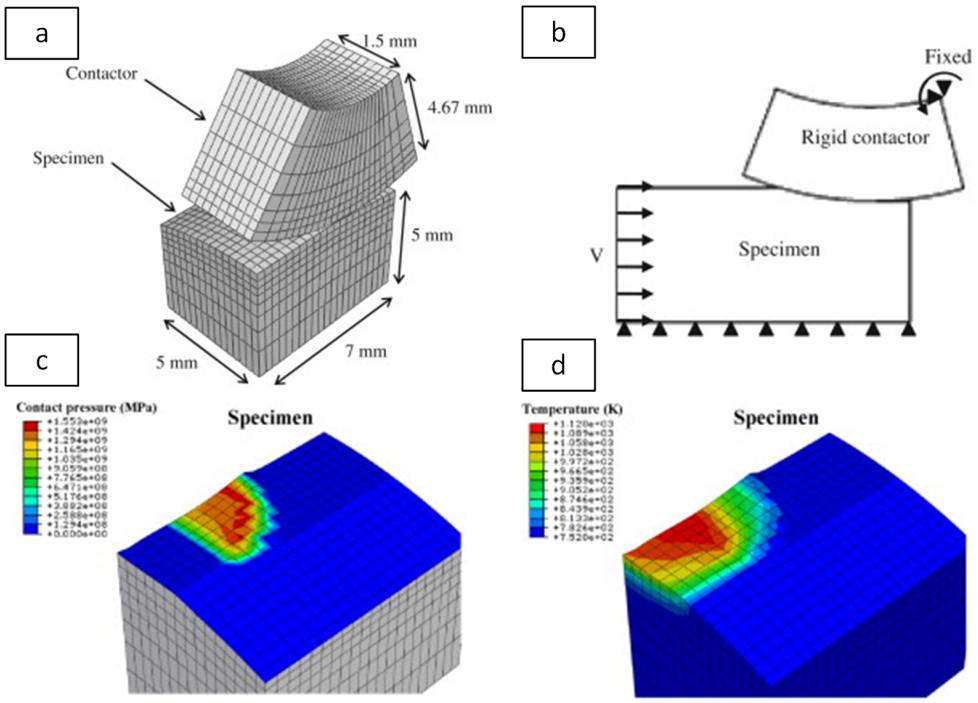

Figure 1.48: Numerical modeling of the upsetting-sliding test: (a) principle of the model, (b) boundary condition, (c) contact pressure and (d) temperature distribution [102].

Akbari et al.[141] simulated linear machining experiments effectuated by single diamond grains using thermo-mechanical dynamic analysis by commercial code MSC Software. The boundary conditions is shown in Fig. 1.49a. The simulation results show the influence of two different cutting edge radii of 0 and 20 μm for cutting speed of 0.8 $\mathrm{m \cdot s^{-1}}$ and 30 μm depth of cut. The flash temperature with 0 μm cutting edge is around 754 K, while the flash temperature is up to 806K with 20 μm cutting edge.

In addition, Smoothed Particle Hydrodynamics (SPH) method [142] and meshfree method [143] can be employed to identify the sliding contact in the machining process.

Among these "pure" sliding numerical models, the researchers are trying to obtain some local data that they cannot access experimentally, such as local contact temperature, pressure, and stress distribution. In addition, friction/heat partition model could be identified using a post-processing tool to identify friction/heat partition models [10, 144, 102, 141];

However, there are still some limitations. The thermal contact conditions at the interface are not clearly identified, e.g., the thermal contact conductance is estimated value; The real simulation time is often too short to reach thermal balance conditions, thus the simulated temperature distribution should be reconsidered. The Coulomb

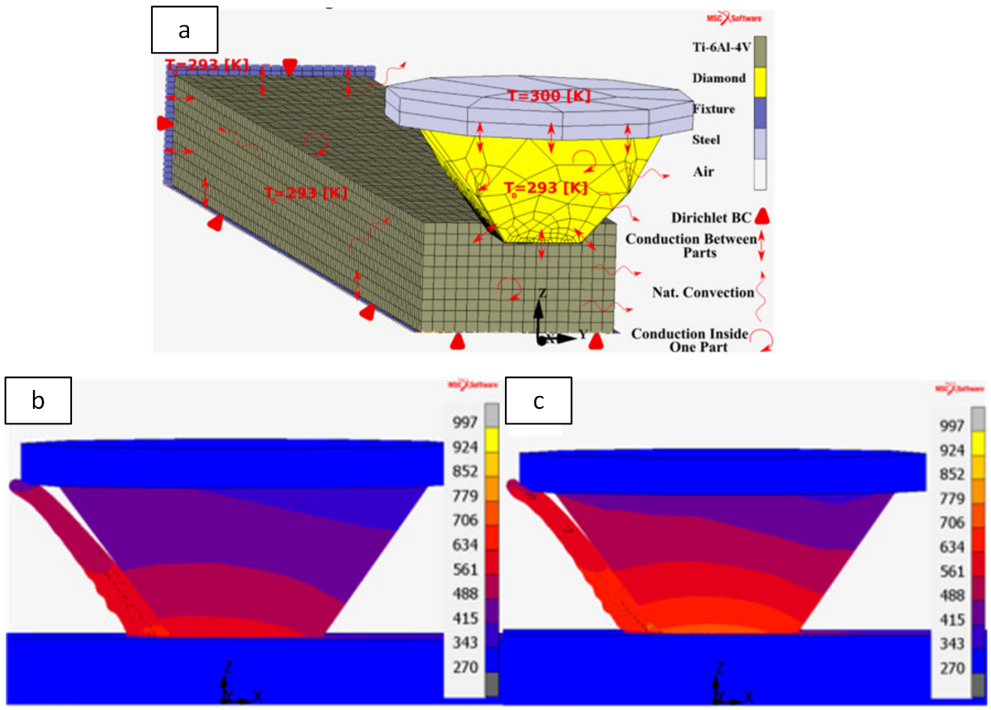

Figure 1.49: Liner machining model: (a) boundary condition, temperature distribution with cutting edge radii of (a) 0 and (b) 20 μs [141].

friction model is the most widely used friction law, while the Coulomb friction model could not reflect the critical deformation at severe contact conditions. [10, 144, 102, 141, 142, 143]

1.4 Summary and identified knowledge gap

In this chapter, the basics of tribology under severe contact conditions have been discussed. The experimental and numerical approaches to investigate the tribological characteristics have been summarized. It is clear that the experimental approaches are the essential methods to not only study the frictional behavior at the interface but also supply reliable input data for the numerical simulation. However, for all the listed processes, it is not easy to monitor the local conditions at the contact interface only with the experimental methods. Therefore, numerical approach is highly required to investigate thoroughly these local aspects. However, there are always many assumptions to simplify the numerical model:

- Impact of the meshing on the local data;

- The thermal contact conditions at interface are not clearly defined;
- The full 3D geometry of the solids is not always properly considered;
- The friction coefficient is always assumed to be constant for a given macroscopic sliding velocity whereas they intend to identify varying friction models based on local contact conditions;
- Only the macroscopic data are imported whereas the local contact parameters are varying based on the local contact conditions.

As a consequence, the reliability and accuracy of the estimated numerical results are still questionable. Therefore, when it comes to identifying contact models based on a numerical approach, it appears as a strong limitation whereas it is a key input data when modelling all the listed applications. Considering the important thermo-mechanical coupling reported in the previous sections, thermal aspects are especially considered whereas they are clearly the weakest ones. Many research works claim that friction or wear model must be temperature dependent, i.e. depend on the "contact temperature". However, the "contact temperature" appears highly difficult to assess experimentally, the widely accepted definition of "contact temperature" is still uncertain.

Finally, the few iterative methods proposed in the literature to post-process experimental data with a numerical model are still not used to their actual potential. There is a clear need of alternatives not to run simulations in a sequential way, but rather to perform large scale sensitivity analyses combined to advanced identification methods.

2 Finite element model of the scratching process

Summary

Objective of this chapter

This chapter aims to develop a numerical modeling strategy to estimate the local contact parameters at the tool-material interface during a pin-on-bar frictional test under severe contact conditions. A cemented carbide pin sliding against a medium carbon steel C45 is considered in this work. In general, severe contact conditions lead to high strain and strain rate, which easy to cause a model not to converge. In order to avoid computation issues, a first thermally-coupled scratching model is developed under an explicit framework. The latter limits the simulations to a few milliseconds of the real scratching process, making it impossible for the thermal balance to be reached. An implicit heat transfer model is thus established based on the heat flux distribution imported from the explicit scratch model and relevant 3D boundary conditions. The implicit model can simulate the scratch process until the system reaches the steady-state thermal conditions and give an insight into the temperature reached in the contact zone.

2.1 State of the art

The tribometer @ENISE shown in Fig 2.1 is designed by F. Zemzemi et al.[11] and Claudin et al. [84]. It could measure the friction coefficient under extreme contact pressure and very low sliding velocities and apply a cutting fluid under defined conditions (pressure, orientation, flow rate, temperature, etc.). Based on this open tribometer, a series of friction and wear experiments were presented to simulate contact conditions encountered in cutting on a longer time scale, such as the effects of straight oil friction at the tool-workmaterial interface [84], the friction and heat partition coefficients evolution for different tool-workmaterial pairs and lubrication conditions (dry, emulsion, straight oil, and cryogenic) [140].

Ben Abdelali et al. [144] identified the workpiece surface temperature and an equivalent plastic strain at this interface during the dry cutting of an AISI 1045 with TiN–coated carbide tools, etc. Despite the average temperature, contact pressure, sliding velocity, heat partition, and friction coefficient at the tool-workmaterial interface in the macroscopic scale could be estimated. It is hard to monitor the local parameters at the interface. Some researchers attempted to use, for example, an infrared camera to record temperature versus time [145]. However, the spatial resolution compared with a large temperature gradient at the interface makes the quantification critical. In order to get rid of the limitations of the experimental methods, numerical simulation appears as a relevant alternative to investigate the thermal contact conditions [11, 7, 19] in such confined and strongly coupled tribosystems where temperature governs friction, wear mechanisms, and near-surface modifications.

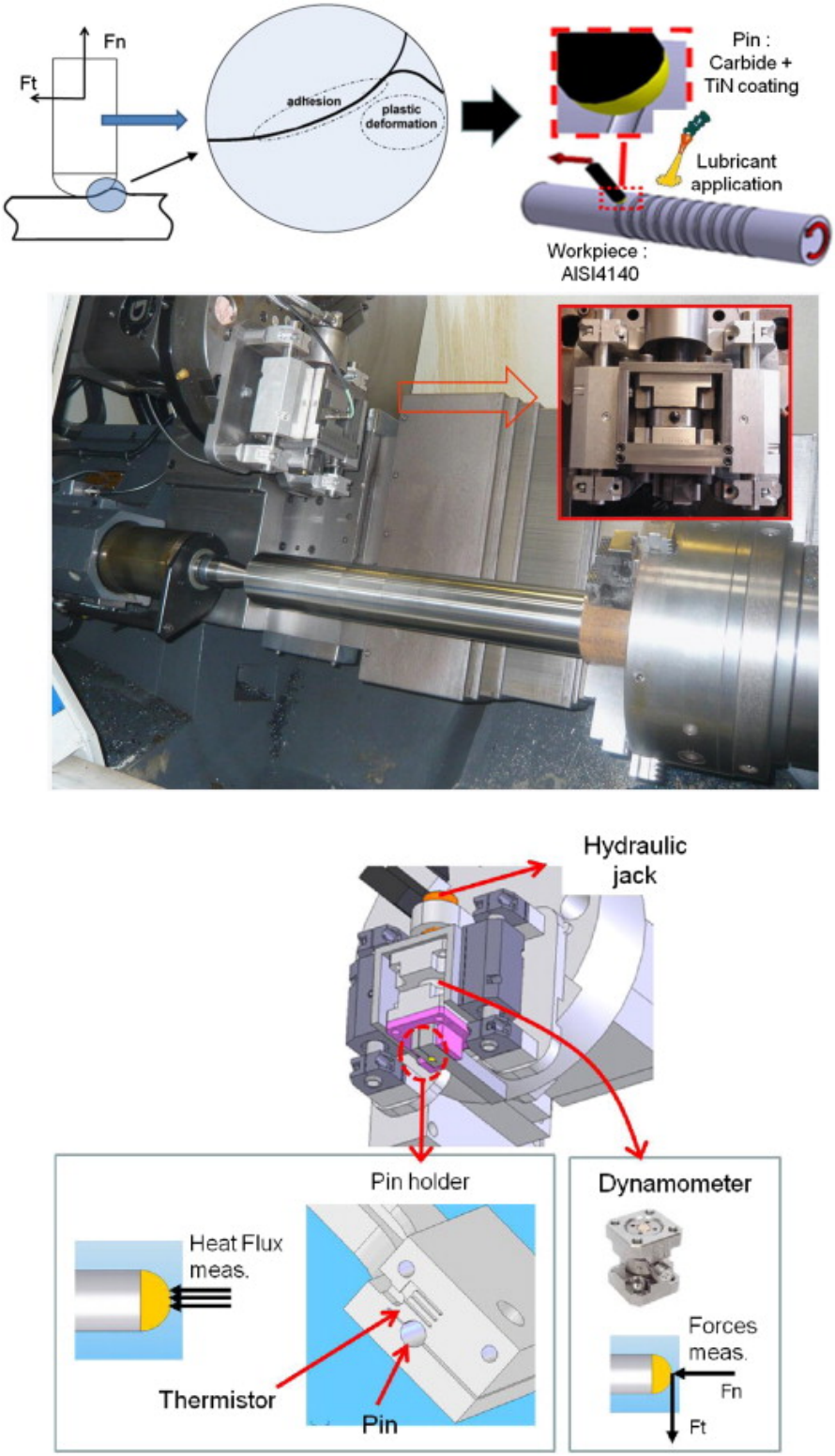

Figure 2.1: Design of the tribometer developed [84].

2.2 Choice of formulation

2.2.1 Explicit scratch model

First of all, it is necessary to choose the formulation method between explicit integration and implicit integration for the FE model. Explicit integration methods calculate the state of the system at a later time from the state of the system at the current time without the need to solve algebraic equations. In contrast, implicit integration methods find a solution by solving an equation involving the current state of the system and the later one [146]. The explicit integration method is typically used to solve transient problems with small time steps, especially with a high deformation rate and severe contact conditions. Due to the high strain rate of the scratch process, explicit integration methods are chosen for the FE model.

Furthermore, one method must be selected between the Lagrangian, the Eulerian, and the ALE formulation. The Lagrangian methods' main drawbacks are mesh distortion, and entanglement of finite elements in problems with relatively large deformations [147]. For Eulerian formulation, the large strains will not cause numerical problems, while the geometry must be known for the beginning. It is not acceptable for the dynamic scratching process. The ALE method was first developed in fluid mechanics for modeling the motion of free surfaces and boundary conditions [147]. The ALE method combines the advantages of Lagrangian and Eulerian formulation. The large strains and mesh distortion can be prevented by decoupling the mesh displacements and the material displacements. The first numerical development is a 3D model of the full pin-on-bar test based on the Arbitrary Lagrangian-Eulerian (ALE) explicit approach.

2.2.2 Implicit heat transfer model

The only drawback is that the ALE explicit model can only simulate some milliseconds of the real scratch process, and it is too difficult to reach the thermal balance conditions. The only choice for the second model is the implicit approach. In the implicit method, general equilibrium is achieved by iteration first, followed by evaluating local element variables. If the balance is not achieved, this method becomes expensive for calculation since the matrix coefficients should recalculate with different time steps. The implicit method is unconditionally stable, allowing the use of more massive increment time steps. It is suitable for problems that tend to be highly linear, static, and quasi-static.[148].

Based on the surface heat flux distribution imported from the explicit simulation results, the interface temperature distribution could be estimated by an implicit heat transfer model without mesh distortion. For the implicit heat transfer model, the Lagrangian formulation is an appropriate choice.

2.3 Development of ALE explicit scratch model

Based on the previous study, the commercial code SIMULIA Abaqus FEA was employed to simulate the local contact parameters at the tool-workmaterials interface. Considering the cutting process with high thermal-mechanical complexity, such as high strain rate, high contact temperature gradient, the finite element method (FEM) is selected to estimate the quantitative prediction of the thermal and mechanical parameters generated in the interface.

2.3.1 Description of the model

The model considers a static pin and a moving workpiece. Considering the symmetry of the pin-workpiece system, only half of the system is modeled. As Fig. 2.2 shows, the pin is modeled as part of the sphere of 9 mm. Its height is 0.5 mm. Hexahedral C3D8T elements were selected to enable a proper heat transfer modeling. Mesh size is approximately 60 µm around the contact surface. A concentrated normal force F_n is applied to the reference point associated with a rigid pin surface to simulate the load on the pin. The thermophysical properties of WC tungsten carbide are imported from I. M. Arrieta [149], which is shown in Table 2.1.

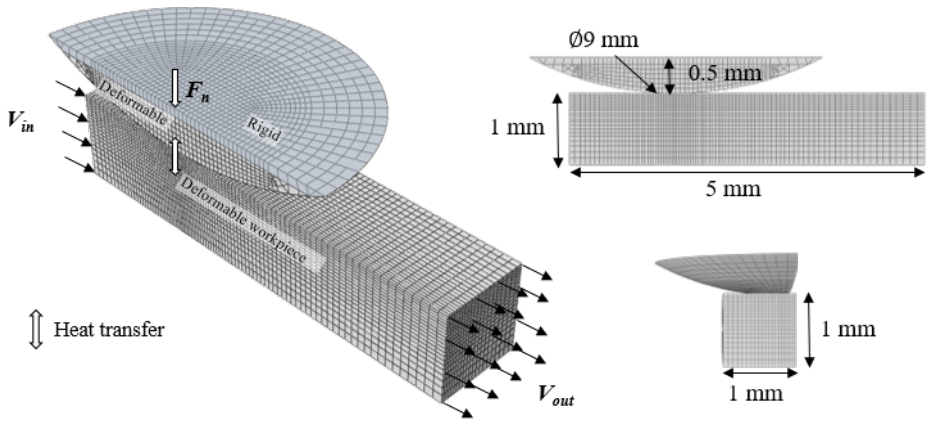

Figure 2.2: Description of the updated ALE explicit model.

Regarding the workpiece, hexahedral C3D8RT elements with reduced integration were selected to simulate the thermal mechanic coupled scratching process. The element size is close to 20 µm around the contact zone and gradually increasing to 100 µm at the edge of the workpiece. Eulerian surfaces were defined at the two sides of the workpiece. The materials enter with a velocity V_{in} by the Eulerian surface and exits through the Eulerian surface with a velocity V_{out}, where $V_{in} = V_{out}$. For the C45 thermal-mechanical

Table 2.1: Properties of the tungsten carbide H13A [149].

Temperature [K]	Density [kg·m^{-3}]	Specific heat [J·kg^{-1}·K^{-1}]	Thermal conductivity [W·m^{-1}·K^{-1}]	Young's modulus [GPa]	Poisson's ratio
293	14968	113	202		
373	14964	98	202		
473	14946	83	208		
573	14914	72	208		
673	14885	62	205	630	0.3
773	14855	60	195		
873	14827	47	167		
973	14799	29	105		

behavior, due to the strong deformation during the scratch process [150], a Johnson-Cook flow stress model identified by Jaspers and Dautzenberg [151] has been used to model, as shown in equation 2.1 with the constants given in Tab. 2.2.AISI 1045 steel's thermophysical properties are those identified by I. M. Arrieta [149] in Table 2.3.

$$\sigma = \left[A + B \cdot (\varepsilon_p)^n\right] \cdot \left[1 + C \cdot \ln\left(\frac{\dot{\varepsilon}_p}{\dot{\varepsilon_0}}\right)\right] \cdot \left[1 - \left(\frac{T - T_0}{T_M - T_0}\right)^m\right] \tag{2.1}$$

where σ is equivalent plastic stress, A is the yield strength (MPa), B is the hardening modulus (MPa), ε_p is the equivalent plastic strain, n is the hardening coefficient, C is the strain rate sensitivity coefficient (viscosity), $\dot{\varepsilon}_p$ is the plastic strain rate, $\dot{\varepsilon_0}$ is the reference plastic strain rate, which equals 1.0 s^{-1} in this chapter, T is absolute temperature, T_0 is room temperature, and T_M the melting point of the specific alloy, m is the thermal softening coefficient.

Table 2.2: Constant for the Johnson-Cook constitutive models of the C45 [151].

A [MPa]	B [MPa]	C	n	m	T_M [K]	T_0 [K]	$\dot{\varepsilon_0}$ [s^{-1}]
553	601	0.013	0.23	1	1733	293	1

Table 2.3: Properties of the C45 steel [149].

Temperature [K]	Density [kg·m^{-3}]	Specific heat [J·kg^{-1}·K^{-1}]	Thermal conductivity [W·m^{-1}·K^{-1}]	Young's modulus [GPa]	Poisson's ratio
294	7764	396	32		
397	7753	459	36		
497	7724	519	37		
597	7684	545	34		
697	7646	595	33	207	0.3
797	7608	664	28		
897	7570	633	23		
997	7533	803	21		
1097	7553	323	10		

2.3.2 Boundary conditions

For the explicit scratch model's thermal boundary conditions, as Fig. 2.3 shows, heat transfer by conduction at the pin-workpiece interface is considered. Heat is dissipated by conduction through surfaces ABB'A', CDD'C', A'B'C'D', AA'D'D and BB'C'C. Heat exchange through the surface ABCD is neglected.

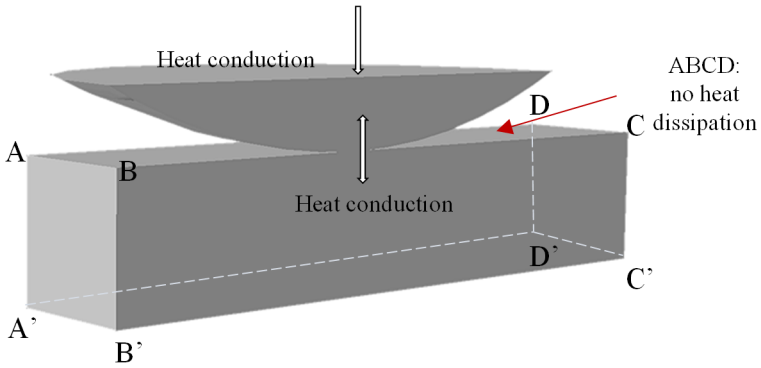

Figure 2.3: Node temperature distribution of (a) assembly and (b) pin in the explicit model.

The friction coefficient between the pin and the workpiece is defined by equation 2.2 [140]. Where μ_{adh} is the adhesive friction coefficient at a specific macroscopic sliding velocity V_{macro} (m·s^{-1}).

$$\mu_{adh} = 3.75\,(60 \cdot V_{macro})^{-0.538} \tag{2.2}$$

For the numerical model, the heat partition coefficient α between the pin and the workpiece could be estimated by equation 2.3 [140] at a specific macroscopic sliding velocity V_{macro} ($m \cdot s^{-1}$).

$$\alpha = 1.27\,(60 \cdot V_{macro})^{-0.458} \tag{2.3}$$

2.4 Numerical results of the explicit scratch model

The explicit scratch model identifies the local contact conditions, including the heat flux distribution on the pin's spherical tip. In order to simulate the severe contact conditions at the interface, the normal force F_n applied to the center of the pin is 500N, and the macroscopic sliding velocity V_{macro} is selected from 2 $m \cdot s^{-1}$ to 5 $m \cdot s^{-1}$. The TCR is assumed as 100 $K \cdot mm^2 \cdot W^{-1}$ based on previous findings from Bourouga et al. [23]. The friction coefficient and the heat partition coefficient between the pin and workpiece were defined by equation 2.2 and equation 2.3.

2.4.1 Heat flux distribution

The manufacturing process always leads to high contact temperatures in the tool and workpiece's contact area and increases the importance of thermal factors. Besides amplified thermal tool loading, the thermal fluxes affect the accuracy due to thermo-elastic deformations. Thus it is essential to know the magnitudes of these heat flows in order to assess the heat conduction and stability [152].

Fig. 2.4 presented the heat flux multiplied by the nodal area (HFLA) at the pin interface after 10 ms of numerical simulation. The max heat flux multiplied node area is 910 mW (absolute value). The negative value means the direction of heat flux is toward the pin. It indicates that the sliding velocity has contributed to the heat flux distribution. These results are similar to those reported by Claudin et al. [84].

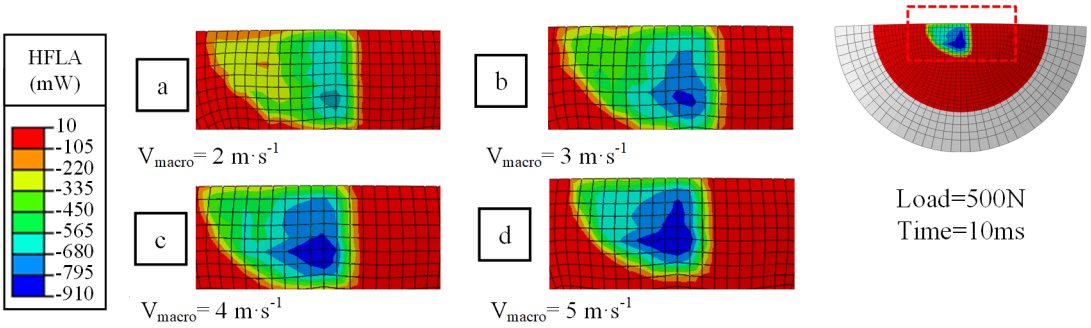

Figure 2.4: Heat flux multiplied node area of the pin at 10 ms with different sliding velocities(a) 2 $m \cdot s^{-1}$, (b) 3 $m \cdot s^{-1}$, (c) 4 $m \cdot s^{-1}$, and (d) 5 $m \cdot s^{-1}$.

The total power which penetrates the interface of the pin and heating the materials could be calculated based on the HFLA distribution (Fig. 2.4a). The evolution of the total heat input is plotted in Fig. 2.5a & b. It indicates that the heating power tends to stabilize after 4 ms of the scratching process. It also shows that the heat flux is affected by sliding velocity. The heat flux is likely to increase then tends to leave off. These results are similar to those reported by Rech et al. [140].

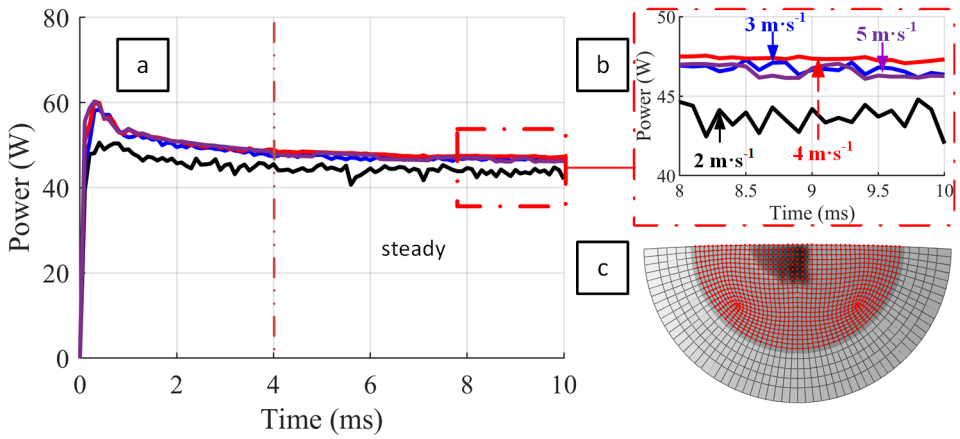

Figure 2.5: Heat flux multiplied by the nodal area distribution under different sliding velocities (a), partial enlarged detail (b), and the corresponding location of selected area (c).

2.4.2 Contact pressure distribution

Like the heat flux distribution, the contact pressure distribution is one of the critical parameters that significantly influences wear and damage of the cutting tools and impacts surface integrity.

Fig. 2.6 shows the contact pressure distribution at the pin interface after 10 ms of numerical simulation. The max contact pressure is around 2.49 GPa. It is clear that a higher sliding velocity leads to more critical contact conditions. The severe contact conditions at the interface tends to increase the contact pressure.

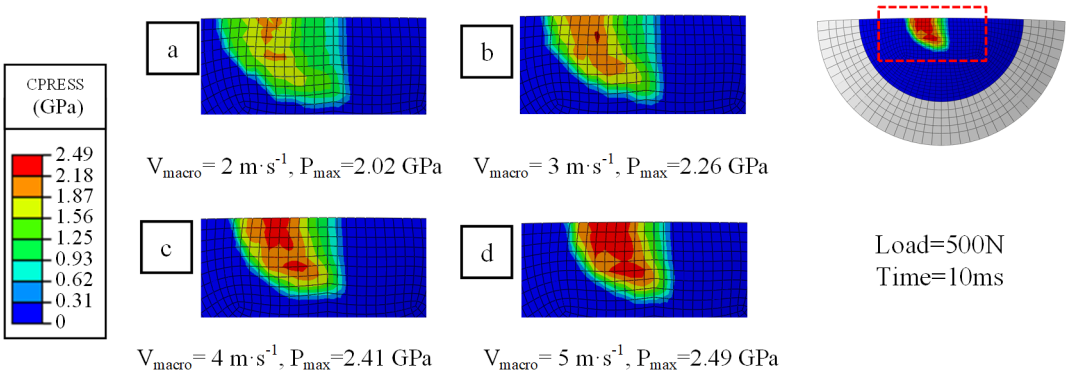

Figure 2.6: Contact pressure distribution of the pin at 10 ms with different sliding velocities(a) 2 $m \cdot s^{-1}$, (b) 3 $m \cdot s^{-1}$, (c) 4 $m \cdot s^{-1}$, and (d) 5 $m \cdot s^{-1}$.

2.4.3 Local sliding velocity distribution

Furthermore, the local sliding velocity V_{ls} distribution is studied in this part. Fig 2.7 presents the local sliding velocity V_{ls} distribution at the workpiece contact area with different macroscopic sliding velocities V_{macro}. The max local sliding velocity V_{ls} is a little bit higher than the macroscopic sliding velocity V_{macro}. This due to the distance around the sphere is higher than the straight line. So it is necessary to be faster in some areas.

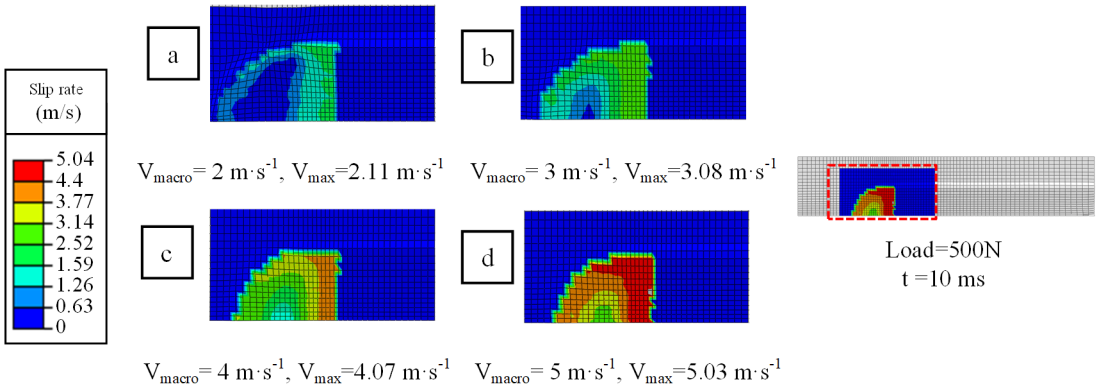

Figure 2.7: Local sliding velocity V_{ls} distribution at the workpiece contact area with different macroscopic sliding velocities $V_{m}acro\ V_{macro}$ (a) 2 $m \cdot s^{-1}$, (b) 3 $m \cdot s^{-1}$, (c) 4 $m \cdot s^{-1}$, and (d) 5 $m \cdot s^{-1}$.

2.4.4 Numerical apparent friction coefficient

In addition, the numerical apparent friction coefficient $\mu_{app-num}$ at the workpiece contact area with different macroscopic sliding velocities V_{macro} is presented in Fig. 2.8. It indicates that higher sliding velocity leads to smaller and more stable numerical apparent friction coefficient $\mu_{app-num}$.

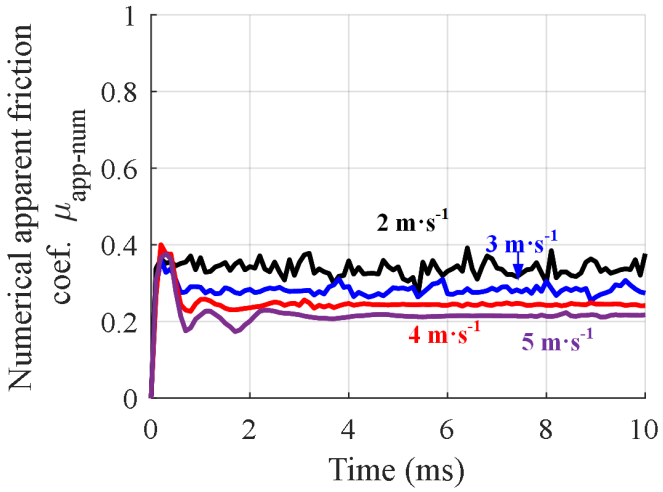

Figure 2.8: Numerical apparent friction coefficient at the workpiece contact area with different macroscopic sliding velocities V_{macro}.

2.5 Development of the implicit heat transfer model

The quantitative prediction of local contact parameters is estimated with the ALE explicit scratching model in section 2.4. As mentioned before, the only drawback is that the ALE explicit model can only simulate some milliseconds of the real scratch process, and it is too difficult to reach the thermal balance conditions. As Fig 2.9 shows, the node temperature of selected nodes on the pin is continuously increasing after 10 ms of simulation of scratching process. The macroscopic sliding velocity V_{macro} is 3 $m \cdot s^{-1}$ and the normal force F_n is 500 N. The contact temperature distribution at thermal balance conditions is still uncertain. Therefore, this section aims to develop another FE model to estimate the interface temperature distribution on the pin's spherical tip.

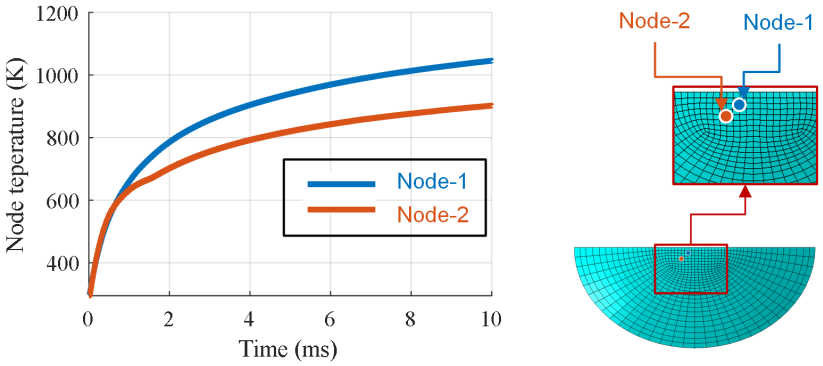

Figure 2.9: (a) Selected node temperature of pin versus time, and (b) corresponding area of selected nodes.

2.5.1 Description of the implicit model

The second numerical model is an implicit heat transfer model considering only the friction pin and the corresponding pin holder (Fig. 2.10).

The model consists of two parts with the pin (Fig. 2.10b) mounted into the pin holder (Fig. 2.10c). Hexahedral DC3D8 elements were applied for the heat transfer procedure. The pin consists of three subparts, two spherical tips directly imported as orphan meshes and mirrored from the explicit scratching model, which are then combined to the cylindrical core of the friction pin. The advantage of the orphan mesh is that it is convenient to import the explicit model's heat flux distribution and apply the heat flux distribution on the pin tip. It is not necessary to consider the geometry and mesh on the tip of the pin. Similar to the explicit model, the pin is made of WC tungsten carbide (Table 2.1), and the mesh size is approximately 60 µm around the contact surface. For the pin holder, the element size is approximately 1 mm, and the

thermophysical properties of C45 steel (Table 2.3) were applied.

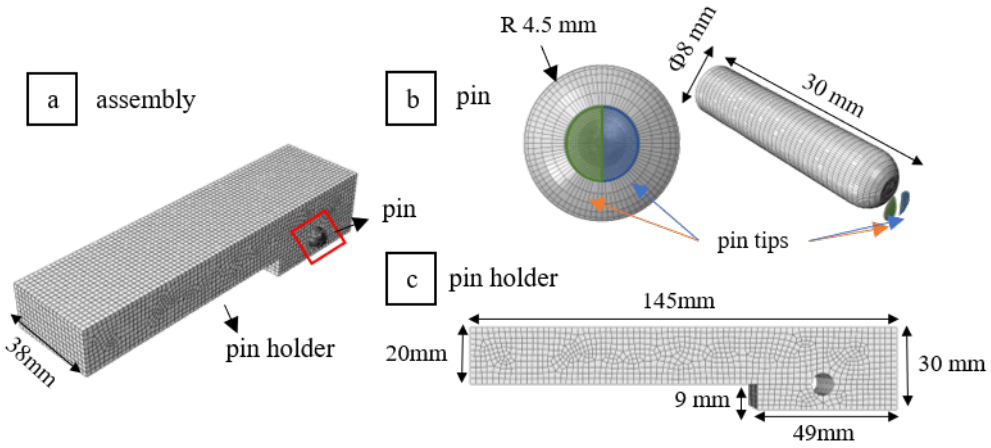

Figure 2.10: Description of the heat transfer implicit model (a) assembly, (b) pin and (c) pin holder.

2.5.2 Boundary conditions

Regarding the thermal boundary conditions, some were considered to be of interest. As Fig. 2.1, the pin holder is fixed in the tribometer. Therefore the heat conduction between the pin holder and the tribometer should be considered. The relative surfaces is shown in Fig. 2.11a. Similarly, the heat conduction between the pin and pin holder is considered as well (Fig. 2.11b). Furthermore, the heat exchange with the environment by convection and radiation is considered (Fig. 2.11c).

To sum up, the boundary conditions of the implicit heat transfer model is considered as follows:

- Convective heat transfer to surroundings (Fig. 2.11a);
- Radiation heat transfer to surroundings (Fig. 2.11b);
- TCR between pin & pin holder (Fig. 2.11c);
- TCR between pin holder & tribometer (Fig. 2.11d)

The steady-state heat flux distribution, which is shown in Fig. 2.4a, is imported from the numerical results of the explicit scratch model and applied as boundary conditions in the 3D thermal model. The heat transfer by convection is assumed to $50\,\mathrm{W\cdot m^{-2}\cdot K^{-1}}$. The emissivity coefficient of the carbide pin is assumed at 0.82 since Kieruj et al. [153]. Thermal contact resistance between pin & pin holder and between

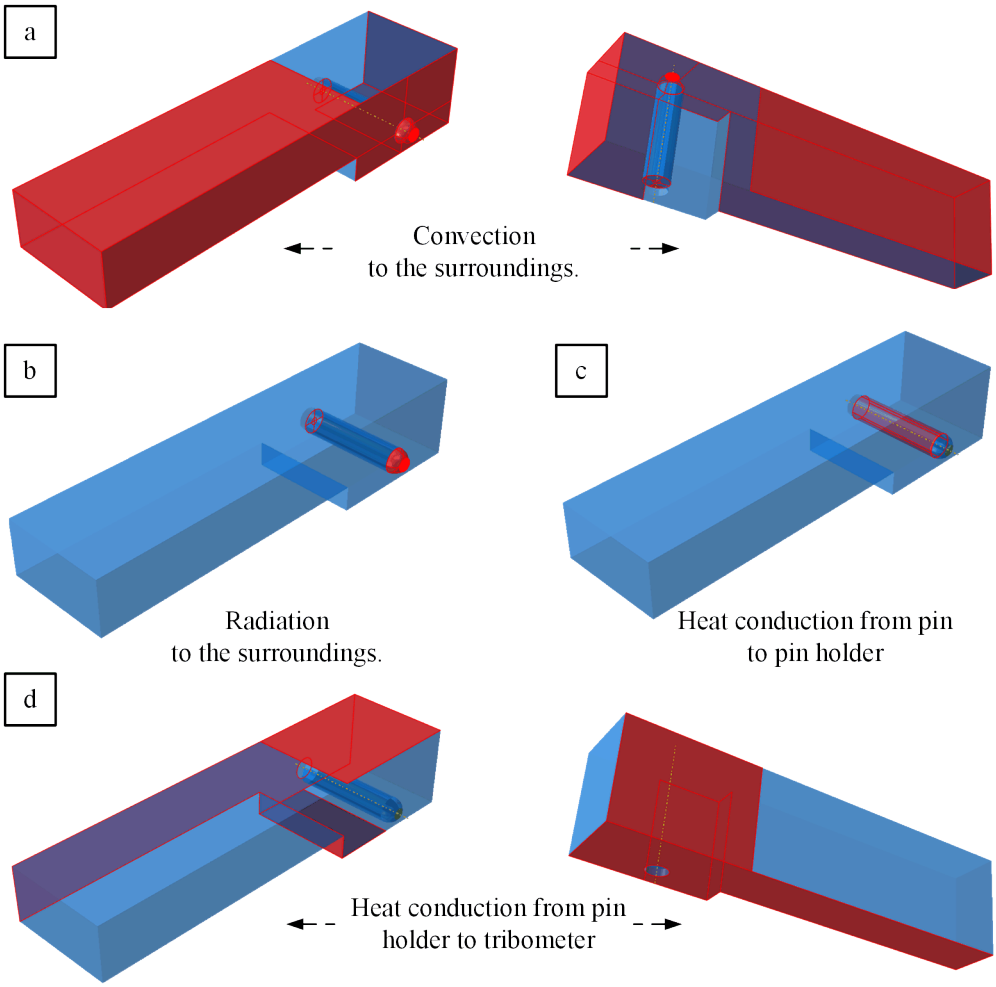

Figure 2.11: Description of the boundary conditions.

pin holder & tribometer is set to 200 $K \cdot mm^2 \cdot W^{-1}$ and 1000 $K \cdot mm^2 \cdot W^{-1}$ individually. The heat source is around 65.2 W, which is the sum value the heat flux multiplied by the nodal area (HFLA) when macroscopic sliding velocity V_{macro} is at 2 $m \cdot s^{-1}$ and loading is 500 N. The details about the boundary conditions are presented in Table 2.4.

2.5.3 Numerical results of the implicit heat transfer model

The implicit model simulates 30 s of the scratch process, and the evolution of node temperature is shown in Fig. 2.12. The average temperature is the average value the node temperature extracted from the corresponding location of selected area (red node) in Fig. 2.12b. The most interesting aspect of this curve is that the average temperature is increasing up to around 20 s and then tend to be constant. It indicates that it take

Table 2.4: Boundary conditions.

Name	Unit	Value
Heat source	[W]	65.2
Convective heat transfer	$[W \cdot m^{-2} \cdot K^{-1}]$	50
TCR between pin holder & tribometer	$[K \cdot mm^2 \cdot W^{-1}]$	1000
Radiation heat transfer	emissivity coefficient	0.82
TCR between pin & pin holder	$[K \cdot mm^2 \cdot W^{-1}]$	200

around 20 s for the system to reach thermal balance conditions.

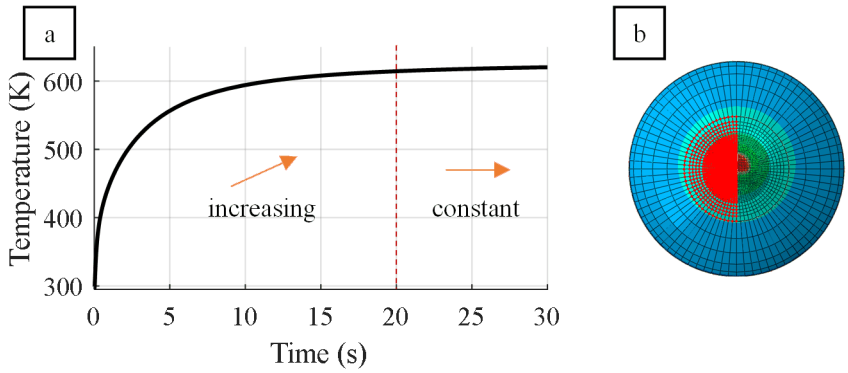

Figure 2.12: Evolution of average node temperature (a), and the corresponding location of selected area (b).

A sliding time of 30 s is simulated, and the resulting node temperature distribution is shown in Fig. 2.13. The max temperature $T_{max-imp}$ on the center of the pin reached around 1374 K. For the pin holder, the max temperature is around 350 K at the edge of the hole. This is due to the TCR plays a significant part in the heat conduction.

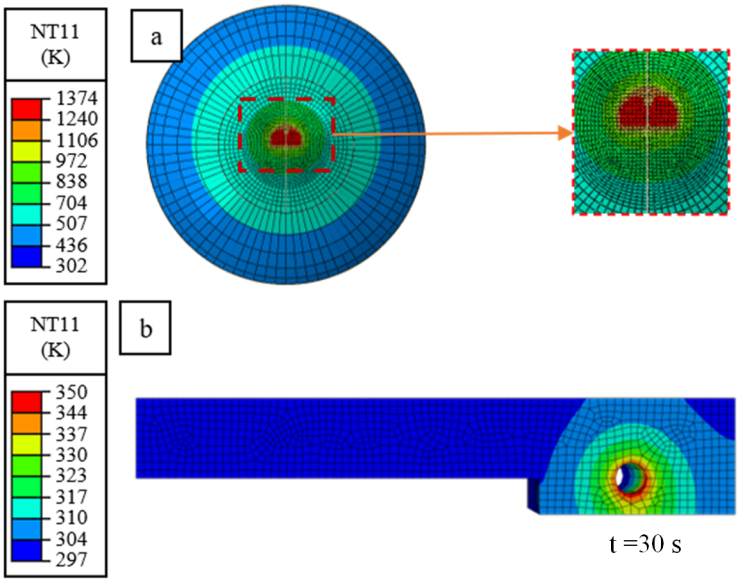

Figure 2.13: Node temperature distribution of implicit heat transfer model at end of the simulation (t=30 s), (a) pin and (b) pin holder.

We know that the temperature difference between pin & pin holder is critically high due the TCR, based on Fig. 2.13. Nevertheless, it still does not display the temperature difference at the pin & pin holder's contact zone. Fig. 2.14a shows the evolution of node temperature alone line AB verse coordinate of the Z-axis. Line AB is presented in Fig. 2.14b. The node temperature suddenly crashed at z equals ±4mm, which is the interface between the pin & pin holder. As mentioned before, the TCR between pin & pin holder have a critical influence on system thermal balance.

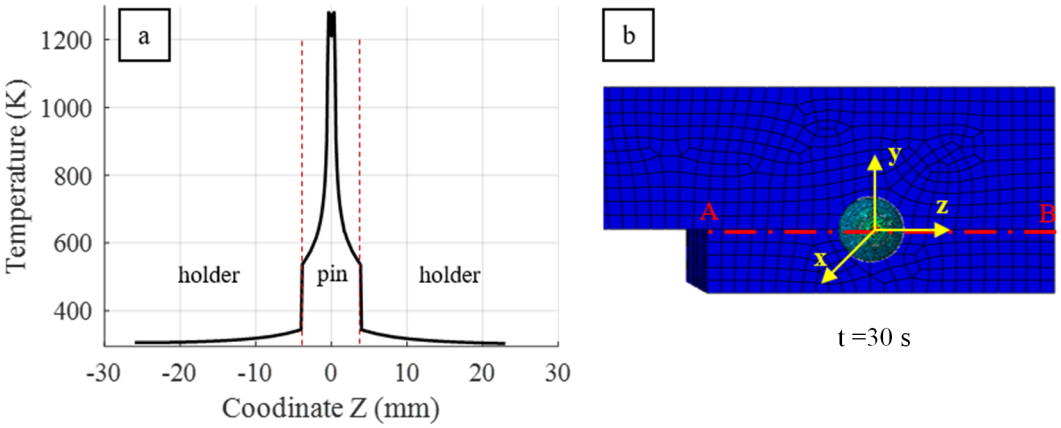

Figure 2.14: Evolution of node temperature verse coordinate Z (a) and the corresponding location of the selected area (b).

2.6 Sensitivity analysis of implicit heat transfer model

As several uncertainties remain regarding the applied boundary conditions of the implicit model, a sensitivity analysis has been carried out to assess their impact and the most important ones.

2.6.1 Convective heat transfer

The heat exchange with the environment is considered first. In this part the heat exchange by convection is studied. The relative surface which corresponded the convection is shown in Fig. 2.15. The boundary conditions is presented in Table 2.5. The convection heat transfer coefficient is assumed from 25 $W \cdot m^{-2} \cdot K^{-1}$ to 75 $W \cdot m^{-2} \cdot K^{-1}$. The steady-state heat flux distribution is imported from the numerical results of the explicit scratch model and applied in the 3D thermal model. The heat flux density is around 65.2 W, which is imported from the explicit numerical results with macroscopic sliding velocity V_{macro} of 2 $m \cdot s^{-1}$ and loading of 500 N. The emissivity coefficient of the carbide pin is assumed at 0.82. TCR between pin and pin holder and between pin holder and tribometer is set to 200 $K \cdot mm^2 \cdot W^{-1}$ and 1000 $K \cdot mm^2 \cdot W^{-1}$ individually. A sliding time of 30 s is simulated.

The resulting evolution of average node temperature under different convection conditions is shown in Fig. 2.16a & b. The node temperature is extracted from the selected area of Fig. 2.16c. The temperature difference is less than 7 K at the end of the

Table 2.5: Boundary conditions - various convective heat transfer.

Name	Unit	Value
Heat flux density	[W]	65.2
Convective heat transfer	$[W \cdot m^{-2} \cdot K^{-1}]$	25, 50, 75
TCR between pin holder & tribometer	$[K \cdot mm^2 \cdot W^{-1}]$	1000
Radiation heat transfer	emissivity coefficient	0.82
TCR between pin & pin holder	$[K \cdot mm^2 \cdot W^{-1}]$	200

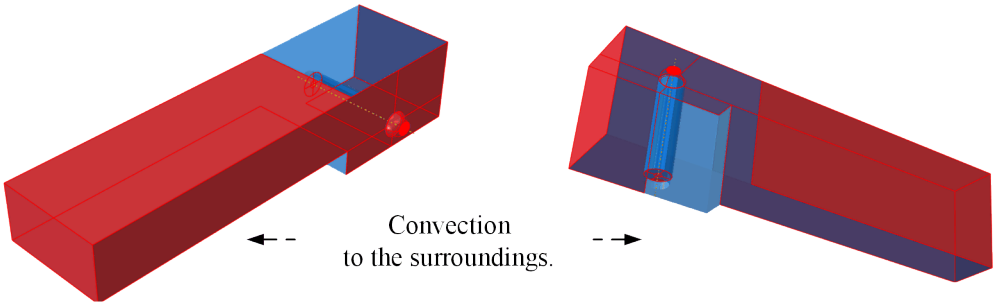

Figure 2.15: Surfaces corresponded with boundary conditions: convection.

simulation process. It indicates that the convective heat transfer has a slight influence on the temperature distribution at pin tips.

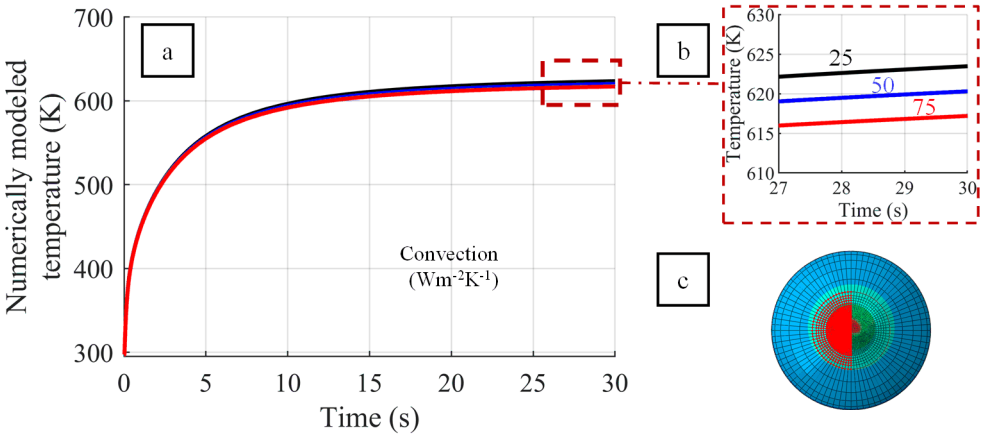

Figure 2.16: Evolution of average node temperature under different convection conditions (a), partial enlarged detail (b), and the correspond location of selected area (c).

2.6.2 Radiation heat transfer

The second part investigates the influence of radiation to the surroundings on temperature distribution at pin tips. The relative surface which corresponded the convection is shown in Fig. 2.17. The boundary conditions is presented in Table 2.6. The emissivity coefficient of the carbide pin is assumed at 0.25, 0.5, and 0.82 [153]. The convection heat transfer coefficient is set at 50 $W \cdot m^{-2} \cdot K^{-1}$. The heat flux density is around 65.2 W, which is imported from the explicit numerical results with macroscopic sliding velocity V_{macro} of 2 $m \cdot s^{-1}$ and loading of 500 N. TCR between pin & pin holder and between pin holder & tribometer is set to 200 $K \cdot mm^2 \cdot W^{-1}$ and 1000 $K \cdot mm^2 \cdot W^{-1}$ individually. A sliding time of 30 s is simulated.

Table 2.6: Boundary conditions - various emissivity coefficient.

Name	Unit	Value
Heat flux density	[W]	65.2
Convective heat transfer	$[W \cdot m^{-2} \cdot K^{-1}]$	50
TCR between pin holder & tribometer	$[K \cdot mm^2 \cdot W^{-1}]$	1000
Radiation heat transfer	emissivity coefficient	0.25, 0.5, 0.82
TCR between pin & pin holder	$[K \cdot mm^2 \cdot W^{-1}]$	200

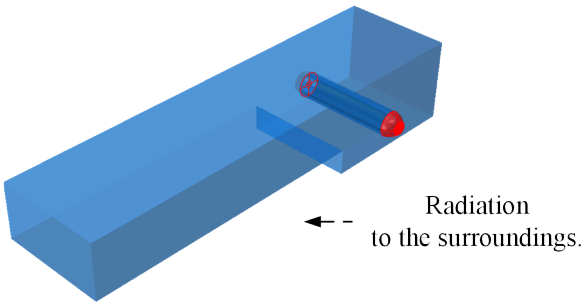

Figure 2.17: Surfaces corresponded with boundary conditions: radiation.

Fig. 2.18a & b shows the evolution of average node temperature with various emissivity coefficient, which is selected from Fig. 2.16c. No significant differences between these curves, and the max temperature difference is only around 2 K. This result may be explained by the fact that, as Fig. 2.13 shows, only a small part of the center of the pin tip reach relatively high temperature. The radiation phenomena is not obvious.

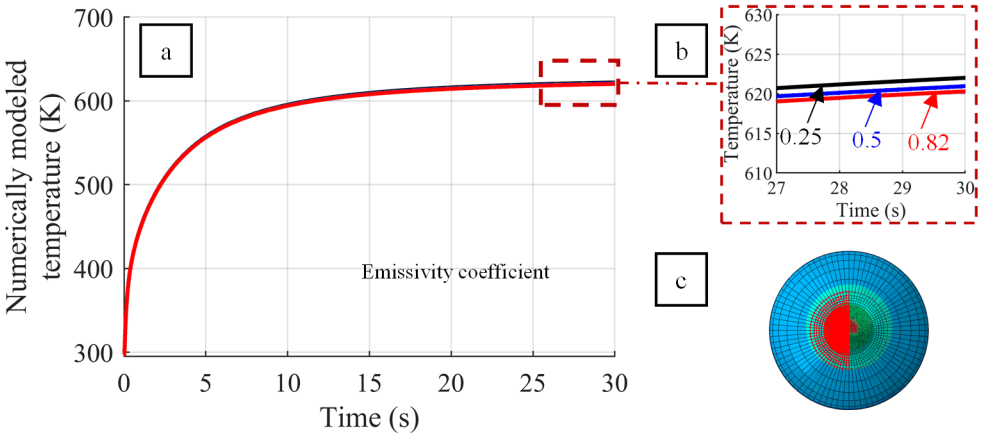

Figure 2.18: Evolution of average node temperature with different emissivity coefficient (a), partial enlarged detail (b), and the correspond location of selected area (c).

2.6.3 TCR between pin holder & tribometer

Due to the pin holder is fixed in the tribometer, TCR between pin holder & tribometer is considered in this part. The relative surface which corresponded the convection is shown in Fig. 2.19. The boundary conditions is presented in Table 2.7. For the TCR, TCR = 1 $K \cdot mm^2 \cdot W^{-1}$ means the thermal perfect contacts, where almost no thermal resistance in the interface. While the TCR = ∞ $K \cdot mm^2 \cdot W^{-1}$ means the thermal

isolated contacts, where the energy can not exchange at al. Furthermore, based on previous research [23], the TCR between pin & pin holder could be assumed as 100, 1000 $K \cdot mm^2 \cdot W^{-1}$.

For other boundary conditions, the heat flux density is around 65.2 W. The convective heat transfer coefficient is 50 $W \cdot m^{-2} \cdot K^{-1}$. The emissivity coefficient of the carbide pin is assumed at 0.82. TCR between pin and pin holder is set to 200 $K \cdot mm^2 \cdot W^{-1}$. A sliding time of 30 s is simulated.

Table 2.7: Boundary conditions - various TCR between pin holder & tribometer.

Name	Unit	Value
Heat flux density	[W]	65.2
Convective heat transfer	$[W \cdot m^{-2} \cdot K^{-1}]$	50
TCR between pin holder & tribometer	$[K \cdot mm^2 \cdot W^{-1}]$	1, 100, 1000, ∞
Radiation heat transfer	emissivity coefficient	0.82
TCR between pin & pin holder	$[K \cdot mm^2 \cdot W^{-1}]$	200

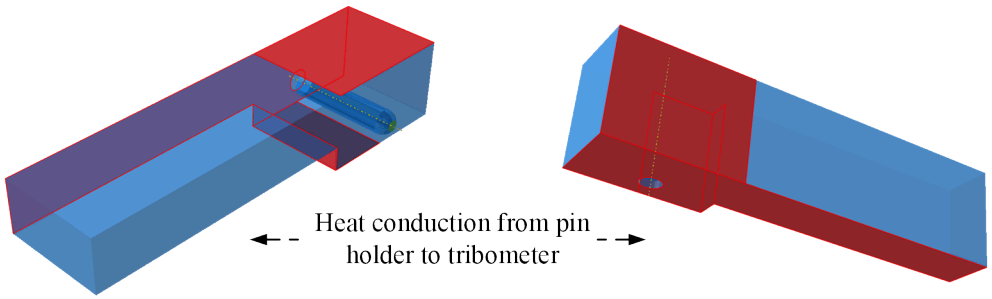

Figure 2.19: Surfaces corresponded with boundary conditions: TCR between pin holder & tribometer.

As Fig. 2.20a & b shows, the evolution of average node temperature with various TCR between pin holder & tribometer, which is selected from Fig. 2.20c. Due to the TCR = 1 $K \cdot mm^2 \cdot W^{-1}$ imply the thermal perfect condition and the TCR = ∞ $K \cdot mm^2 \cdot W^{-1}$ imply the thermal isolated condition. The max temperature difference, which is less than 8 K at the end of simulation, indicates that the TCR between pin holder & tribometer does not significantly influence temperature distribution at pin tip.

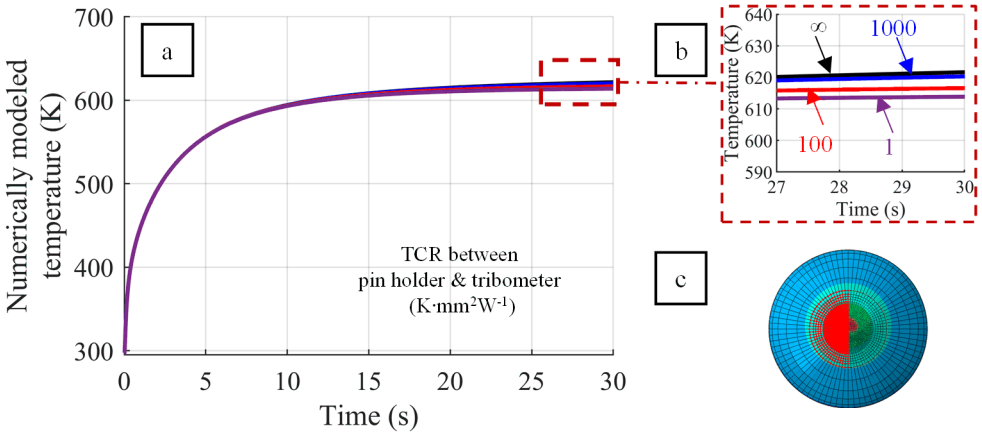

Figure 2.20: Evolution of average node temperature with different TCR between pin holder & tribometer (a), partial enlarged detail (b), and the correspond location of selected area (c).

2.6.4 TCR between pin & pin holder

As the pin is fixed in the pin holder, heat flux conducts from pin to pin holder. This part focus on the TCR between pin & pin holder. The relative surface which corresponded the convection is shown in Fig. 2.21. The boundary conditions is presented in Table 2.8. The thermal perfect conditions and thermal isolated conditions are considered, as well. The TCR between pin & pin holder is assumed as 1, 100, 200, 500, 1000, and ∞ $K \cdot mm^2 \cdot W^{-1}$. For other boundary conditions, the heat flux density is around 65.2 W. The convective heat transfer coefficient is 50 $W \cdot m^{-2} \cdot K^{-1}$. The emissivity coefficient of the carbide pin is assumed at 0.82. TCR between pin holder & tribometer is set to 1000 $K \cdot mm^2 \cdot W^{-1}$. A sliding time of 30 s is simulated.

Table 2.8: Boundary conditions - various TCR between pin & pin holder.

Name	Unit	Value
Heat flux density	[W]	65.2
Convective heat transfer	$[W \cdot m^{-2} \cdot K^{-1}]$	50
TCR between pin holder & tribometer	$[K \cdot mm^2 \cdot W^{-1}]$	1000
Radiation heat transfer	emissivity coefficient	0.82
TCR between pin & pin holder	$[K \cdot mm^2 \cdot W^{-1}]$	1, 100, 200, 500, 1000, ∞

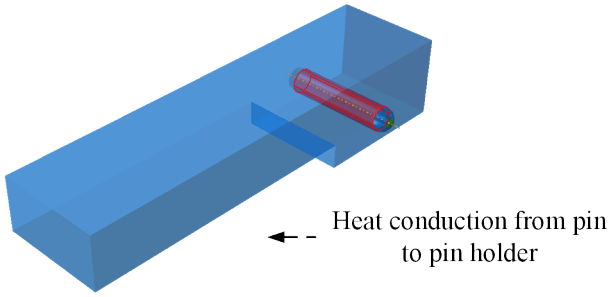

Figure 2.21: Surfaces corresponding the boundary conditions: TCR between pin & pin holder.

As Fig 2.22 shows, there was a significant difference between the evolution of average node temperature with TCR between pin & pin holder and other boundary conditions. This result may be explained by the fact that the heat flux could only conduct from pin to pin holder via the interface in which TCR between pin & pin holder plays a significant part in the heat conduction.

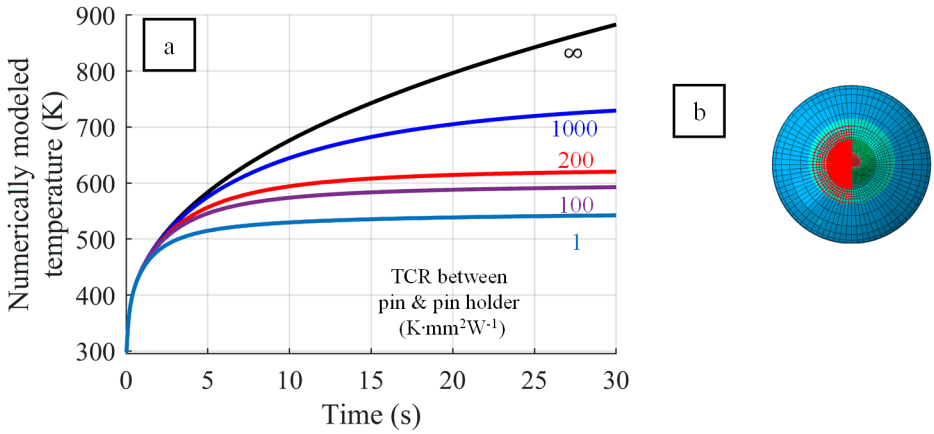

Figure 2.22: Evolution of average node temperature with different boundary conditions TCR between pin & pin holder(a), and the corresponding location of selected area (b)

Furthermore, in order to clearly identify the influence of TCR between pin & pin holder on temperature distribution at the pin - pin holder interface, the evolution of temperature alone line AB at the end of the simulation (time = 30 s) verse coordinate of the Z-axis is presented in Fig. 2.23a & b. The corresponding location of line AB is shown in Fig. 2.23c. The boundary conditions are shown in Table 2.8. It is evident that the node temperature still crashed at the interface between the pin & pin holder. As mentioned before, the TCR between pin & pin holder significantly affects the temperature distribution.

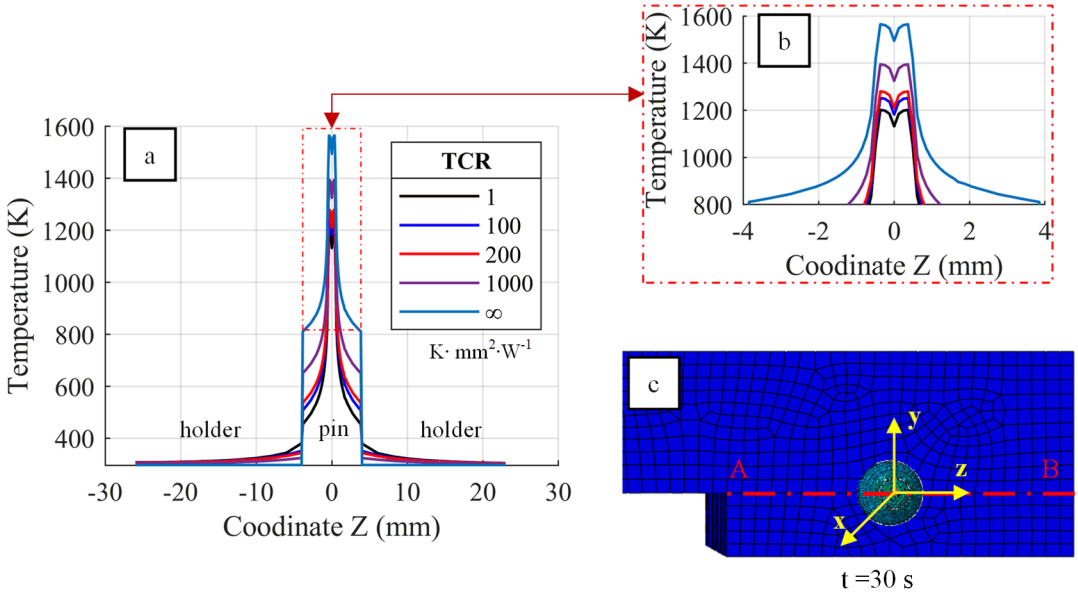

Figure 2.23: Evolution of node temperature verse coordinate Z at 30 s under different TCC (a), partial enlarged detail (b), and the corresponding location of selected area (c).

2.7 Summary

A numerical modeling strategy to estimate the 3D temperature distribution at the interface during a pin-on-bar frictional test under severe contact conditions is presented. Two 3D Finite Element (FE) models based on commercial code ABAQUS have been established to simulate local thermo-mechanical loadings. The first explicit scratch model showed that the total power transmitted to the friction pin is almost constant after 4 ms of sliding, making it possible to be used as a boundary condition in a long time scale model.

The second implicit heat transfer model showed that, after applying the heat input extracted from the scratch model, the 20 s were needed to reach the thermal balance within the system. The dedicated methodology could simulate the temperature within such contact properly. The sensitivity analysis of the implicit heat transfer model shows that the TCR between pin & pin holder is the critical boundary condition. It affects not only the final temperature reached by the pin but also the heating rate by controlling the dissipation rate to the pin holder. This study finally shows that, in order to get a more reliable 3D temperature distribution at the contact interface, a proper calibration of the TCR between pin & pin holder is highly required.

3 Calibration of thermal contact resistance

Summary

Objective of this chapter

Preliminary sensitivity investigations have highlighted that TCR between the pin and the pin-holder is, by far, the most critical parameter to estimate in order to model heat transfer properly in the tribometer. Even if the interface pin & pin-holder is located some millimeters away from the pin-workpiece interface, it can significantly influence the heat transfer.

This chapter examines a method to calibrate pin & pin holder TCR by an inverse thermal method. A laser source heats either a pin alone or a pin+pin-holder system

equipped with thermocouples. A FE model is employed to simulate heat transfer on the one hand between the laser and the pin, and the other hand, between the pin and the pin-holder. Actual TCR is adjusted based on the best fit between experimental and simulated thermocouples temperature.

3.1 Experimental design

3.1.1 Identification of the laser efficiency ratio

The sufficient heat transmitted to the pin cannot be easily assessed as it depends on the laser power, material absorptivity, wavelength, and temperature. Schneider et al. found that the absorptivity could reach up to 80% for steel and aluminum with pick power of 15 kW. In contrast, the absorptivity was only 40% for steel and close to 0 for aluminum with 2 kW pick power [154] So, the identification of the TCR requires first to estimate the efficiency ratio of the laser. The efficiency ratio is calculated based on equation 3.1

$$\lambda = \frac{P_{\text{actual}}}{P_{\text{laser}}} \times 100\% \tag{3.1}$$

Where the λ is the efficiency ratio of the laser. The P_{actual} is the actual power (W) that penetrates the interface and heats the materials. The P_{laser} is the power of the laser (W).

To identify the effective heat input, as Fig. 3.1 shows, the laser source (Fig. 3.1a) is applied on the pin alone considered as insulated. The heating source (Fig. 3.1b) is a continuous Ytterbium fiber laser YLR-4x200W-SM with a wavelength of 1070 nm. The support (Fig. 3.1c) is made of a vermiculite plate. Two K thermocouples TC1 and TC2 with a diameter of 0.2 mm (Fig. 3.1d) are located on a defined position on the pin. The distance between the tip of the pin and the thermocouple is 8.5 mm. The temperature is measured with a multichannel data acquisition system at 75 Hz. The pins are made of non-coated tungsten carbide H13A (Sandvik) with a cylindrical shape and a spherical tip with a radius of 8.5 mm. Its length is 30 mm, and its diameter is 8 mm. The laser beam is focused on the spherical tip of the pin with a beam diameter of 800 µm fixed at 100 W (Fig. 3.1e), mimicking the diameter of the contact zone during the friction test. The identification procedure of the laser efficiency ratio will be presented in 3.2.1.

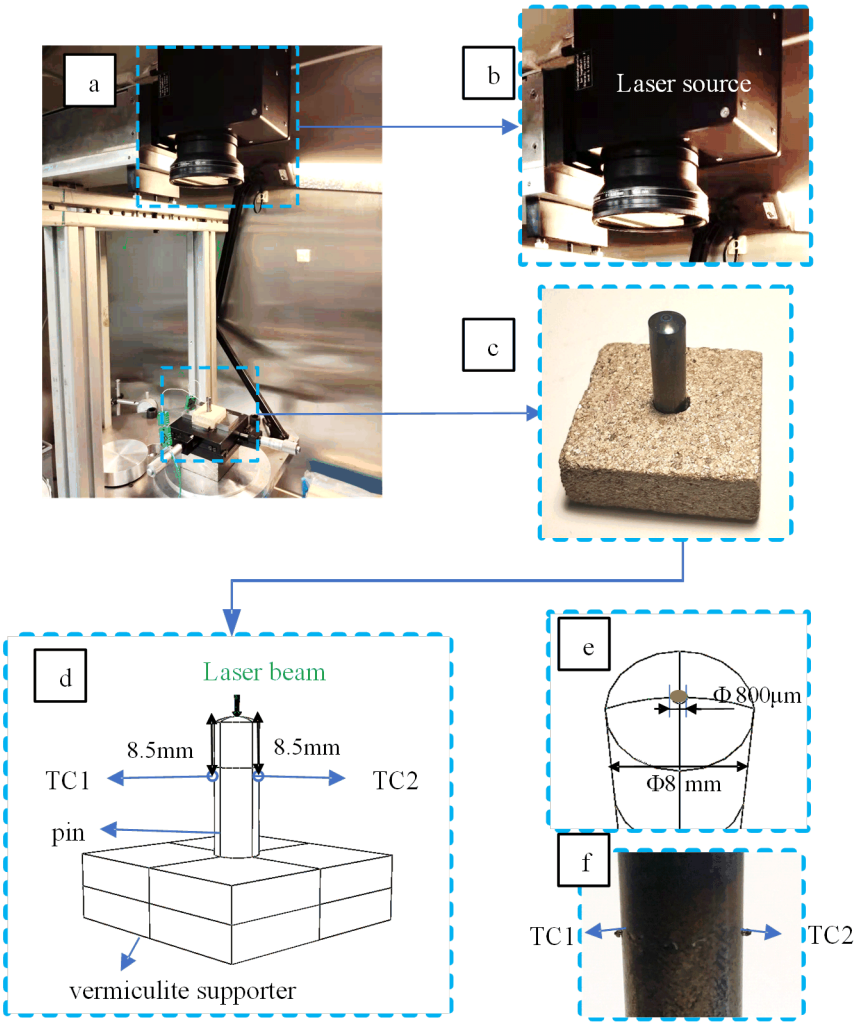

Figure 3.1: Experimental set-up with a) an overview of the bench, b) laser source, c) the pin alone configuration, d) scheme of the configuration, e) scheme of the tip of pin, f) photo of the junction area of thermocouples.

3.1.2 Identification of the thermal contact resistance between the pin and the pin holder

With the laser's estimated efficiency ratio, the TCR could be identified with the second configuration, the pin fixed in the pin holder.

As Fig. 3.2a shows, the pin is fixed in the pin holder, and the pin holder is made of C45 medium carbon steel. A proper fitting of the pin in the pin holder is ensured by screws that have to be carefully tightened. The tightening torque was kept constant at 10 m · N so as to avoid any influence on the identification of the TCR. During heating,

the same lasering conditions were also applied on the pins. The identification of the TCR between the pin and the pin holder requires applying a finely controlled heat source on the spherical tip of pins and then to monitor the temperatures on different locations on the pin holder with thermocouples (TC3 and TC4 in Fig. 3.2c) with a diameter of 0.8mm. The location of the thermocouple is shown in Fig. 3.2d.

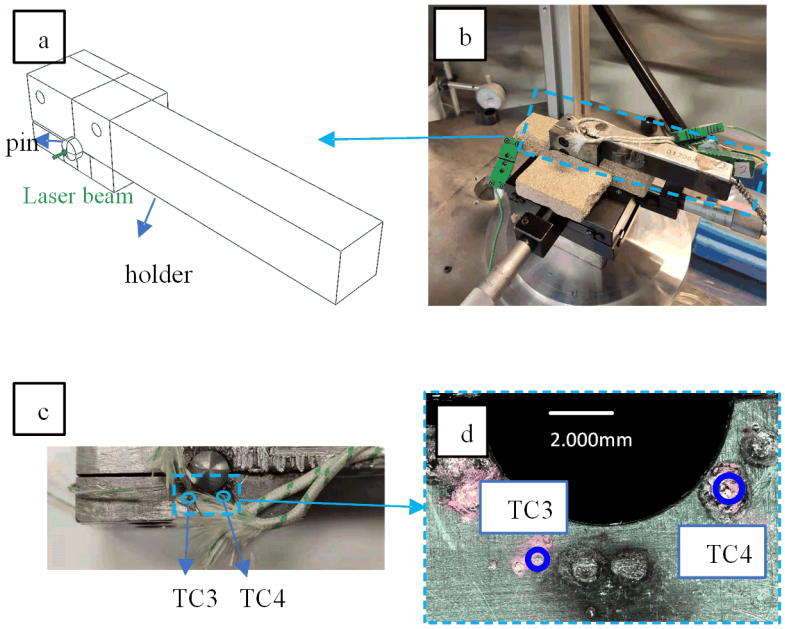

Figure 3.2: Experimental device and heating configurations of heating of the pin fixed in the pin holder.

3.1.3 Numerical model for calibration

In parallel to these two experimental campaigns, i.e., pin alone and pin+pin holder, the corresponding heat transfer was developed, as shown in Fig. 3.3a and Fig. 3.4a. The first model considers the pin alone (Fig. 3.3a). In a constant heat flux model, the laser source is applied on the spherical tip and is defined by its diameter (800 µm) and its heat flux density. The 3D finite element heat transfer models are composed of 8-node linear brick elements. The mesh size was refined down to 0.4 mm close to the tip of the pin (Fig. 3.3d), and the size gradually increases up to 1 mm at the bottom of the pin (Fig. 3.3c). The average mesh size of the vermiculite supporter is around 2 mm.

The ambient temperature is considered to be 297 K. The thermal properties of tungsten carbide are referred in Table 2.1, and the thermal properties of vermiculite are referred to from N. Low [155], which is shown in Table 3.1. Heat transfer with air by radiation and convective heat transfer are considered. The emissivity coefficient of the tungsten

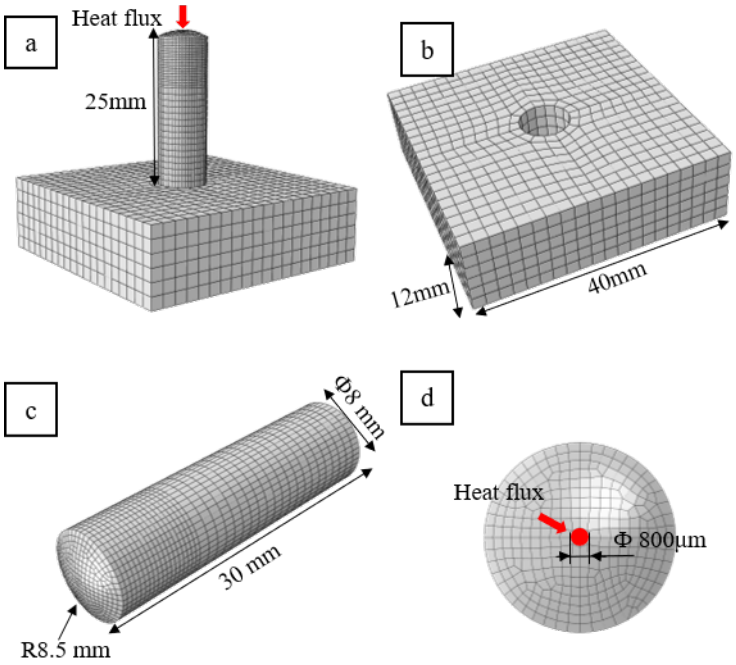

Figure 3.3: Numerical heat transfer model of pin in support.

carbide is assumed at 0.82 since Kieruj et al. [153].

Table 3.1: Properties of the vermiculite.

Temperature [K]	Density [$kg \cdot m^{-3}$]	Specific heat [$J \cdot kg^{-1} \cdot K^{-1}$]	Thermal conductivity [$W \cdot m^{-1} \cdot K^{-1}$]
293	130	840	0.06

The second model takes into account the pin mounted into the pin holder. For the pin holder, the mesh size was refined down to 0.015mm close to the junction area of the thermocouples (Fig. 3.4b). The size gradually increases up to 2 mm at the edge of the holder (Fig. 3.4d). For the pin, the mesh size was refined down to 0.4 mm close to the pin's tip, and the size gradually increases up to 1 mm at the bottom of the pin (Fig. 3.4c). The ambient temperature is considered to be 297 K. The thermal properties of tungsten carbide and C45 steel are referred to in Table 2.1 and Table 2.3.

The distance between the pin tip to TC1 and TC2 are almost the same, which equals 8.5 mm (Fig. 3.2d). The laser beam is applied at the center of the pin tip. Theoretically, the experimentally measured temperature of TC1 and TC2 should be the same. Therefore, as Fig. 3.5a shows, only one node set is considered, which corresponds to the junction

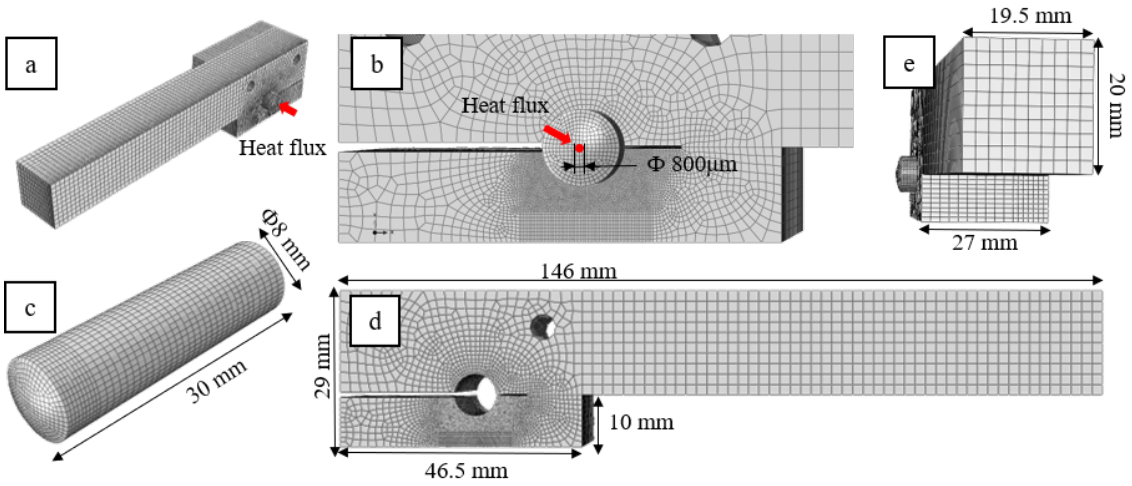

Figure 3.4: Numerical heat transfer model of pin in pin holder.

area of the thermocouples TC1 and TC2 (Fig. 3.5b). Fig. 3.5c shows the node sets corresponded to the junction area of the thermocouples TC3 and TC4 resulting from the soldering procedure (Fig. 3.5d). The average contact temperature of these node sets was computed and compared to the experimentally measured temperatures.

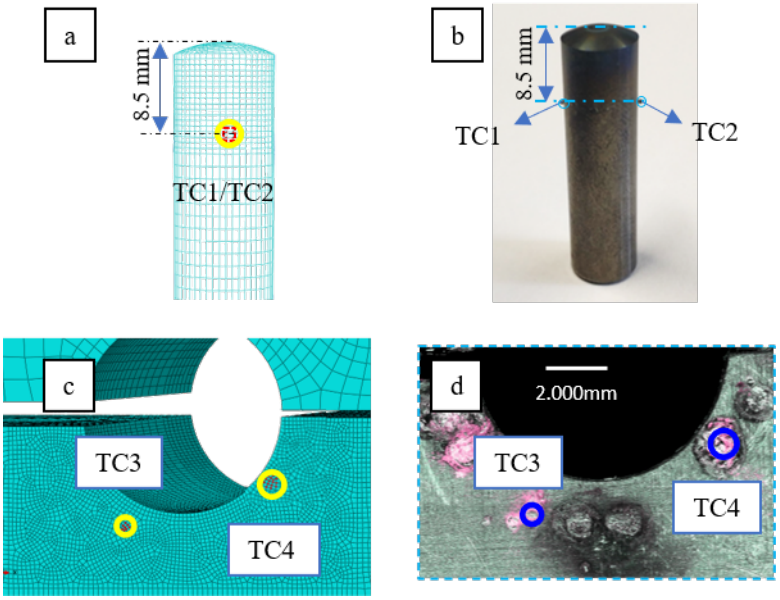

Figure 3.5: Location of the extracted simulated temperatures a) pin, b), photo of the pin with the junction area c) pin holder and d) photo of pin holder with the junction area.

3.2 Calibration procedure

During the laser heating test, the laser power is constant value 100 W. However, due to reflection and other physical phenomena, the real heat power which penetrated the interface and heated the body is still uncertain. The first part is to adjust the heating power of the numerical model to fit the experimental results, which are measured by thermocouples TC1 and TC2 (Fig. 3.5a & b). Based on the estimated heating power, the second part is to adjust the thermal contact resistance TCR to fit the experimental results, which are measured by thermocouples TC3 and TC4(Fig. 3.5c & d).

3.2.1 Laser heating test

For the laser heating test, the heating cycle is selected as Fig. 3.6. The heating process tests 18 s, while the cooling process by convection tests 10 s.

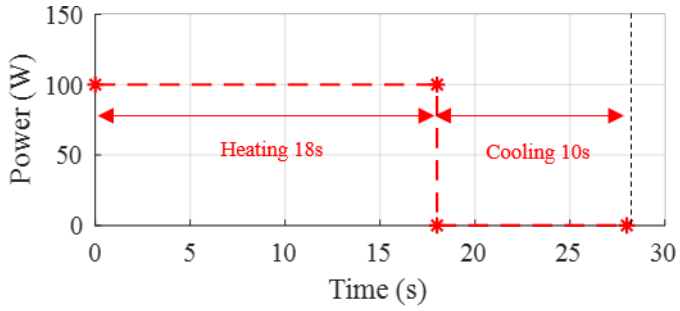

Figure 3.6: The heating cycle of the laser heating test.

The distance between the pin tip to TC1 and TC2 are almost the same, which equals 8.5 mm (Fig. 3.2d, Fig 3.5b). Theoretically, the experimentally measured temperature of TC1 and TC2 should be the same. Due to the laser beam's location at the pin tip or the conjunction area thermocouples, the experimentally measured temperature is not the same. In contrast, the max temperature difference is less than 5 K. Fig. 3.7a shows the evolution of the average temperature of TC1 and TC2 on the pin versus time of heating pin alone (Fig. 3.7b). Fig. 3.7c shows the evaluation of the average temperature of TC3 and TC4 individually of pin in pin holder (Fig. 3.7d). The maximum temperature is around 542 K of heat of pin alone, while the maximum temperature is around 332 K (TC3) and 334 K (TC4).

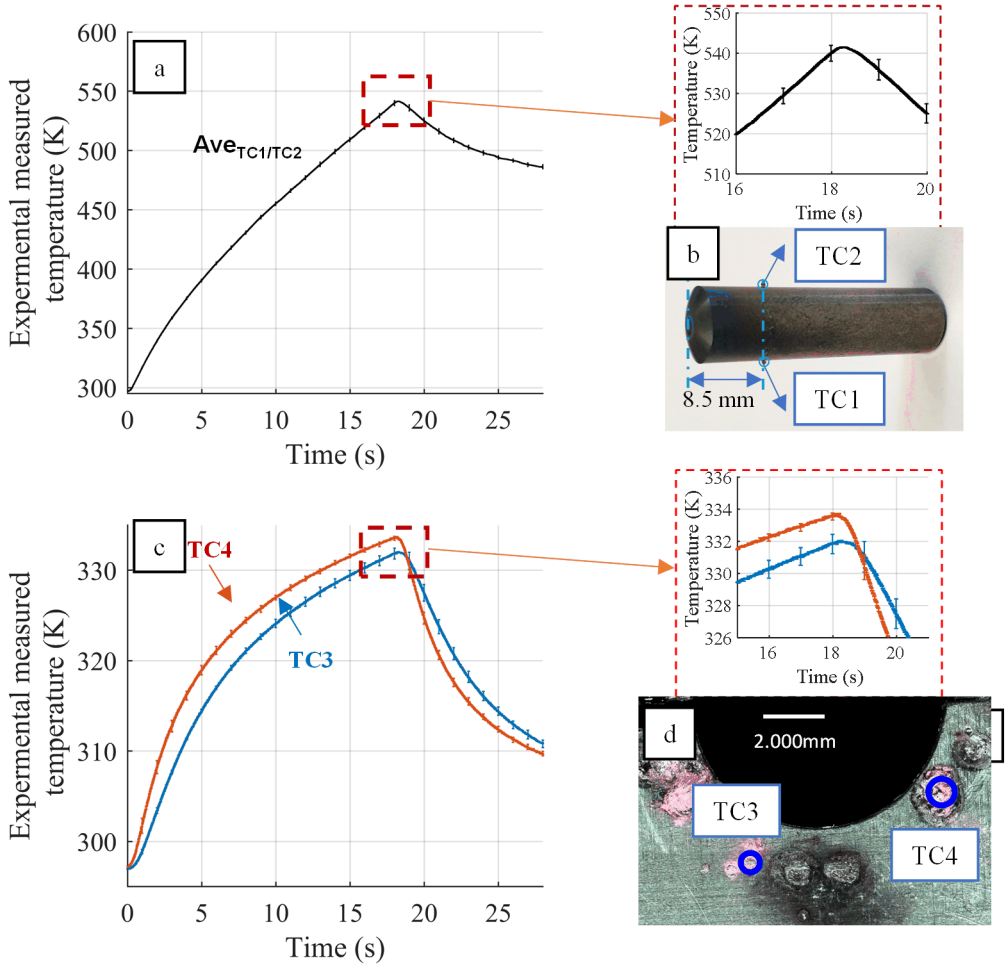

Figure 3.7: Experimental results: heating and cooling curve of heating a) pin alone and c) pin fixed in the pin holder.

3.2.2 Calibration of pin alone, the real heat power

Due to the uncertain reflection and other physical phenomena, it is possible to estimate the real heat power which penetrates the interface and heat the materials. Since the pin is contacted with supporter (Fig. 3.5) in the atmospheric environment (ambient temperature is considered as 297 K), several boundary conditions are verified: the heat transfer between pin and supporter, heat transfer by radiation, and convective heat transfer with surroundings.

In this section, the sensitivity analysis of the pin alone model is completed first to identify the most critical boundary condition contributed to the temperature distribution. The first step is to identify the most critical boundary condition by sensitivity analysis.

The second step is to adjust the heating power and the most critical boundary condition to fit the experiment result. The influence of different boundary conditions on the numerical simulated temperature of nodes set TC1/TC2 (Fig. 3.5a) is shown in Fig. 3.8.

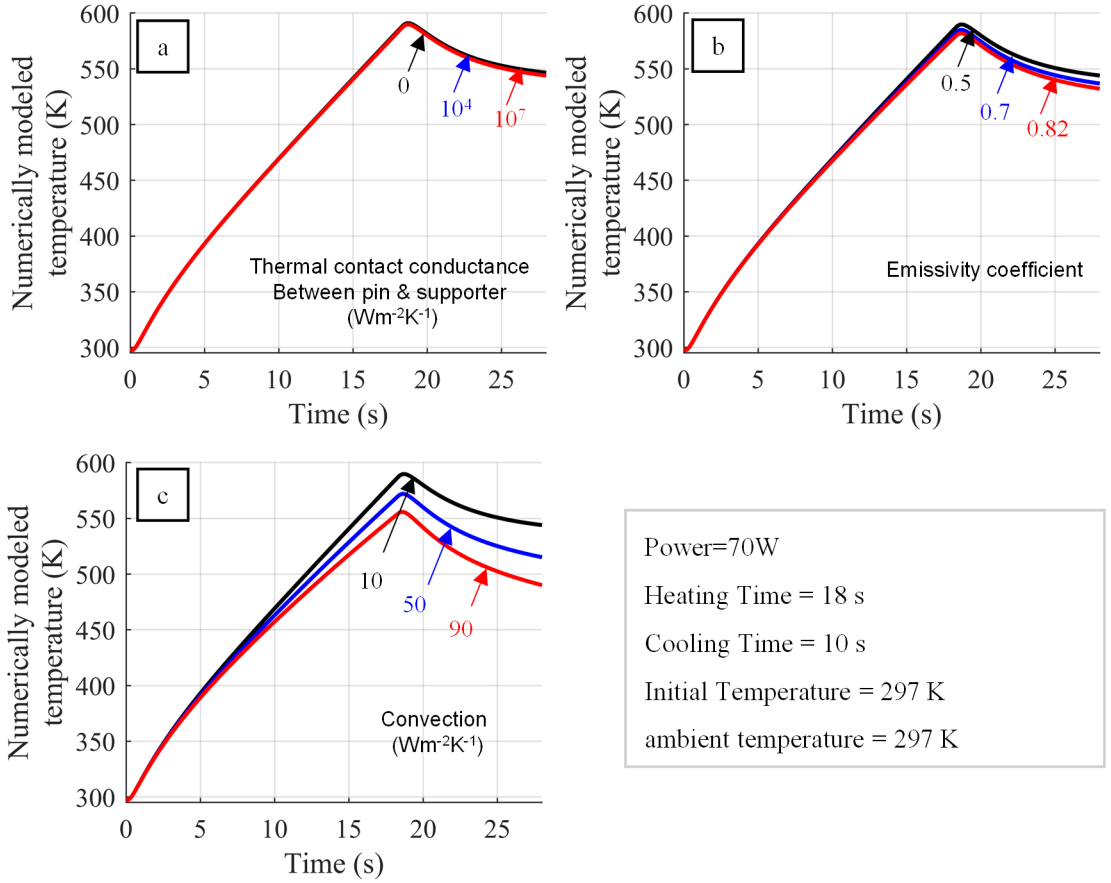

Figure 3.8: Heating and cooling curve under different conditions, a) heat transfer between pin and supporter, b) heat transfer by radiation, and c) convective heat transfer with air.

Fig. 3.8a shows the influence of thermal conductance between pin and supporter. The max temperature difference is less than 4 K. It indicates that the heat transfer between pin and supporter could be ignored. Fig. 3.8b shows the influence of heat transfer by radiation. The max temperature difference is less than 16 K. The heat transfer by radiation should be considered. Thus the emissivity coefficient is considered as 0.82 based on the research of Kieruj et al. [153]. Fig. 3.8c shows the influence of heat transfer by convection. The max temperature difference is over 70 K. It is evident that the convective heat transfer plays a significant role in heat loss.

The second step is to adjust the heating power and the heat transfer by convection to

fit the experimentally measured temperature. The emissivity coefficient is considered as 0.82 [153]. As Fig. 3.9 shows, The best agreement between pin experimental and numerical results are obtained when the heating source is 70 W, and the convective heat transfer coefficient is $50\,\mathrm{W\cdot m^{-2}\cdot K^{-1}}$). The max temperature difference is less than 5 K. Since the laser power is set to 100 W, only 70% of laser power penetrates the interface and finally heating the device.

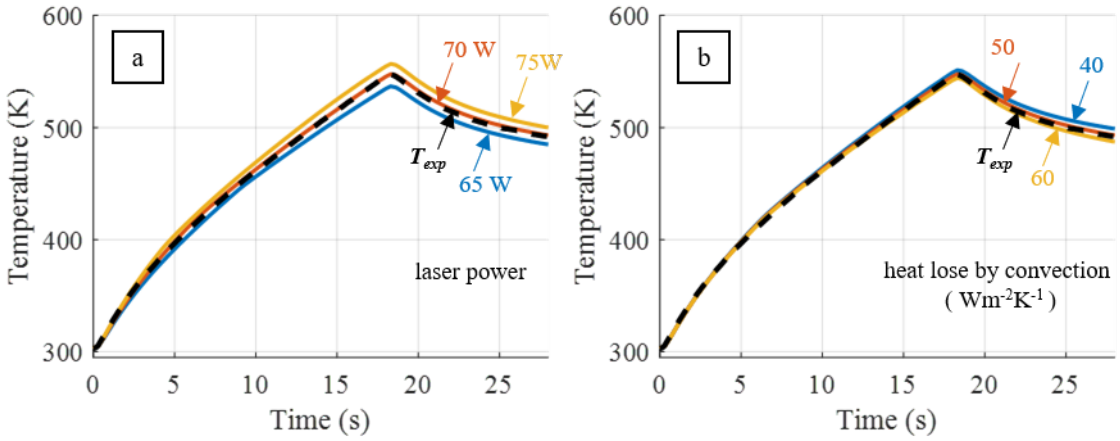

Figure 3.9: Verification of a) real heating power and b) convection coefficient.

With the calibrated heating power of 70 W and heat transfer by convection of $50\,\mathrm{W\cdot m^{-2}\cdot K^{-1}}$), the temperature distribution of the pin alone model is shown in Fig. 3.10. The initial temperature is 297 K. The max temperature at the tip of the pin is over 3000 K.

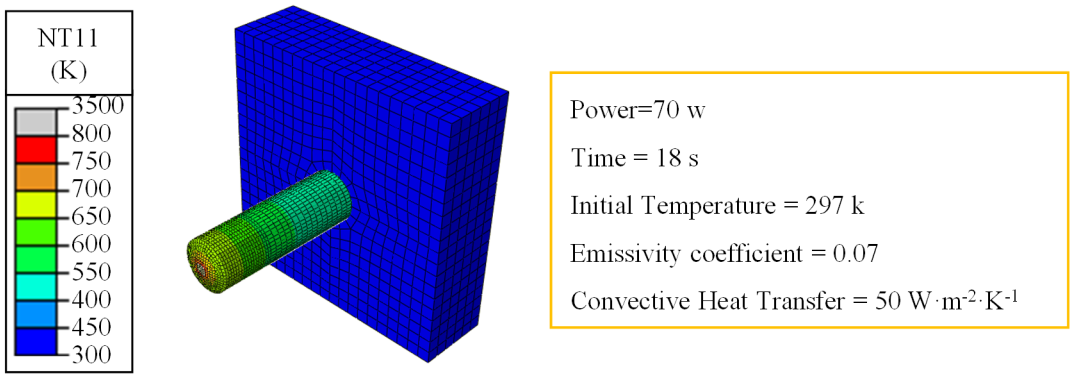

Figure 3.10: The temperature distribution of the heating of pin at the end of the heating process (18 s).

3.2.3 Calibration of thermal contact resistance between pin and pin holder

This identified input heat input 70 W was then applied into the second heat transfer model considering the whole system (pin+pin holder). The heat transfer by convection of 50 $W \cdot m^{-2} \cdot K^{-1}$) is still taken into account. As previously, the measured temperatures, thanks to two thermocouples TC3 and TC4 on the pin holder, were recorded for 28 seconds and compared with the simulated temperatures. A so-called "deviation coefficient" is calculated based on the Equation 3.2:

$$dev = \frac{1}{28s}\sqrt{\sum_{t=0}^{28s}\left[\left(T_{\exp_{TC3}} - T_{num_{TC3}}\right)^2 + \left(T_{\exp_{TC4}} - T_{\mathrm{num}_{TC4}}\right)^2\right]} \tag{3.2}$$

Where dev is the deviation between experimental and numerical data,$T_{exp-TC3}$ and $T_{exp-TC4}$ are the measured temperature (K) of TC3 and TC4 at time t, $T_{num-TC3}$ and $T_{num-TC4}$ are the numerically simulated temperature (K) of TC3 and TC4 at time t. Fig. 3.11 plots the deviation coefficient dev for a range of thermal contact resistance and reveals that the TCR minimizing the deviation is around 260 $K \cdot mm^2 W^{-1}$, which corresponds to a thermal contact conductance (TCC) around 3850 $W \cdot m^2 \cdot K^{-1}$.

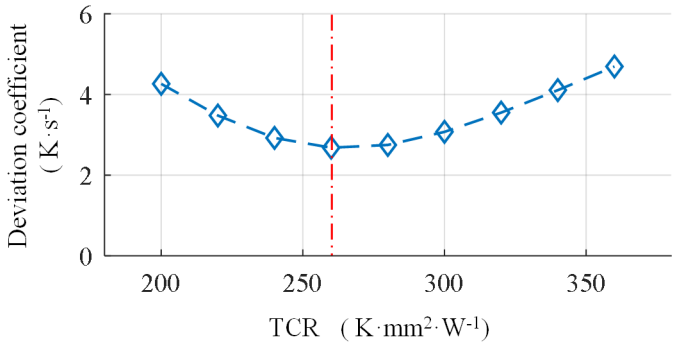

Figure 3.11: Evolution of the deviation coefficient Dev versus thermal contact resistance.

3.3 Verification of thermal contact resistance

3.3.1 Verification of thermal contact resistance with different heat cycles

Despite the thermal contact resistance TCR is calibrated in previous chapter, the TCR is only dependent on one heating cycle (Fig. 3.6). It is necessary to verify whether the TCR is appropriate to other different heating cycles or not. Furthermore, the temperature distribution at the interface under different TCR is compared in this section.

The first step to verify whether the estimated TCR value is an appropriate value for other heating cycles. Fig. 3.12 shows two heating cycles with the heating-cooling-heating-cooling process. The difference between test 1 (red curve) and test 2 (blue curve) is the cooling process. For test 1, the cooling process is 11 s + 9 s, while the cooling process is 12 s + 8 s for test2. During heating, the same lasering conditions were also applied on the pins.

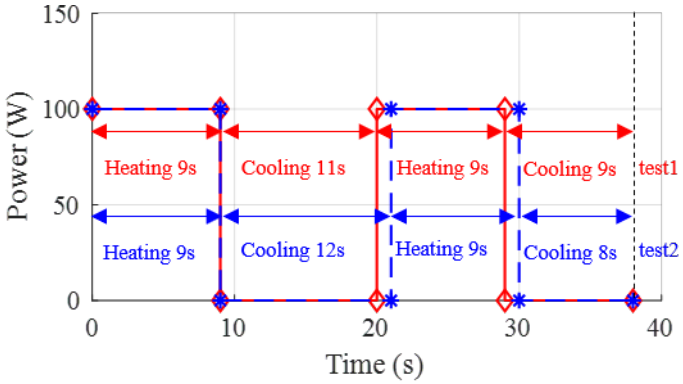

Figure 3.12: The heating cycle (38 s), verification of TCR.

Based on the heating cycle, laser heating experimental temperature and numerical results of test 1 and test 2 are compared in Fig. 3.13. The maximum temperature difference is less than 2.5 K in test 2. Numerical results based on the calibrated TCR are well-matched with the heating experiments. It indicates that the calibrated TCR is an appropriate value for different heating cycles.

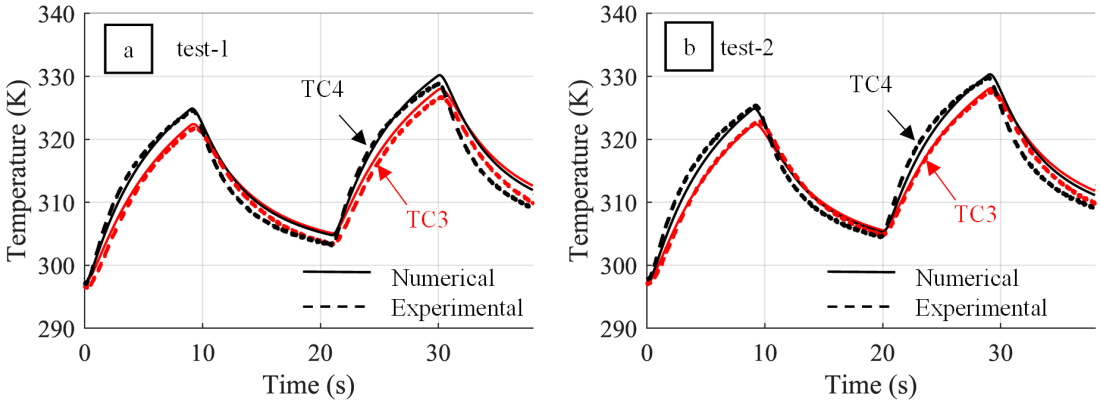

Figure 3.13: The comparison of numerical modeled and experimental measured temperature of TC3 and TC4 with different heating cycle: (a) test 1 and (b) test 2.

3.3.2 Temperature distribution with calibrated thermal contact resistance

This chapter's major issue is to calibrate the TCR to monitor the interface temperature distribution during the manufacturing process. Therefore the temperature distribution at the interface under different TCR is compared in this section. Based on the numerical model of pin fixed in pin holder, a series of the simulation were performed to investigate the temperature distribution on the tip of the spherical pin tip. The heating cycle is shown in Fig. 3.14. The heating process is 10 s, and the cooling process is 10 s.

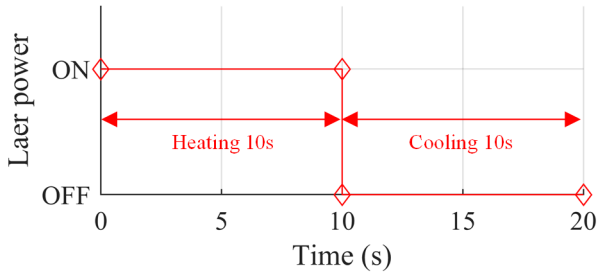

Figure 3.14: The heating cycle (20 s), comparison of different TCR.

The surface heat flux applied to the center of the spherical pin tip is assumed to 40 W and 50 W. For the TCR between pin and pin holder, in order to compare the actual contact interface with the thermally perfect contact interface and the thermally isolated contact interface, the TCR between pin and pin holder is considered as $1\,\mathrm{K\cdot mm^2W^{-1}}$ (TCC= $1\cdot10^6\,\mathrm{W\cdot m^{-2}\cdot K^{-1}}$)) and $\infty\,\mathrm{K\cdot mm^2W^{-1}}$ (TCC= $0\,\mathrm{W\cdot m^{-2}\cdot K^{-1}}$)) .

Fig. 3.15 shows the node temperature distribution after the heating process of 10 s. The heating power is 50 W. Fig. 3.15 a, Fig. 3.15b, and Fig. 3.15c show the temperature distribution with different TCR. With calibrated TCR, the max temperature is around 878 K, which is 57 K higher than thermally perfect condition.

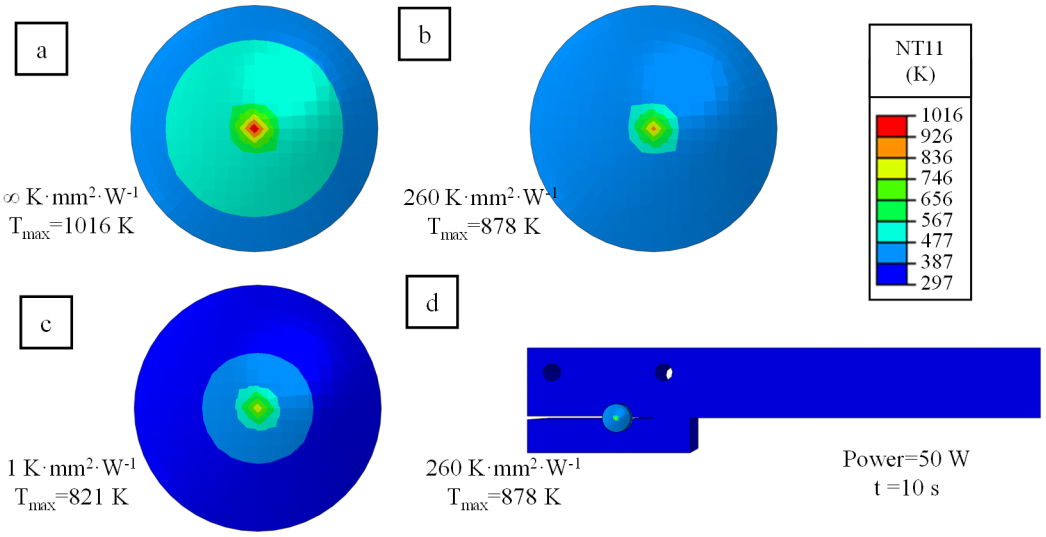

Figure 3.15: The temperature distribution of pin fix in pin holder at the end of the heating process (10s), a) TCR= ∞ K·m^2·W^{-1}, b) & d), TCR=260 K·m^2·W^{-1}, c) 1 K·m^2·W^{-1}.

Fig. 3.16a shows the heating and cooling curve of the average temperature of the center of the spherical pin tip (Fig. 3.16b). The temperature difference between calibrated TCR and thermally perfect TCR is around 35 K (power = 50 W) or 31 K (power = 40 W).

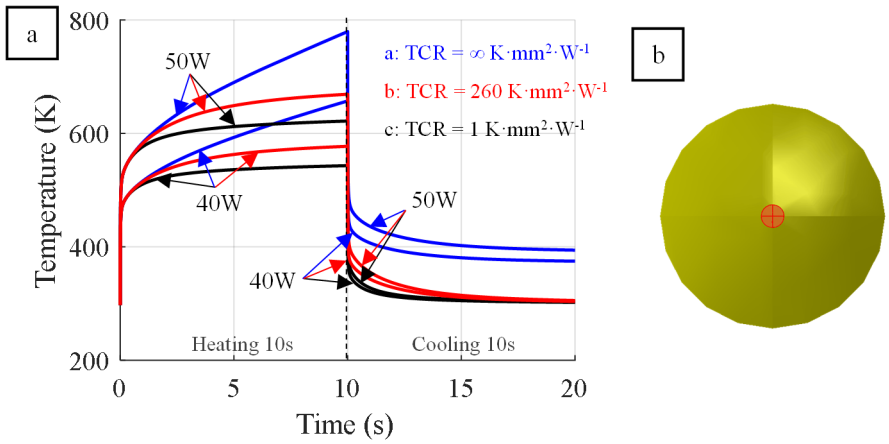

Figure 3.16: Heating and cooling curve of a) average temperature of b) center of pin spherical tip with different TCR

3.4 Summary

This chapter aimed to improve the simulation of the interface temperature distribution. One critical step was identifying the thermal contact resistance (TCR) between a pin and a pin holder involved in an experimental tribometer dedicated to the characterization of such tribological phenomena. The identification of the TCR combined two experimental campaigns in which a laser source was applied either on a pin alone or a pin + its pin holder. The first campaign provided the estimation of the significant amount of heat transmitted to the pin, whereas the second led to identifying the effective TCR. The quantification of both parameters was possible thanks to the comparison between temperatures provided by thermocouples and simulated temperatures provided a 3D heat transfer model. It has been shown that the efficiency ratio of the laser source is 70%, whereas the TCR is around 260 $\mathrm{K \cdot mm^2 \cdot W^{-1}}$. The identification of this actual TCR value contributes to improving the temperature distribution estimation during a pin on the bar open tribological test. It may lead to a better understanding of fundamental phenomena such as friction and wear under extreme conditions.

4 Identification of friction coefficient

Summary

Objective of this chapter

This chapter aims to identify a numerical friction model depended on local tribological parameters at the tool-material interface during a pin-on-bar frictional test under severe contact conditions. The identification process is based on two parts, previous experimental results by Ben Abdelali [7] and numerical simulated local parameters by ALE explicit model. The Response Surface Methodology (RSM) is applied to obtain an optimal response.

4.1 Methodology to identify the friction model

Previous research by Courbon et al. [139] showed that the exponential tendency (asymptote when $V_{ls} \rightarrow \infty$) allows us to propose a similar evolution for adhesive fricion coefficient μ_{adh}, which is shown in Eq. 4.1, where V_{ls} is the local sliding velocity ($m \cdot s^{-1}$). Fig. 4.1 indicates the theoretical curve of the exponential decay friction model. Thus a parameter called 'static friction coefficient μ_s', value at $V_{ls} = 0$, a parameter

called 'kinetic friction coefficient μ_k' , value at $V_{ls} \to \infty$, and a decay constant d_c are introduced. The interest from a numerical point of view is to obtain a continuous function, unlike previous models defined by Zemzemi [11] or Rech [138] in Table 1.4. In this chapter, the exponential decay adhesive friction μ_{adh} model is selected as the form of friction model. The major object is to propose appropriate values of the unknown parameters (μ_s, μ_k, d_c) .

$$\mu_{adh} = \mu_k + (\mu_s - \mu_k) \cdot e^{-d_c \| V_{ls} \|} \tag{4.1}$$

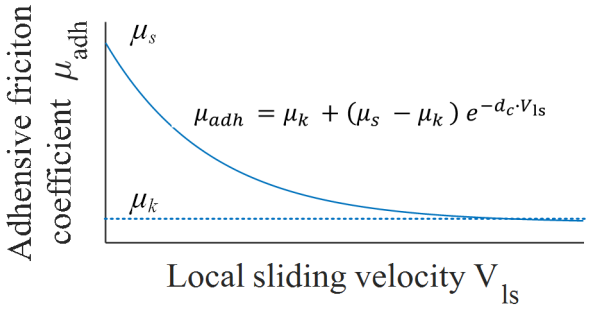

Figure 4.1: Exponential decay friction model.

The methodology to identify the friction coefficient depended on the sliding velocity is presented in Fig. 4.2.

The identification is based on the ALE explicit scratching model in Chapter 2. The heat partition coefficient α_{exp} between the pin and the workpiece could be estimated by equation 2.3 [140]. The thermal contact conductance has been assumed to be $10\,000\,\mathrm{w \cdot m^{-2} \cdot K^{-1}}$all along the contact. The normal force applied to the center of the pin is 500 N.

The experimental apparent friction coefficient $\mu_{app-exp}$ is shown in Tab. 4.1 as well as Fig.4.3 [7], thanks to the tribometer in Fig. 2.1 [84].

Table 4.1: Experimental apparent friction coefficient [7].

V_{macro} $(m \cdot s^{-1})$	1	2	3	4	5
$\mu_{app-exp}$	0.48	0.31	0.24	0.23	0.22

In order to predict the unknown parameters (μ_s, μ_k, d_c) in Eq. 4.1, a series of numerical simulations with various input parameters have been conducted. As Fig. 4.2a shows, The numerical apparent friction coefficient $\mu_{app-num}$ is calculated as the ratio of reaction force along the x direction (F_{R1}) and normal force (F_n).

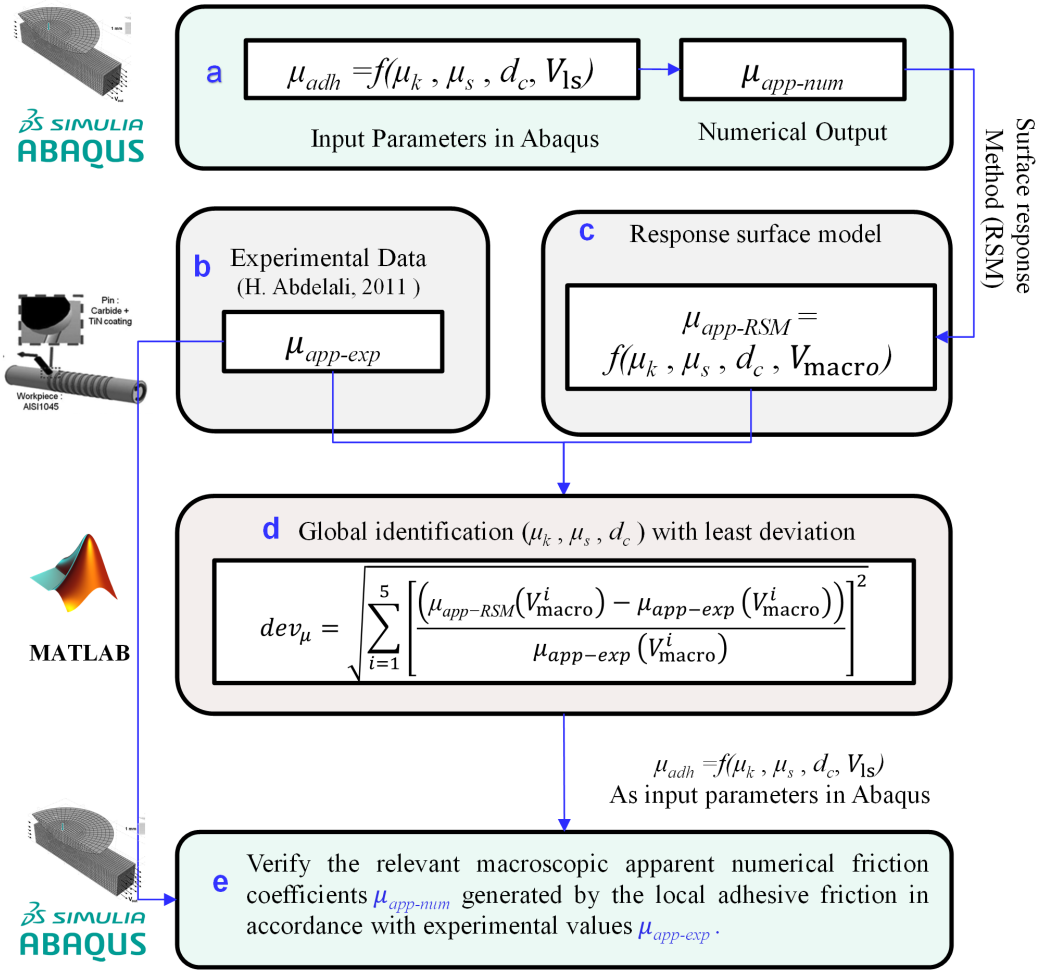

Figure 4.2: Methodology of the identification of friction coefficient.

Thus the response surface models based on the polynomials are fitted with various μ_s, μ_k, d_c, V_{macro} and $\mu_{app-num}$. The calculated result of the response surface model is named as numerical apparent friction coefficient estimated by RSM, $\mu_{app-RSM}$, as Fig. 4.2c shows.

The next step is to find the best solution for the response surface models. As Fig. 4.2d shows, the frictional deviation dev_μ could be estimated by Equ. 4.2. The global optimal solution corresponding to the μ_s, μ_k, d_c with minimal frictional deviation dev_μ.

$$dev_\mu = \sqrt{\sum_{i=1}^{5}\left[\frac{(\mu_{app-num}(V^i_{macro}) - \mu_{app-exp}(V^i_{macro}))}{\mu_{app-exp}(V^i_{macro})}\right]^2} \tag{4.2}$$

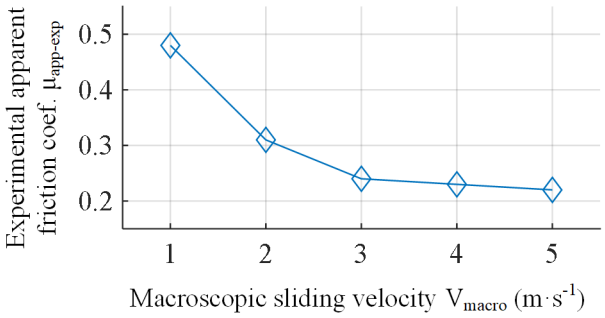

Figure 4.3: Experimental apparent friction coefficient versus macroscopic sliding velocity.

The last step is presented in Fig. 4.2e. The identified input parameters μ_s, μ_k, d_c are substituted into the exponential decay adhesive friction μ_{adh} model. The numerical simulations with identified adhesive friction μ_{adh} model are conducted. The experimental apparent friction coefficient $\mu_{app-exp}$ and numerical apparent friction coefficient $\mu_{app-num}$ are compared.

4.2 Improve stability of the friction coefficient

4.2.1 Contact instability

In previous numerical simulations, the local adhesive friction coefficient μ_{adh} was always considered as a constant value. Even in some cases [11, 138, 139, 7], the adhesive friction coefficient μ_{adh} depends on the macroscopic sliding speed V_{macro} (m·s^{-1}), and the adhesive friction coefficient μ_{adh} is still constant at a specific sliding speed.

For example, if we selected the Equ. 4.3 as the friction model, the adhesive friction coefficient μ_{adh} at a specific microscopic sliding velocity V_{macro} is estimated. Thus the numerical apparent friction coefficients $\mu_{app-num}$ and experimental apparent friction coefficients $\mu_{app-exp}$ are presented in Fig. 4.4.

$$\mu_{adh} = 3.75 \times (60 \cdot V_{macro})^{-0.538} \tag{4.3}$$

Fig. 4.4a shows the numerical apparent friction coefficient $\mu_{app-num}$ versus time on various sliding conditions. Fig. 4.4b compares the numerical and experimental apparent friction coefficient $\mu_{app-num}$ and $\mu_{app-exp}$ on different macroscopic sliding velocities. Where the numerical apparent friction coefficient $\mu_{app-num}$ is the average value of

the last period of 1.5 ms. It indicates that the numerical apparent friction coefficient $\mu_{app-num}$ is slightly higher than the experimental $\mu_{app-exp}$.

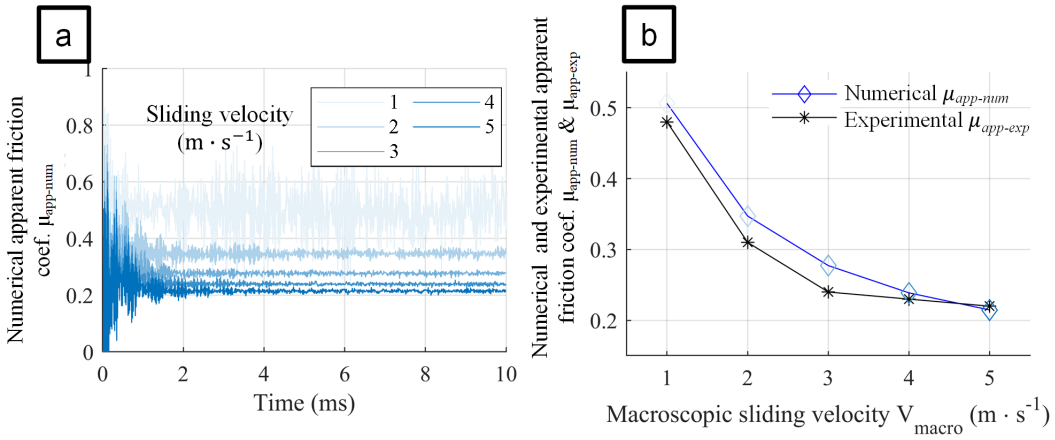

Figure 4.4: (a) Numerical apparent friction coefficient versus time, and (b) comparison of numerical and experimental apparent friction coefficient on different sliding velocities with constant adhesive friction coefficient.

However, when we implement the exponential decay model in the ALE explicit scratch model, the numerical apparent friction coefficient $\mu_{app-num}$ versus time is not as stable as the results based on the constant friction coefficient which is identified by Equ. 4.3, as Fig. 4.5 shows. After a series of attempts, switching the pin into a rigid body and filtering the friction coefficient as a signal effectively improve the stability of the numerical apparent friction coefficient$\mu_{app-num}$.

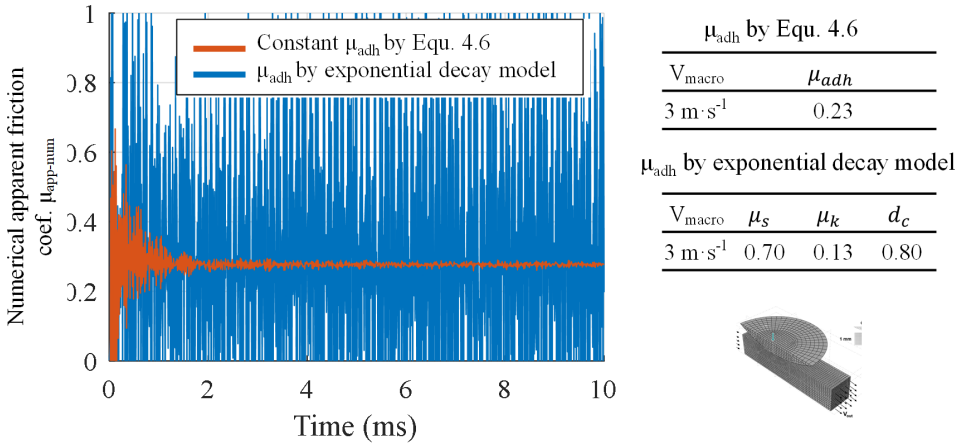

Figure 4.5: Apparent friction coefficient versus time when sliding velocity at 3 $m \cdot s^{-1}$.

4.2.2 Scratching model with rigid pin

In previous simulations, as. Fig. 4.6a shows, only the pin's top layer is defined as a rigid body. The rest of the pin is a flexible part. Thus, to avoid critical instability, the whole pin is selected as a rigid part (Fig. 4.6b).

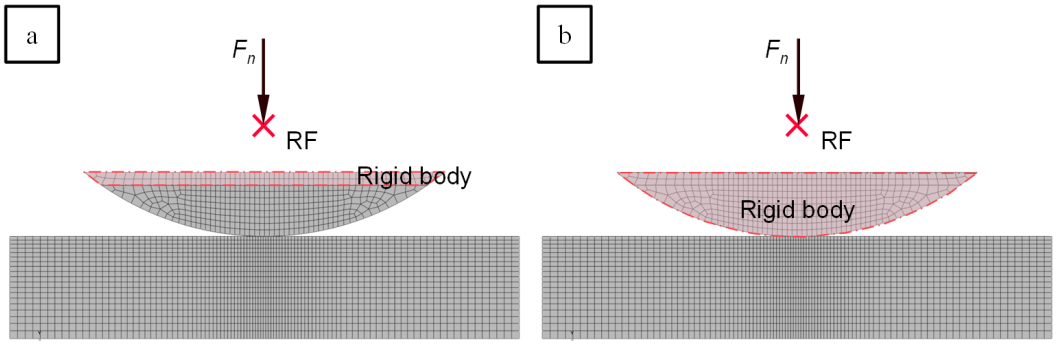

Figure 4.6: Instructions of the rigid part of the pin.

Fig. 4.7 is an example of the apparent friction coefficient versus time with a flexible and a fully rigid pin. The macroscopic sliding velocity V_{macro} is 3 $m \cdot s^{-1}$ and μ_s, μ_k, d_c are 0.70, 0.13 and 0.80, respectively. It is obvious that the rigid pin could increase the contact stabilization at the pin workmaterial interface.

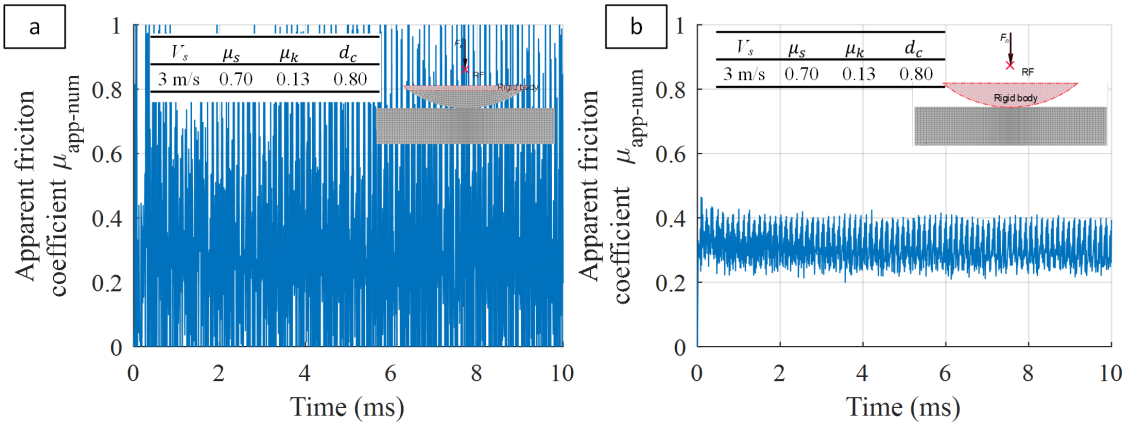

Figure 4.7: Apparent friction coefficient $\mu_{app-num}$ versus time with with a flexible and a fully rigid pin.

4.2.3 Filtering the friction coefficient

Therefore, the signal processing procedure is applied to reduce system error and appropriately estimate the $\mu_{app-num}$. For the ALE explicit model, the macroscopic sliding velocity V_{macro} is from 1 m/s to 5m/s. The normal force F_n applied on the pin is 500 N. The simulation period is 10 ms. The step increment δt is 0.01 ms. Thus, the frequency equals 100 kHz, which equals 1/ δt.

The signal processing procedure is based on MATLAB Signal Processing Toolbox. The high frequency parts of the friction coefficient which exceed the passband frequency (Fpass) are removed by the lowpass filter, where Fpass = 10 kHz. Thus, the original and filtered numerical apparent friction coefficient $\mu_{app-num}$ could be compared. Fig. 4.8 shows that the original and filtered apparent friction coefficient versus time with different sliding velocities. The macroscopic sliding velocity V_{macro} is 1 $m \cdot s^{-1}$ and 3 $m \cdot s^{-1}$. Input parameters μ_s, μ_k, d_c are 0.70, 0.13 and 0.80, respectively. Significantly, the filtered numerical apparent friction coefficient $\mu_{app-num}$ is much more stable than the original value, while a certain small amount of instability still exists.

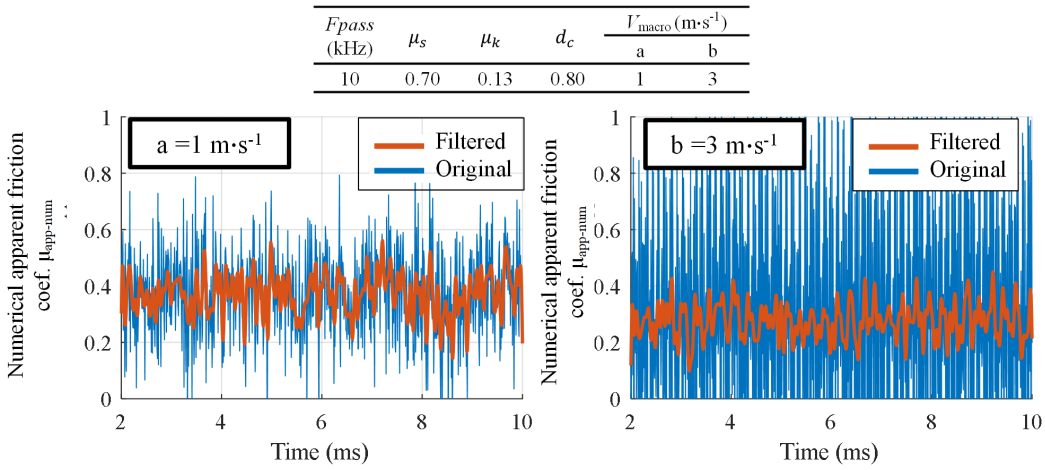

Figure 4.8: Original and filtered apparent friction coefficient versus time with different sliding velocity (a) 1 $m \cdot s^{-1}$ and (b) 3 $m \cdot s^{-1}$.

4.3 Identification of the friction model

4.3.1 Numerical simulation

In order to predict the unknown parameters (μ_s, μ_k, d_c) in Eq. 4.1, a series of numerical simulations with various input parameters have been conducted. The range of these

parameters is shown in Table 4.2. The CCD is the central composite design, which is a proper experimental design in response surface methodology. The full set of data is a control group, which consists of many previous simulation results.

Table 4.2: Range of different unknown parameters.

factor	units	CCD		full set of data		response
		low level	high level	low level	high level	
μ_s		0.6	1	0.5	1	$\mu_{app-num}$
μ_k		0.05	0.15	0.05	0.16	
d_c		0.6	1	0.45	1	
V_{macro}	$m \cdot s^{-1}$	0.5	4.5	1	5	
test count		25		222		

4.3.2 Identification based on the filtered friction coefficient

Based on these numerical simulations, the numerical macroscopic friction coefficient $\mu_{app-num}$ is provided. The scatter of $\mu_{app-num}$, which is dependent on macroscopic sliding velocity V_{macro} and decay constant d_c is shown in Fig. 4.9. Thus the Response Surface Method (RSM) is employed based on commercial code MATLAB. RSM method is a representative method for generating meta-models. The original model is evaluated at multiple sample points, and the meta-model is constructed usually as a function [156].

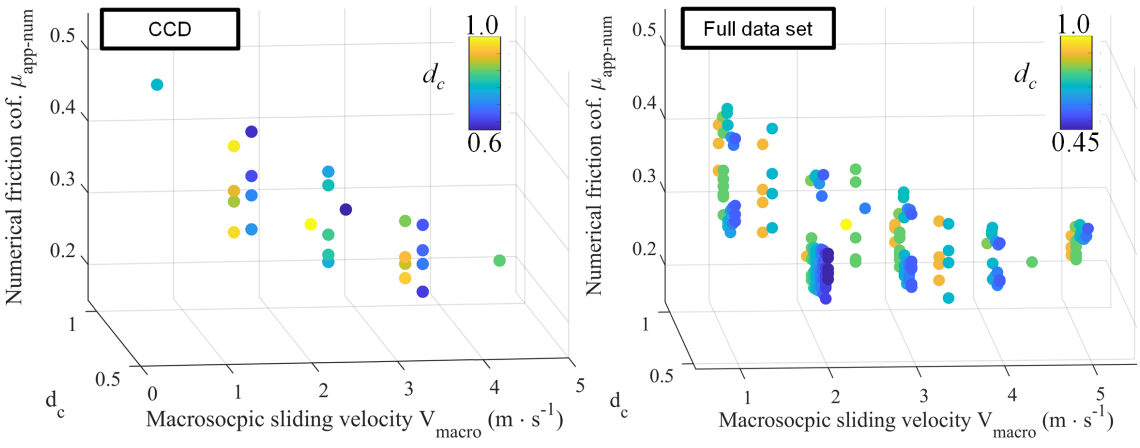

Figure 4.9: Scatter of the numerical apparent friction coefficient ($\mu_{app-num}$) depended on macroscopic sliding velocity V_{macro} and decay constant d_c.

Tab. 4.3 summarized the deviation of the original $\mu_{app-num}$ and the difference between original and filtered $\mu_{app-num}$. The original and filtered numerical apparent

friction coefficient $\mu_{app-num}$ is the average value of the last period of 1.5 ms. The standard deviation (STD) is estimated based on the original numerical apparent friction coefficient $\mu_{app-num}$. The Diff is the difference between the original and filtered numerical apparent friction coefficient $\mu_{app-num}$ with the passband frequency at 10 kHz. It indicates that there is no significant difference between the original and filtered $\mu_{app-num}$.

Table 4.3: Standard deviation of the original numerical apparent friction coefficient and the difference between original and filtered.

	$\mu_{app-num}$				
	STD			Diff	
	minima	median	maxima	minima	maxima
CCD	0.15	0.28	0.72	0.00	0.00
Full set of data	0.11	0.33	1.32	0.00	0.01

In addition, to better understand the standard deviation STD in Tab. 4.3, Fig. 4.10 presents the standard deviation STD corresponding to the numerical apparent friction coefficient $\mu_{app-num}$ versus time.

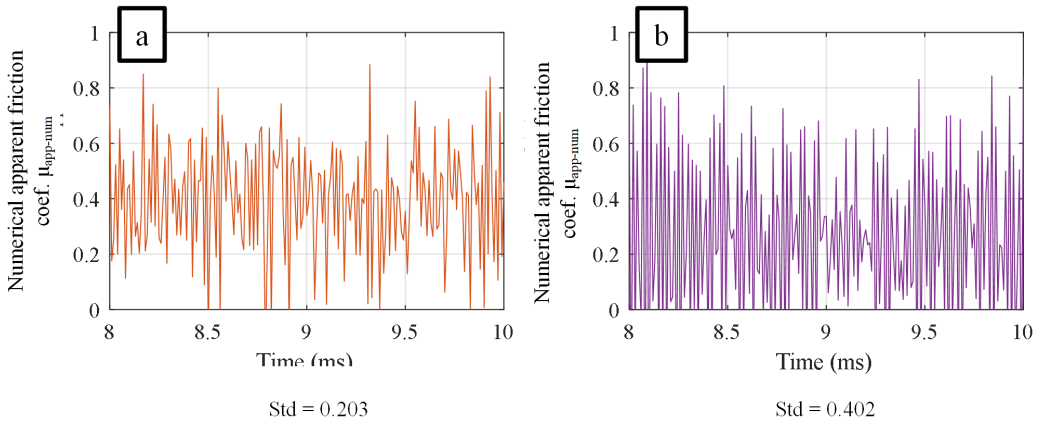

Figure 4.10: The apparent friction coefficient versus time with different standard deviation: (a) STD=0.203 and (b) STD =0.402.

Thus, based on the filtered $\mu_{app-num}$ with a flexible pin, these response surface models are fitted as Eq. 4.4 and Eq. 4.5. Eq. 4.4 is a reduced cubic model of CCD, and Eq. 4.5 is a quartic model of full set of data (control group). These equations can be implemented to identify the relationship between the unknown parameters (μ_s, μ_k, d_c) with known parameters (V_{macro} with $\mu_{app-num}$).

$$\begin{aligned}\mu_{app-RSM}\big|_{\text{CDD}} = &-12.2+26.4\cdot\mu_s+27.8\cdot\mu_k+3.8\cdot d_c+1.5\cdot V_{macro}-47.4\cdot\mu_s\cdot\mu_k\\ &-6.3\cdot\mu_s\cdot d_c-4.1\cdot\mu_s\cdot V_{macro}-16.9\cdot\mu_k\cdot d_c-0.2\cdot\mu_k\cdot V_{macro}+\\ &0.5\cdot d_c\cdot V_{macro}-13.5\cdot\mu_s^2+14.5\cdot\mu_k^2-0.3\cdot d_c^2+21.3\cdot\mu_s\cdot\mu_k\cdot d_c\\ &+0.4\cdot\mu_s\cdot\mu_k\cdot V_{macro}-0.5\cdot\mu_s\cdot d_c\cdot V_{macro}-0.2\cdot\mu_k\cdot d_c\cdot V_{macro}\\ &+17.1\cdot\mu_s^2\cdot\mu_k+2.3\cdot\mu_s^2\cdot d_c+2.5\cdot\mu_s^2\cdot V_{macro}-16.8\cdot\mu_s\cdot\mu_k^2\end{aligned} \tag{4.4}$$

$$\begin{aligned}\mu_{app-RSM}\big|_{\text{full set}} = =&39.6-38\cdot\mu_s-594.7\cdot\mu_k-59\cdot d_c-6.7\cdot V_{macro}+307.8\cdot\mu_s\cdot\mu_k+60.7\cdot\mu_s\cdot\\ &d_c+20.1\cdot\mu_s\cdot V_{macro}+743.7\cdot\mu_k\cdot d_c+96.2\cdot\mu_k\cdot V_{macro}-9.6\cdot d_c\cdot V_{macro}-\\ &14.6\cdot\mu_s^2+3303.7\cdot\mu_k^2+48\cdot d_c^2+0.4\cdot V_{macro}^2-261.5\cdot\mu_s\cdot\mu_k\cdot d_c-160.6\\ &\mu_s\cdot\mu_k\cdot V_{macro}-10.3\cdot\mu_s\cdot d_c\cdot V_{macro}+46.4\cdot\mu_k\cdot d_c\cdot V_{macro}+184\cdot\mu_s^2\cdot\mu_k\\ &-41.4\cdot\mu_s^2\cdot d_c-10.5\cdot\mu_s^2\cdot V_{macro}-1028.6\cdot\mu_s\cdot\mu_k^2-6.9\cdot\mu_s\cdot d_c^2+0.3\cdot\mu_s\\ &V_{macro}^2-2617.8\cdot\mu_k^2\cdot d_c-515\cdot\mu_k^2\cdot V_{macro}-548.2\cdot\mu_k\cdot d_c^2+1\cdot\mu_k\cdot V_{macro}^2\\ &+15.2\cdot d_c^2\cdot V_{macro}-0.4\cdot d_c\cdot V_{macro}^2+31.8\cdot\mu_s^3-7627.4\cdot\mu_k^3-27.8\cdot d_c^3\\ &-0.1\cdot V_{macro}^3+13\cdot\mu_s\cdot\mu_k\cdot d_c\cdot V_{macro}+8.4\cdot\mu_s^2\cdot\mu_k^2+317.5\cdot\mu_s^2\cdot\mu_k\cdot d_c\\ &+65.1\cdot\mu_s^2\cdot\mu_k\cdot V_{macro}-106.1\cdot\mu_s^2\cdot d_c^2-5\cdot\mu_s^2\cdot d_c\cdot V_{macro}-0.3\cdot\mu_s^2\cdot V_{macro}^2\\ &+65.1\cdot\mu_s^2\cdot\mu_k\cdot V_{macro}-106.1\cdot\mu_s^2\cdot d_c^2-5\cdot\mu_s^2\cdot d_c\cdot V_{macro}-0.3\cdot\mu_s^2\cdot V_{macro}^2\\ &+184.9\cdot\mu_s\cdot\mu_k^2\cdot d_c+326.4\cdot\mu_s\cdot\mu_k^2\cdot V_{macro}-191.3\cdot\mu_s\cdot\mu_k\cdot d_c^2-4.1\cdot\mu_s\cdot\mu_k\\ &V_{macro}^2+9.5\cdot\mu_s\cdot d_c^2\cdot V_{macro}+0.4\mu_s\cdot d_c\cdot V_{macro}^2+1070.6\cdot\mu_k^2\cdot d_c^2-30.1\cdot\mu_k^2\\ &d_c\cdot V_{macro}-3.6\cdot\mu_k^2\cdot V_{macro}^2-40.6\cdot\mu_k\cdot d_c^2\cdot V_{macro}+2.6\cdot\mu_k\cdot d_c\cdot V_{macro}^2-\\ &d_c\cdot V_{macro}-3.6\cdot\mu_k^2\cdot V_{macro}^2-40.6\cdot\mu_k\cdot d_c^2\cdot V_{macro}+2.6\cdot\mu_k\cdot d_c\cdot V_{macro}^2-\\ &0.1\cdot d_c^2\cdot V_{macro}^2-269.6\cdot\mu_s^3\cdot\mu_k+77.7\cdot\mu_s^3\cdot d_c+3.3\cdot\mu_s^3\cdot V_{macro}+54.8\cdot\mu_s\\ &\cdot\mu_k^3+74.2\cdot\mu_s\cdot d_c^3+2805.8\cdot\mu_k^3 d_c+930.8\cdot\mu_k^3\cdot V_{macro}+239.8\cdot\mu_k\cdot d_c^3+0.1\\ &\mu_k\cdot V_{macro}^3-7.4\cdot d_c^3\cdot V_{macro}-22.3\cdot\mu_s^4+6951.9\cdot\mu_k^4-12.9\cdot d_c^4\end{aligned} \tag{4.5}$$

Tab. 4.4 presents the ANOVA for surface response models. The F-value of both models implies the models are significant.

Table 4.4: ANOVA for the surface response models.

model	Sum of Squares	F-value	p-value
CCD	0.1244	23.63	0.0001
Full set	0.6451	65.16	0.0001

The next step is to find the optimal global solution for the unknown parameters (μ_s, μ_k, d_c) with the surface response models. Based on the range of unknown parameters

in Tab. 4.2, a large 3 dimensional matrix with a small interval of μ_s, μ_k, d_c is created. The frictional deviation dev_μ is estimated with each combination of μ_s, μ_k, d_c in the 3 dimensional matrix. The dev_μ is calculated by Equ. 4.2 in MATLAB. Thus all the possible solutions of the surface response models corresponding to the dev_μ are presented. The global optimal solution of μ_s, μ_k, d_c corresponds to the minimal dev_μ. Equ. 4.6 and Equ. 4.7 are the calibrated response surface model with global optimal solutions of μ_s, μ_k, d_c of CCD design and the full set of data (control group), respectively.

$$\mu_{adh}\big|_{\text{CCD}} = 0.08 + (0.84 - 0.08) \cdot e^{-0.79\|V_{ls}\|} \tag{4.6}$$

$$\mu_{adh}\big|_{\text{full set}} = 0.06 + (0.84 - 0.06) \cdot e^{-0.69\|V_{ls}\|} \tag{4.7}$$

Based on the global optimal solutions of μ_s, μ_k, d_c of the CCD and full set of data design (control group), the comparison between the experimental $\mu_{app-exp}$ and numerical $\mu_{app-num}$ apparent friction coeffcient estimated by RSM are shown in Fig. 4.11. Futhermore, the numerical apparent friction coefficient based on the Equ. 4.3 is presented as well. The corresponding data are presented in Tab. 4.5. The global optimal solution of the μ_s of both models is around 0.84. The identified d_c of CCD is higher than full data set, thus $\mu_{app-RSM}$ (the apparent friction coefficient estimated by RSM) of CCD at 1 $m \cdot s^{-1}$ is lower than the full data set.

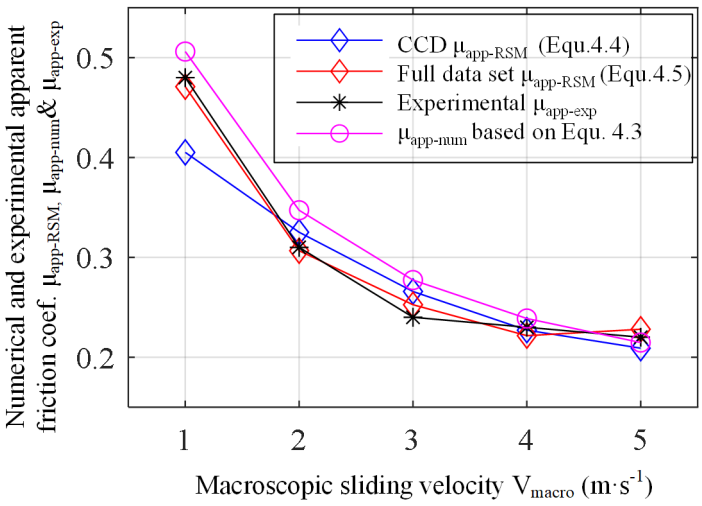

Figure 4.11: Comparison between the experimental and numerical apparent friction coefficient estimated by RSM.

The last step is to verify these friction models in the ALE scratching numerical model by ABAQUS. As Fig. 4.12 shows, the $\mu_{app-num}$ of data set group does not fit as well

Table 4.5: Comparison of the experimental and numerical apparent friction coefficient estimated by RSM.

	μ_s	μ_k	d_c	dev_μ	Apparent friction coefficient (RSM)				
					v=1 $m \cdot s^{-1}$	v=2 $m \cdot s^{-1}$	v=3 $m \cdot s^{-1}$	v=4 $m \cdot s^{-1}$	v=5 $m \cdot s^{-1}$
CCD	0.84	0.08	0.79	0.20	0.41	0.33	0.27	0.23	0.21
Full data set	0.84	0.06	0.69	0.06	0.47	0.31	0.25	0.22	0.23
Experimental	/	/	/	/	0.48	0.31	0.24	0.23	0.22
$\mu_{app-num}$ based on Equ. 4.6	/	/	/	/	0.51	0.35	0.28	0.24	0.21

as the $\mu_{app-RSM}$ in Fig. 4.11. Furthermore, the numerical apparent friction coefficient $\mu_{app-num}$ and $\mu_{app-RSM}$ of central composite design (CCD) has the same tend. While there is a significant difference between the numerical apparent friction coefficient $\mu_{app-num}$ and $\mu_{app-RSM}$ of the full data set. One possible explanation is that it is a numerical calculation problem. Despite we get the minimal dev_μ, the solution is an extraneous solution.

For the CCD model, the $\mu_{app-num}$ fits the experimental results well except 1 $m \cdot s^{-1}$. This might occur due to the own characteristic of the CCD. Despite the range of sliding velocity V_{macro} in CCD is from 0.5 to 5.5 $m \cdot s^{-1}$, most of the simulations are in the range 1.5 to 3.5 $m \cdot s^{-1}$. Therefore the $\mu_{app-num}$ based on CCD friction model fits the $\mu_{app-exp}$ well except for low sliding speed.

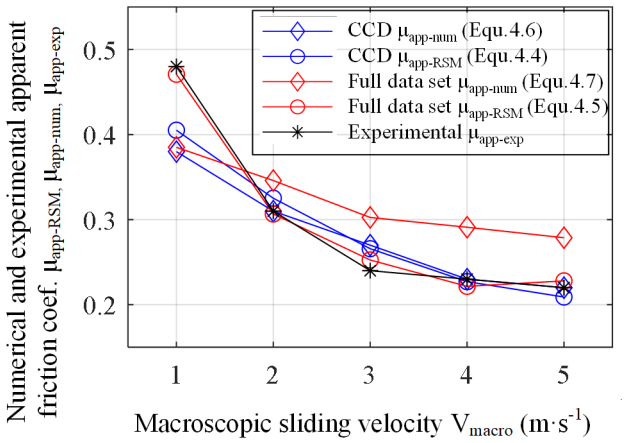

Figure 4.12: Comparison between the experimental and numerical apparent friction coefficient extracted from ABAQUS output.

Table 4.6: Comparison of the experimental and numerical apparent friction coefficient.

	μ_s	μ_k	d_c	dev_μ	Apparent friction coefficient				
					v=1 $m \cdot s^{-1}$	v=2 $m \cdot s^{-1}$	v=3 $m \cdot s^{-1}$	v=4 $m \cdot s^{-1}$	v=5 $m \cdot s^{-1}$
CCD $\mu_{app-num}$	0.84	0.08	0.79	0.20	0.38	0.31	0.27	0.23	0.22
CCD $\mu_{app-RSM}$	0.84	0.08	0.79	0.20	0.41	0.33	0.27	0.23	0.21
Full data set $\mu_{app-num}$	0.84	0.06	0.69	0.06	0.39	0.35	0.30	0.29	0.28
Full data set $\mu_{app-RSM}$	0.84	0.06	0.69	0.06	0.47	0.31	0.25	0.22	0.23
Experimental	/	/	/	/	0.48	0.31	0.24	0.23	0.22
$\mu_{app-num}$ based on Equ. 4.6	/	/	/	/	0.51	0.35	0.28	0.24	0.21

4.4 Summary

In this section, the response surface method (RSM) is applied to identify a general friction model for various sliding velocities. Central composite designs (CCD) are selected as a helpful RSM design method and the full data set as a control group. The adhesive friction model μ_{adh} is select in the form of an exponential decay model. During the identification process, the instability of the friction coefficient is filtered by signal processing. The data processing indicates that there is no significant difference between filtered and original average apparent friction coefficient ($\mu_{app-num}$). Furthermore, the rigid pin can increase contact stabilization.

Based on the filtered numerical apparent friction coefficient $\mu_{app-num}$, the RSM models are fitted by Matlab. Thus the global optimal solutions of the RSM models are identified by calculated the frictional deviation. The RSM models consist of the CCD model and the full data set (control group) model. The corresponding adhesive frictional exponential decay model is presented as well.

The numerical apparent friction coefficient $\mu_{app-RSM}$ of full data set (control group) fits the $\mu_{app-exp}$ well. While in the verification process, the $\mu_{app-num}$ of full data set is varying from the $\mu_{app-exp}$.

The identified CCD model (Equ. 4.6) fits the experimental result well except at 1 $m \cdot s^{-1}$. Compare with Equ. 4.3, The CCD model provides reliable adhesive friction coefficient μ_{adh} and no need to consider one specific adhesive friction coefficient μ_{adh} at a specific macroscopic sliding velocity V_{macro}. However, the assumption of the exponential decay model is only dependent on the local sliding velocity V_{ls}, the influence of contact pressure and temperature is ignored. This might limit the application range of the CCD model.

Conclusion

This thesis aimed at generally improving the numerical simulation of a sliding contact under extreme contact conditions and proposing an innovative methodology to better identify friction models.

First of all, a numerical modeling strategy is presented to estimate the 3D temperature distribution at the interface during a pin-on-bar frictional test under severe contact conditions. Two 3D Finite Element (FE) models based on commercial code ABAQUS have been established to simulate local thermo-mechanical loading. The first explicit scratch model indicated that the total power transmitted to the friction pin is almost constant after 9 ms of sliding. Thus it is possible to apply the surface heat flux distribution as a boundary condition in a long time scale model. The second implicit heat transfer model showed that it took 20 s to reach the thermal equilibrium with the heat input extracted from the scratch model. The dedicated methodology could simulate the temperature within such contact properly.

The sensitivity analysis of the implicit heat transfer model shows that the TCR between pin & pin holder is the critical boundary condition. It affects not only the final temperature reached by the pin but also the heating rate by controlling the dissipation rate to the pin holder. Thus the thermal contact resistance (TCR) between a pin and a pin holder was identified by an experimental tribometer dedicated to the characterization of such tribological phenomena.

The identification of the TCR combined two experimental campaigns in which a laser source was applied either on a pin alone or a pin + its pin holder. The first campaign provided the estimation of the significant amount of heat transmitted to the pin, whereas the second led to identifying the effective TCR. The quantification of both parameters was possible thanks to the comparison between temperatures provided by thermocouples and simulated temperatures provided a 3D heat transfer model. It has been shown that the efficiency ratio of the laser source is 70%, whereas the TCR is around $260\,\mathrm{K}\cdot\mathrm{mm}^2\cdot\mathrm{W}^{-1}$. The identification of this actual TCR value contributes to improving the temperature distribution estimation during a pin on the bar open tribological test.

Furthermore, a general friction model for various sliding velocities was identified by the response surface method (RSM) based on the explicit scratch model. The adhesive friction model μ_{adh} is selected in the form of an exponential decay model. The

RSM models are fitted by Matlab based on the numerical apparent friction coefficient $\mu_{app-num}$. Thus the global optimal solutions of the RSM models are identified by calculated the frictional deviation. The RSM models consist of the CCD model and the full data set (control group) model. The corresponding adhesive frictional exponential decay model is presented as well. The identified input parameters are substituted into the exponential decay adhesive friction μ_{adh} model to verify the relevant macroscopic apparent numerical friction coefficients $\mu_{app-num}$ generated by the local adhesive friction in accordance with experimental values $\mu_{app-exp}$. The identified CCD model fits the experimental result well except at 1 $m \cdot s^{-1}$. The CCD model provides reliable adhesive friction coefficient μ_{adh} and no need to consider one specific adhesive friction coefficient μ_{adh} at a specific macroscopic sliding velocity V_{macro}.

The improvement of numerical simulation of a sliding contact may lead to a better understanding of fundamental phenomena such as friction under extreme conditions. The methodology to identify a general friction model for various sliding velocities may be helpful and effective for the description of frictional behavior at the interface. Those improvements could be effective to predict the wear, tool's failure in the future.

Bibliography

[1] H. P. Jost. "Tribology - Origin and future". In: *Wear* 136.1 (Feb. 1990), pp. 1–17 (cit. on p. 1).

[2] K. Holmberg and A. Erdemir. "Influence of tribology on global energy consumption, costs and emissions". In: *Friction* 5.3 (2017), pp. 263–284 (cit. on p. 1).

[3] D. Mourtzis, M. Doukas, and D. Bernidaki. "Simulation in manufacturing: Review and challenges". In: *Procedia Cirp* 25 (2014), pp. 213–229 (cit. on p. 6).

[4] M. P. Groover. *Fundamentals of modern manufacturing: materials, processes, and systems*. John Wiley & Sons, 2020 (cit. on pp. 6, 7, 13).

[5] B. Shi, H. Attia, and N. Tounsi. "Identification of material constitutive laws for machining—part I: an analytical model describing the stress, strain, strain rate, and temperature fields in the primary shear zone in orthogonal metal cutting". In: *Journal of Manufacturing Science and Engineering* 132.5 (2010) (cit. on p. 6).

[6] M. C. Shaw and J. Cookson. *Metal cutting principles*. Vol. 2. Oxford university press New York, 2005 (cit. on p. 8).

[7] H. B. Abdelali, C. Courbon, J. Rech, et al. "Identification of a friction model at the tool-chip-workpiece interface in dry machining of a AISI 1045 steel with a TiN coated carbide tool". In: *Journal of Tribology* 133.4 (Oct. 2011), pp. 1–11 (cit. on pp. 8, 21, 28, 43–46, 51, 91, 92, 94).

[8] N. N. Zorev. *Metal cutting mechanics*. 1966 (cit. on p. 7).

[9] P. L. Menezes, S. P. Ingole, M. Nosonovsky, et al. *Tribology for scientists and engineers: From basics to advanced concepts*. Vol. 9781461419. 2013, pp. 1–948 (cit. on pp. 7, 11, 24).

[10] C. Bonnet, F. Valiorgue, J. Rech, et al. "Identification of a friction model-Application to the context of dry cutting of an AISI 316L austenitic stainless steel with a TiN coated carbide tool". In: *International Journal of Machine Tools and Manufacture* 48.11 (Sept. 2008), pp. 1211–1223 (cit. on pp. 9, 45, 47, 48).

[11] F. Zemzemi, J. Rech, W. Ben Salem, et al. "Identification of a friction model at tool/chip/workpiece interfaces in dry machining of AISI4142 treated steels". In: *Journal of Materials Processing Technology* 209.8 (Apr. 2009), pp. 3978–3990 (cit. on pp. 9, 24, 43, 44, 51, 92, 94).

[12] T. P. Kumar, N. Mahalingesh, S. Prajwal, et al. "Estimation of solid-solid contact conductance based on inverse solution". In: *Proceedings of the 24 th National and 2 nd International ISHMT-ASTFE Heat and Mass Transfer Conference (IHMTC-2017)*. Begel House Inc. 2017 (cit. on p. 9).

[13] L. S. Fletcher. "Recent Developments in Contact Conductance Heat Transfer". In: *Journal of Heat Transfer* 110.4b (Nov. 1988), pp. 1059–1070 (cit. on p. 9).

[14] L. Fletcher. "Recent developments in contact conductance heat transfer". In: (1988) (cit. on p. 10).

[15] G. Zavarise, P. Wriggers, E. Stein, et al. "Real contact mechanisms and finite element formulation—a coupled thermomechanical approach". In: *International Journal for numerical methods in Engineering* 35.4 (1992), pp. 767–785 (cit. on p. 9).

[16] J. Meseguer, I. Pérez-Grande, and A. Sanz-Andrés. "10 - Mechanical interfaces". In: *Spacecraft Thermal Control*. Ed. by J. Meseguer, I. Pérez-Grande, and A. Sanz-Andrés. Woodhead Publishing, 2012, pp. 157–173 (cit. on p. 9).

[17] M. Sakkaki, F. Sadegh Moghanlou, M. Vajdi, et al. "The effect of thermal contact resistance on the temperature distribution in a WC made cutting tool". In: *Ceramics International* 45.17, Part A (2019), pp. 22196–22202 (cit. on p. 10).

[18] C. Courbon, T. Mabrouki, J. Rech, et al. "On the existence of a thermal contact resistance at the tool-chip interface in dry cutting of AISI 1045: Formation mechanisms and influence on the cutting process". In: *Applied Thermal Engineering* 50.1 (2013), pp. 1311–1325 (cit. on pp. 10, 41, 42).

[19] A. Mondelin, F. Valiorgue, E. Feulvarch, et al. "Calibration of the insert/tool holder thermal contact resistance in stationary 3D turning". In: *Applied Thermal Engineering* 55.1-2 (2013), pp. 17–25 (cit. on pp. 10, 51).

[20] F. Klocke and T. Krieg. "Coated tools for metal cutting–features and applications". In: *CIRP Annals* 48.2 (1999), pp. 515–525 (cit. on p. 10).

[21] J. Outeiro, D. Umbrello, and R. M'saoubi. "Experimental and numerical modelling of the residual stresses induced in orthogonal cutting of AISI 316L steel". In: *International Journal of Machine Tools and Manufacture* 46.14 (2006), pp. 1786–1794 (cit. on p. 10).

[22] Y.-C. Yen, J. Söhner, B. Lilly, et al. "Estimation of tool wear in orthogonal cutting using the finite element analysis". In: *Journal of materials processing technology* 146.1 (2004), pp. 82–91 (cit. on p. 10).

[23] B. Bourouga, E. Guillot, B. Garnier, et al. "Experimental study of thermal sliding contact parameters at interface seat of large strains". In: *International Journal of Material Forming* 3.1 (2010), pp. 821–824 (cit. on pp. 10, 57, 70).

[24] A. Kusiak, J.-L. Battaglia, and J. Rech. "Tool coatings influence on the heat transfer in the tool during machining". In: *Surface and Coatings Technology* 195.1 (2005), pp. 29–40 (cit. on p. 10).

[25] M. Attia and L. Kops. "Nonlinear thermoelastic behavior of structural joints—solution to a missing link for prediction of thermal deformation of machine tools". In: (1979) (cit. on p. 10).

[26] M. Attia and L. Kops. "Importance of contact pressure distribution on heat transfer in structural joints of machine tools". In: (1980) (cit. on p. 10).

[27] M. Attia and L. Kops. "System approach to the thermal behavior and deformation of machine tool structures in response to the effect of fixed joints". In: (1981) (cit. on p. 10).

[28] R. W. Maruda, G. M. Krolczyk, P. Nieslony, et al. "The influence of the cooling conditions on the cutting tool wear and the chip formation mechanism". In: *Journal of Manufacturing processes* 24 (2016), pp. 107–115 (cit. on p. 10).

[29] S. N. Melkote, W. Grzesik, J. Outeiro, et al. "Advances in material and friction data for modelling of metal machining". In: *CIRP Annals* (2017) (cit. on pp. 10, 11).

[30] D. Buryta, R. Sowerby, and I. Yellowley. "Stress distributions on the rake face during orthogonal machining". In: *International Journal of Machine Tools and Manufacture* 34.5 (1994), pp. 721–739 (cit. on p. 11).

[31] H. T. Yang, M. Heinstein, and J.-M. Shih. "Adaptive 2D finite element simulation of metal forming processes". In: *International journal for numerical methods in engineering* 28.6 (1989), pp. 1409–1428 (cit. on pp. 11, 12, 40).

[32] T. Marusich and M. Ortiz. "Modelling and simulation of high-speed machining". In: *International Journal for Numerical Methods in Engineering* 38.21 (1995), pp. 3675–3694 (cit. on pp. 11, 12).

[33] K. Lange. "Handbook of metal forming". In: *McGraw-Hill Book Company, 1985,* (1985), p. 1216 (cit. on p. 11).

[34] G. E. Dieter and D. J. Bacon. *Mechanical metallurgy*. Vol. 3. McGraw-hill New York, 1986 (cit. on p. 12).

[35] N. Bay. "The state of the art in cold forging lubrication". In: *Journal of Materials Processing Technology* 46.1-2 (1994), pp. 19–40 (cit. on p. 13).

[36] M. P. Pereira, W. Yan, and B. F. Rolfe. "Contact pressure evolution and its relation to wear in sheet metal forming". In: *Wear* 265.11-12 (2008), pp. 1687–1699 (cit. on p. 13).

[37] P. Groche, C. Müller, J. Stahlmann, et al. "Mechanical conditions in bulk metal forming tribometers—Part one". In: *Tribology International* 62 (2013), pp. 223–231 (cit. on pp. 13, 14, 29–31).

[38] A. Buschhausen, K. Weinmann, J. Y. Lee, et al. "Evaluation of lubrication and friction in cold forging using a double backward-extrusion process". In: *Journal of materials processing technology* 33.1-2 (1992), pp. 95–108 (cit. on p. 13).

[39] H. Liu, W. Liu, J. Bao, et al. "Numerical and experimental investigation into hot forming of ultra high strength steel sheet". In: *Journal of Materials Engineering and Performance* 20.1 (2011), pp. 1–10 (cit. on pp. 14, 15).

[40] Z. Hou, J. Sheikh-Ahmad, F. Jarrar, et al. "Residual stresses in dissimilar friction stir welding of AA2024 and AZ31: experimental and numerical study". In: *Journal of Manufacturing Science and Engineering* 140.5 (2018) (cit. on p. 14).

[41] H. Schmidt, J. Hattel, and J. Wert. "An analytical model for the heat generation in friction stir welding". In: *Modelling and simulation in materials science and engineering* 12.1 (2003), p. 143 (cit. on pp. 14, 15).

[42] S. Chen, Y. Zhou, J. Xue, et al. "High rotation speed friction stir welding for 2014 aluminum alloy thin sheets". In: *Journal of Materials Engineering and Performance* 26.3 (2017), pp. 1337–1345 (cit. on p. 15).

[43] Z. Zhang, B. Xiao, and Z. Ma. "Enhancing mechanical properties of friction stir welded 2219Al-T6 joints at high welding speed through water cooling and post-welding artificial ageing". In: *Materials Characterization* 106 (2015), pp. 255–265 (cit. on p. 15).

[44] P. Li, G. You, H. Wen, et al. "Friction stir welding between the high-pressure die casting of AZ91 magnesium alloy and A383 aluminum alloy". In: *Journal of Materials Processing Technology* 264 (2019), pp. 55–63 (cit. on p. 15).

[45] D. Kim, H. Badarinarayan, J. H. Kim, et al. "Numerical simulation of friction stir butt welding process for AA5083-H18 sheets". In: *European Journal of Mechanics-A/Solids* 29.2 (2010), pp. 204–215 (cit. on p. 16).

[46] G. Buffa, J. Hua, R. Shivpuri, et al. "A continuum based fem model for friction stir welding—model development". In: *Materials Science and Engineering: A* 419.1-2 (2006), pp. 389–396 (cit. on p. 16).

[47] G. Buffa, J. Hua, R. Shivpuri, et al. "Design of the friction stir welding tool using the continuum based FEM model". In: *Materials Science and Engineering: A* 419.1-2 (2006), pp. 381–388 (cit. on p. 16).

[48] H. Schmidt and J. Hattel. "A local model for the thermomechanical conditions in friction stir welding". In: *Modelling and simulation in materials science and engineering* 13.1 (2004), p. 77 (cit. on p. 16).

[49] W. Li, R. Jiang, Z. Zhang, et al. "Effect of Rotation Speed to Welding Speed Ratio on Microstructure and Mechanical Behavior of Friction Stir Welded Aluminum–L ithium Alloy Joints". In: *Advanced Engineering Materials* 15.11 (2013), pp. 1051–1058 (cit. on p. 17).

[50] P. Cavaliere, M. Cabibbo, F. Panella, et al. "2198 Al–Li plates joined by friction stir welding: mechanical and microstructural behavior". In: *Materials & Design* 30.9 (2009), pp. 3622–3631 (cit. on p. 17).

[51] M. X. Milagre, N. V. Mogili, U. Donatus, et al. "On the microstructure characterization of the AA2098-T351 alloy welded by FSW". In: *Materials Characterization* 140 (2018), pp. 233–246 (cit. on p. 17).

[52] O. Lorrain, J. Serri, V. Favier, et al. "A contribution to a critical review of friction stir welding numerical simulation". In: *Journal of mechanics of materials and structures* 4.2 (2009), pp. 351–369 (cit. on p. 17).

[53] L. Fratini, G. Buffa, and R. Shivpuri. "Improving friction stir welding of blanks of different thicknesses". In: *Materials Science and Engineering: A* 459.1-2 (2007), pp. 209–215 (cit. on p. 17).

[54] M. Assidi, L. Fourment, S. Guerdoux, et al. "Friction model for friction stir welding process simulation: Calibrations from welding experiments". In: *International Journal of Machine Tools and Manufacture* 50.2 (2010), pp. 143–155 (cit. on pp. 17, 18).

[55] L. Zhu and C. S. Peskin. "Simulation of a flapping flexible filament in a flowing soap film by the immersed boundary method". In: *Journal of Computational Physics* 179.2 (2002), pp. 452–468 (cit. on p. 18).

[56] G. Chen, S. Zhang, Y. Zhu, et al. "Thermo-mechanical analysis of friction stir welding: A review on recent advances". In: *Acta Metallurgica Sinica (English Letters)* 33.1 (2020), pp. 3–12 (cit. on pp. 18, 19).

[57] A. Tongne, C. Desrayaud, M. Jahazi, et al. "On material flow in friction stir welded Al alloys". In: *Journal of Materials Processing Technology* 239 (2017), pp. 284–296 (cit. on p. 18).

[58] A. Tongne, H. Robe, C. Desrayaud, et al. "Two dimensional Coupled Eulerian Lagrangian (CEL) model for banded structure prediction in friction stir welding with trigonal tool". In: *AIP Conference Proceedings*. Vol. 1769. 1. AIP Publishing LLC. 2016, p. 100007 (cit. on p. 18).

[59] L. Fratini and G. Buffa. "CDRX modelling in friction stir welding of aluminium alloys". In: *International Journal of Machine Tools and Manufacture* 45.10 (2005), pp. 1188–1194 (cit. on p. 19).

[60] H. Liu, K. Ushioda, and H. Fujii. "Elucidation of interface joining mechanism during friction stir welding through Cu/Cu-10Zn interfacial observations". In: *Acta Materialia* 166 (2019), pp. 324–334 (cit. on p. 19).

[61] F. Talati and S. Jalalifar. "Analysis of heat conduction in a disk brake system". In: *Heat and mass transfer* 45.8 (2009), p. 1047 (cit. on p. 19).

[62] H. Kasem, J. Thevenet, X. Boidin, et al. "An emissivity-corrected method for the accurate radiometric measurement of transient surface temperatures during braking". In: *Tribology International* 43.10 (2010), pp. 1823–1830 (cit. on pp. 19, 35).

[63] M. Collignon, A.-L. Cristol, P. Dufrenoy, et al. "Failure of truck brake discs: A coupled numerical–experimental approach to identifying critical thermomechanical loadings". In: *Tribology International* 59 (2013), pp. 114–120 (cit. on p. 20).

[64] F. Bagnoli, F. Dolce, and M. Bernabei. "Thermal fatigue cracks of fire fighting vehicles gray iron brake discs". In: *Engineering Failure Analysis* 16.1 (2009), pp. 152–163 (cit. on p. 20).

[65] S. J. Kim, M. H. Cho, K. H. Cho, et al. "Complementary effects of solid lubricants in the automotive brake lining". In: *Tribology International* 40.1 (2007), pp. 15–20 (cit. on p. 20).

[66] M. Cho, S. Kim, R. Basch, et al. "Tribological study of gray cast iron with automotive brake linings: The effect of rotor microstructure". In: *Tribology International* 36.7 (2003), pp. 537–545 (cit. on p. 20).

[67] W. Grzesik and J. Rech. "Development of tribo-testers for predicting metal cutting friction". In: *Journal of Machine Engineering* 19 (2019) (cit. on p. 21).

[68] R. M'Saoubi and H. Chandrasekaran. "Innovative methods for the investigation of tool-chip adhesion and layer formation during machining". In: *CIRP annals* 54.1 (2005), pp. 59–62 (cit. on p. 21).

[69] D. S. Kilic and S. Raman. "Observations of the tool–chip boundary conditions in turning of aluminum alloys". In: *Wear* 262.7-8 (2007), pp. 889–904 (cit. on p. 21).

[70] P. Arrazola, D. Ugarte, and X. Dominguez. "A new approach for the friction identification during machining through the use of finite element modeling". In: *International Journal of Machine Tools and Manufacture* 48.2 (2008), pp. 173–183 (cit. on p. 21).

[71] P. J. Arrazola and T. Özel. "Investigations on the effects of friction modeling in finite element simulation of machining". In: *International Journal of Mechanical Sciences* 52.1 (2010), pp. 31–42 (cit. on pp. 21, 22).

[72] P. Albrecht. "New developments in the theory of the metal-cutting process: part I. The ploughing process in metal cutting". In: (1960) (cit. on p. 21).

[73] S. Kato, K. Yamaguchi, and M. Yamada. "Stress distribution at the interface between tool and chip in machining". In: (1972) (cit. on p. 22).

[74] K. Maekawa, T. Kitagawa, and T. Childs. "Friction characteristics at tool-chip interface in steel machining". In: *Tribology Series*. Vol. 32. Elsevier, 1997, pp. 559–567 (cit. on p. 22).

[75] T. Childs. "Friction modelling in metal cutting". In: *Wear* 260.3 (2006), pp. 310–318 (cit. on p. 22).

[76] G. Ortiz-de-Zarate, A. Madariaga, P. J. Arrazola, et al. "A novel methodology to characterize tool-chip contact in metal cutting using partially restricted contact length tools". In: *CIRP Annals* (2021) (cit. on pp. 22, 23).

[77] S. N. Melkote, W. Grzesik, J. Outeiro, et al. "Advances in material and friction data for modelling of metal machining". In: *CIRP Annals* 66.2 (2017), pp. 731–754 (cit. on pp. 23, 24).

[78] L. Sterle, F. Pušavec, and M. Kalin. "Determination of friction coefficient in cutting processes: comparison between open and closed tribometers". In: *Procedia CIRP* 82 (2019), pp. 101–106 (cit. on pp. 25, 29).

[79] T. Kagnaya, C. Boher, L. Lambert, et al. "Wear mechanisms of WC-Co cutting tools from high-speed tribological tests". In: *Wear* 267.5-8 (2009), pp. 890–897 (cit. on pp. 25, 29).

[80] P. Bollig, J. Michna, C. Faltin, et al. "Experimental and simulative modeling of drilling processes for the compensation of thermal effects". In: (2018), pp. 145–180 (cit. on pp. 25, 29).

[81] M. Olsson, S. Söderberg, S. Jacobson, et al. "Simulation of cutting tool wear by a modified pin-on-disc test". In: *International Journal of Machine Tools and Manufacture* 29.3 (1989), pp. 377–390 (cit. on pp. 26, 27, 29).

[82] F. Zemzemi, W. Bensalem, J. Rech, et al. "New tribometer designed for the characterisation of the friction properties at the tool/chip/workpiece interfaces in machining". In: *Tribotest* 14.1 (2008), pp. 11–25 (cit. on pp. 26, 27, 29).

[83] P. Hedenqvist and M. Olsson. "Sliding wear testing of coated cutting tool materials". In: *Tribology International* 24.3 (1991), pp. 143–150 (cit. on pp. 26, 27, 29).

[84] C. Claudin, A. Mondelin, J. Rech, et al. "Effects of a straight oil on friction at the toolworkmaterial interface in machining". In: *International Journal of Machine Tools and Manufacture* 50.8 (2010), pp. 681–688 (cit. on pp. 27–29, 45, 51, 52, 57, 92).

[85] H. Puls, F. Klocke, and D. Lung. "Experimental investigation on friction under metal cutting conditions". In: *Wear* 310.1-2 (2014), pp. 63–71 (cit. on pp. 28, 29).

[86] H. Puls, F. Klocke, and D. Lung. "A new experimental methodology to analyse the friction behaviour at the tool-chip interface in metal cutting". In: *Production Engineering* 6.4-5 (2012), pp. 349–354 (cit. on p. 28).

[87] M. Kunogi. "On plastic deformation of hollow cylinders under axial compressive loading". In: (1954) (cit. on p. 29).

[88] T. Schrader, M. Shirgaokar, and T. Altan. "A critical evaluation of the double cup extrusion test for selection of cold forging lubricants". In: *Journal of Materials Processing Technology* 189.1 (2007), pp. 36–44 (cit. on p. 29).

[89] G. Lahoti and T. Al tan. "Ring and spike test for evaluating lubricants". In: *Battelle topical report* 11 (1982) (cit. on p. 30).

[90] S. Isogawa, A. Kimura, and Y. Tozawa. "Proposal of an evaluating method on lubrication". In: *CIRP annals* 41.1 (1992), pp. 263–266 (cit. on p. 30).

[91] S. Sheljaskow. "Tool lubricating systems in warm forging". In: *Journal of Materials Processing Technology* 113.1-3 (2001), pp. 16–21 (cit. on p. 30).

[92] P. Marx. "Mechanische Beschichtung für die Kaltmassivumformung von Stahl". PhD thesis. Technische Universität, 2003 (cit. on p. 30).

[93] N. Bay, O. Wibom, and J. A. Nielsen. "A New Friction and Lubrication Test for Cold Forging". In: *CIRP Annals* 44.1 (1995), pp. 217–221 (cit. on p. 30).

[94] T. Wanheim. "Friction at high normal pressures". In: *Wear* 25.2 (1973), pp. 225–244 (cit. on p. 30).

[95] H. Sofuoglu and J. Rasty. "On the measurement of friction coefficient utilizing the ring compression test". In: *Tribology International* 32.6 (1999), pp. 327–335 (cit. on p. 30).

[96] T. Schrader, M. Shirgaokar, and T. Altan. "A critical evaluation of the double cup extrusion test for selection of cold forging lubricants". In: *Journal of materials processing technology* 189.1-3 (2007), pp. 36–44 (cit. on p. 30).

[97] J. Hardell, E. Kassfeldt, and B. Prakash. "Friction and wear behaviour of high strength boron steel at elevated temperatures of up to 800 °C". In: *Wear* 264.9-10 (2008), pp. 788–799 (cit. on pp. 31–33, 35).

[98] I. Velkavrh, M. Lüchinger, K. Kern, et al. "Using a standard pin-on-disc tribometer to analyse friction in a metal forming process". In: *Tribology International* 114 (2017), pp. 418–428 (cit. on p. 31).

[99] J. Hardell, S. Hernandez, S. Mozgovoy, et al. "Effect of oxide layers and near surface transformations on friction and wear during tool steel and boron steel interaction at high temperatures". In: *Wear* 330 (2015), pp. 223–229 (cit. on pp. 31, 32).

[100] J. Hardell, E. Kassfeldt, and B. Prakash. "Friction and wear behaviour of high strength boron steel at elevated temperatures of up to 800 C". In: *Wear* 264.9-10 (2008), pp. 788–799 (cit. on p. 32).

[101] A. Ghiotti, S. Bruschi, and F. Borsetto. "Tribological characteristics of high strength steel sheets under hot stamping conditions". In: *Journal of Materials Processing Technology* 211.11 (2011), pp. 1694–1700 (cit. on pp. 31, 32, 35).

[102] J. Brocail, M. Watremez, and L. Dubar. "Identification of a friction model for modelling of orthogonal cutting". In: *International Journal of Machine Tools and Manufacture* 50.9 (2010), pp. 807–814 (cit. on pp. 32, 33, 35, 46–48).

[103] J. Hardell and B. Prakash. "High-temperature friction and wear behaviour of different tool steels during sliding against Al–Si-coated high-strength steel". In: *Tribology International* 41.7 (2008), pp. 663–671 (cit. on p. 32).

[104] C. Courbon, M. Fallqvist, J. Hardell, et al. "Adhesion tendency of PVD TiAlN coatings at elevated temperatures during reciprocating sliding against carbon steel". In: *Wear* 330-331 (2015), pp. 209–222 (cit. on p. 32).

[105] Ö. N. Cora, K. Namiki, and M. Koç. "Wear performance assessment of alternative stamping die materials utilizing a novel test system". In: *Wear* 267.5-8 (2009), pp. 1123–1129 (cit. on pp. 33–35).

[106] C. Boher, S. Le Roux, L. Penazzi, et al. "Experimental investigation of the tribological behavior and wear mechanisms of tool steel grades in hot stamping of a high-strength boron steel". In: *Wear* 294-295 (2012), pp. 286–295 (cit. on pp. 33–35).

[107] L. Deng, L. Pelcastre, J. Hardell, et al. "Experimental Evaluation of Galling Under Press Hardening Conditions". In: *Tribology Letters* 66.3 (2018), pp. 1–11 (cit. on pp. 33–35).

[108] A. Gåård, P. Krakhmalev, and J. Bergström. "Influence of tool steel microstructure on origin of galling initiation and wear mechanisms under dry sliding against a carbon steel sheet". In: *Wear* 267.1-4 (2009), pp. 387–393 (cit. on pp. 34, 35).

[109] W. Österle, I. Dörfel, C. Prietzel, et al. "A comprehensive microscopic study of third body formation at the interface between a brake pad and brake disc during the final stage of a pin-on-disc test". In: *Wear* 267.5-8 (2009), pp. 781–788 (cit. on pp. 35, 36, 38).

[110] Y. Desplanques, O. Roussette, G. Degallaix, et al. "Analysis of tribological behaviour of pad–disc contact in railway braking: Part 1. Laboratory test development, compromises between actual and simulated tribological triplets". In: *Wear* 262.5-6 (2007), pp. 582–591 (cit. on pp. 35–38).

[111] A.-L. Cristol-Bulthé, Y. Desplanques, and G. Degallaix. "Coupling between friction physical mechanisms and transient thermal phenomena involved in pad–disc contact during railway braking". In: *Wear* 263.7-12 (2007), pp. 1230–1242 (cit. on p. 35).

[112] M. Kumar, X. Boidin, Y. Desplanques, et al. "Influence of various metallic fillers in friction materials on hot-spot appearance during stop braking". In: *Wear* 270.5-6 (2011), pp. 371–381 (cit. on p. 35).

[113] D. Meresse, S. Harmand, M. Siroux, et al. "Experimental disc heat flux identification on a reduced scale braking system using the inverse heat conduction method". In: *Applied Thermal Engineering* 48 (2012), pp. 202–210 (cit. on pp. 36–38).

[114] S. Kobayashi. "A review on the finite-element method and metal forming process modeling". In: *Journal of Applied Metalworking* 2.3 (1982), pp. 163–169 (cit. on p. 38).

[115] R. Hedayati and M. Sadighi. *Bird strike: an experimental, theoretical and numerical investigation*. Woodhead Publishing, 2015 (cit. on p. 39).

[116] A. Raczy, M. Elmadagli, W. Altenhof, et al. "An Eulerian finite-element model for determination of deformation state of a copper subjected to orthogonal cutting". In: *Metallurgical and materials transactions a* 35.8 (2004), pp. 2393–2400 (cit. on p. 39).

[117] P. M. Dixit and U. S. Dixit. *Modeling of metal forming and machining processes: by finite element and soft computing methods*. Springer Science & Business Media, 2008 (cit. on pp. 39, 40).

[118] J. Kronsteiner, D. Horwatitsch, and K. Zeman. "Comparison of updated Lagrangian FEM with arbitrary Lagrangian Eulerian method for 3D thermo-mechanical extrusion of a tube profile". In: 1896.1 (2017), p. 140006 (cit. on p. 39).

[119] J. P. Davim. *Computational Methods and Production Engineering: Research and Development*. Woodhead Publishing, 2017 (cit. on p. 39).

[120] J. Rodriguez, J. Carbonell, and P. Jonsen. "Numerical methods for the modelling of chip formation". In: *Archives of Computational Methods in Engineering* 27.2 (2020), pp. 387–412 (cit. on pp. 39, 40).

[121] L. Olovsson, L. Nilsson, and K. Simonsson. "An ALE formulation for the solution of two-dimensional metal cutting problems". In: *Computers & structures* 72.4-5 (1999), pp. 497–507 (cit. on p. 39).

[122] U. S. Dixit. "Modeling of metal forming: a review". In: *Mechanics of Materials in Modern Manufacturing Methods and Processing Techniques*. Elsevier, 2020, pp. 1–30 (cit. on p. 40).

[123] M. Smith. *ABAQUS/Standard User's Manual, Version 6.13*. English. United States: Dassault Systemes Simulia Corp, 2013 (cit. on p. 40).

[124] J. Rech. "A multiview approach to the tribological characterisation of cutting tool coatings for steels in high-speed dry turning". In: *International journal of Machining and Machinability of Materials* 1.1 (2006), pp. 27–44 (cit. on p. 40).

[125] S. Hashmi. *Comprehensive materials processing*. Newnes, 2014 (cit. on p. 40).

[126] J. Hallquist, G. Goudreau, and D. Benson. "Sliding interfaces with contact-impact in large-scale Lagrangian computations". In: *Computer methods in applied mechanics and engineering* 51.1-3 (1985), pp. 107–137 (cit. on p. 40).

[127] D. Perić and D. Owen. "Computational model for 3-D contact problems with friction based on the penalty method". In: *International journal for numerical methods in engineering* 35.6 (1992), pp. 1289–1309 (cit. on p. 40).

[128] J. C. Simo and T. Laursen. "An augmented Lagrangian treatment of contact problems involving friction". In: *Computers & Structures* 42.1 (1992), pp. 97–116 (cit. on p. 40).

[129] C. El Boustani, J. Bleyer, M. Arquier, et al. "Dual finite-element analysis using second-order cone programming for structures including contact". In: *Engineering Structures* 208 (2020), p. 109892 (cit. on p. 40).

[130] H. Blok. "Theoretical study of temperature rise at surfaces of actual contact under oiliness lubricating conditions". In: *Proc. Instn. Mech. Engrs.(General discussion on lubrication and lubricants)* 2 (1937), p. 222 (cit. on p. 41).

[131] J. C. Jaeger. "Moving sources of heat and the temperature of sliding contacts". In: *Proceedings of the royal society of New South Wales*. Vol. 76. 1942, pp. 203–224 (cit. on p. 41).

[132] J. Bardon. "Sliding contact: a theoretical approach of imperfect contact condition". In: *Proceedings of the Pre-International Heat Transfer Conference Seminar, Michigan State University*. 1986 (cit. on p. 42).

[133] N. Laraqi. "Phénomène de constriction thermique dans les contacts glissants". In: *International journal of heat and mass transfer* 39.17 (1996), pp. 3717–3724 (cit. on p. 42).

[134] P. Chantrenne and M. Raynaud. "A microscopic thermal model for dry sliding contact". In: *International journal of heat and mass transfer* 40.5 (1997), pp. 1083–1094 (cit. on p. 42).

[135] W. Grzesik and C. Van Luttervelt. "An investigation of the thermal effects in orthogonal cutting associated with multilayer coatings". In: *CIRP Annals* 50.1 (2001), pp. 53–56 (cit. on p. 42).

[136] F. P. Bowden, F. P. Bowden, and D. Tabor. *The friction and lubrication of solids*. Vol. 1. Oxford university press, 2001 (cit. on p. 42).

[137] F. Zemzemi, J. Rech, W. Ben Salem, et al. "Development of a friction model for the tool-chip-workpiece interfaces during dry machining of AISI4142 steel with TiN coated carbide cutting tools". In: *International Journal of Machining and Machinability of Materials* 2.3-4 (2007), pp. 361–377 (cit. on pp. 43, 44).

[138] J. Rech, C. Claudin, and E. D'eramo. "Identification of a friction model—application to the context of dry cutting of an AISI 1045 annealed steel with a TiN-coated carbide tool". In: *Tribology International* 42.5 (2009), pp. 738–744 (cit. on pp. 43, 44, 92, 94).

[139] C. Courbon. "Vers une modélisation physique de la coupe des aciers spéciaux: intégration du comportement métallurgique et des phénomènes tribologiques et thermiques aux interfaces". PhD thesis. Ecully, Ecole centrale de Lyon, 2011 (cit. on pp. 43, 44, 91, 94).

[140] J. Rech, P. J. Arrazola, C. Claudin, et al. "Characterisation of friction and heat partition coefficients at the tool-work material interface in cutting". In: *CIRP Annals - Manufacturing Technology* 62.1 (2013), pp. 79–82 (cit. on pp. 44, 51, 56–58, 92).

[141] M. Akbari, S. Buhl, C. Leinenbach, et al. "A new value for Johnson Cook damage limit criterion in machining with large negative rake angle as basis for understanding of grinding". In: *Journal of Materials Processing Technology* 234 (2016), pp. 58–71 (cit. on pp. 47, 48).

[142] N. Ruttimann, M. Roethlin, S. Buhl, et al. "Simulation of hexa-octahedral diamond grain cutting tests using the SPH method". In: *Procedia CIRP* 8 (2013), pp. 322–327 (cit. on pp. 47, 48).

[143] M. Afrasiabi, L. Meier, M. Röthlin, et al. "GPU-accelerated meshfree simulations for parameter identification of a friction model in metal machining". In: *International Journal of Mechanical Sciences* 176 (2020), p. 105571 (cit. on pp. 47, 48).

[144] H. B. Abdelali, W. B. Salem, J. Rech, et al. "Numerical characterisation of the friction coefficient at the tool–chip–workpiece interface during friction tests of AISI 1045". In: *International Journal of Microstructure and Materials Properties* 9.2 (2014), pp. 147–159 (cit. on pp. 47, 48, 51).

[145] O. I. Abdullah and J. Schlattmann. "Temperature analysis of a pin-on-disc tribology test using experimental and numerical approaches". In: *Friction* 4.2 (2016), pp. 135–143 (cit. on p. 51).

[146] T. Bui. "Explicit and implicit methods in solving differential equations". PhD thesis. 2010 (cit. on p. 53).

[147] M. Nazem, J. P. Carter, and D. W. Airey. "Arbitrary Lagrangian-Eulerian method for dynamic analysis of geotechnical problems". In: *Computers and Geotechnics* 36.4 (May 2009), pp. 549–557 (cit. on p. 53).

[148] M. Jawaid and M. Thariq. *Sustainable Composites for Aerospace Applications*. Woodhead publishing, 2018 (cit. on p. 53).

[149] I. M. Arrieta. "Study of microstructural aspects when broaching ferritic-pearlitic steels: influence on cutting mechanisms, tribological and material properties". PhD thesis. 2018 (cit. on pp. 54–56).

[150] J. Rech, P. Arrazola, C. Claudin, et al. "Characterisation of friction and heat partition coefficients at the tool-work material interface in cutting". In: *CIRP Annals* 62.1 (2013), pp. 79–82 (cit. on p. 55).

[151] S. P. Jaspers and J. H. Dautzenberg. "Material behaviour in conditions similar to metal cutting: Flow stress in the primary shear zone". In: *Journal of Materials Processing Technology* 122.2-3 (Mar. 2002), pp. 322–330 (cit. on p. 55).

[152] M. Putz, G. Schmidt, U. Semmler, et al. "Heat Flux in Cutting: Importance, Simulation and Validation". In: *Procedia CIRP* 31 (2015). 15th CIRP Conference on Modelling of Machining Operations (15th CMMO), pp. 334–339 (cit. on p. 57).

[153] P. Kieruj, D. Przestacki, and T. Chwalczuk. "Determination of emissivity coefficient of heat-resistant super alloys and cemented carbide". In: *Archives of Mechanical Technology and Materials* 36.1 (June 2016), pp. 30–34 (cit. on pp. 62, 68, 79, 83, 84).

[154] M. Schneider, L. Berthe, R. Fabbro, et al. "Measurement of laser absorptivity for operating parameters characteristic of laser drilling regime". In: *Journal of Physics D: Applied Physics* 41.15 (2008), p. 155502 (cit. on p. 76).

[155] N. M. Low. "The Thermal Insulating Properties of Vermiculite". In: *Journal of Thermal Envelope and Building Science* 8.2 (Oct. 1984), pp. 107–115 (cit. on p. 78).

[156] J. S. Arora. *Introduction to optimum design*. Elsevier, 2004 (cit. on p. 98).

École Nationale d'Ingénieurs de Saint-Etienne de Saint-Étienne

Ecole Centrale de Lyon

N° d'ordre : ……2021LYSEE005……

Jian CAO

Towards a new methodology to identify friction models under severe contact conditions

Speciality : Mechanical & Engineering

Keywords : finite element method, severe contact, contact temperature, thermal contact resistance, friction coefficient.

Abstract :

This PhD work deals with the understanding and the modelling of severe tribological contact. Severe tribological contact is observable in many applications such as manufacturing processes, such as cutting and forming processes. They are also present in braking applications for cars and aircraft, etc. In severe tribological conditions, contact pressures and temperatures are so high that, at least, one of the two solids in contact is plastified to a certain extent, and rapid and significant wear is observable within some minutes or even seconds. In this context, the standard friction model considering two elastic solids in contact and the standard tribometers, such as pin-on-disc, are no more applicable. The scientific investigation of such conditions requires to develop specific experimental set-up and corresponding numerical simulations so as to analyse complex local tribological phenomena at the interface such as local contact pressure, local temperature, local sliding velocity, etc.

This thesis aims at generally improving the numerical simulation of a sliding contact under extreme contact conditions and proposing an innovative methodology to better identify friction models. The driving idea is that a robust simulation of the local contact conditions is definitely needed to reach a better understanding of the complex phenomena occurring under

such specific conditions and to identify a friction model depending on local tribological parameters.

École Nationale d’Ingénieurs de Saint-Etienne de Saint-Étienne

Ecole Centrale de Lyon

N° d’ordre : ……2021LYSEE005……

Jian CAO

Une nouvelle méthodologie pour identifier des modèles de frottement dans des conditions de contact sévères.

Spécialité: Mécanique et Ingénierie

Mots clefs : méthode des éléments finis, contact sévère, température de contact, résistance thermique de contact, coefficient de frottement.

Résumé :

Ce travail de thèse porte sur la compréhension et la modélisation des contacts tribologiques sévères. Les contacts tribologiques sévères sont observables dans des nombreuses applications telles que les procédés de fabrication, tels que les procédés de usinage et de formage. Ils également présentent dans les applications de freinage pour les voitures et les avions, etc. Conditions tribologiques sévères, les pressions et températures de contact sont si élevées qu'au moins l'un des deux solides en contact est plastifié dans une certaine mesure, et une usure rapide et importante est observable en quelques minutes voire quelques secondes. Le modèle de friction considérant deux solides élastiques en contact et les tribomètres standard, tels que le pin-on-disc, ne sont plus applicables. L'étude scientifique de telles conditions nécessite de développer un montage expérimental spécifique et des simulations numériques correspondantes afin d'analyser des locaux complexes phénomènes tribologiques à l'interface tels que pression de contact locale, température locale, vitesse de glissement locale, etc.

Cette thèse vise à améliorer de manière générale la simulation numérique d'un contact glissant dans des conditions de contact extrêmes et à proposer une méthodologie innovante pour mieux identifier les modèles de frottement. L'idée maîtresse est qu'une simulation robuste des conditions de contact locales est absolument nécessaire pour parvenir à une meilleure compréhension des phénomènes complexes se produisant dans de telles conditions

spécifiques et pour identifier un modèle de frottement en fonction des paramètres tribologiques locaux.